PHYSIK-DEPARTMENT

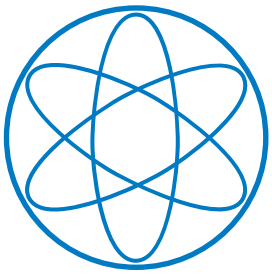

Simulation of Cosmic-Ray Antimatter Fluxes

Master Thesis
by
Laura Šerkšnytė

Dense and Strange Hadronic Matter
Prof. Dr. Laura Fabbietti
01.10.2019

TECHNISCHE UNIVERSITÄT MÜNCHEN

Abstract

Multiple astrophysical observations, such as the galactic rotation curves, the gravitational lensing or the microwave background radiation, can be explained only by introducing a new form of matter - the dark matter. No dark matter particle has ever been detected but there are many experiments trying to find it. The indirect dark matter search is based on detecting the ordinary matter cosmic ray particles produced in the dark matter annihilations and decays in the universe. The dark matter signal would be seen as a discrepancy between the cosmic ray measurements and the expected background cosmic ray flux. To have as small background as possible, antiparticles are the best hadronic observable in the indirect dark matter searches. To see discrepancies between the measured flux and the expected flux, precise models are required for cosmic ray background simulations.
The antiproton cosmic ray flux is the subject of this thesis. In this work we created a framework using already existing individual models to propagate cosmic ray particles from their creation point trough the galaxy, the heliosphere and the earth's environment. We constrained our propagation chain using available proton and helium cosmic ray measurements. We investigated several parametrizations of the antiproton production in $p+p$ collisions and the antiproton production in several event generators: GiBUU, EPOS and PYTHIA. We implemented a general solution in GALPROP which uses the event generator output for the antiproton creation as well as one of the available antiproton parametrizations. Finally we studied the antiproton cosmic rays, produced using the studied antiproton production parametrizations and the GiBUU generator results and propagated using our propagation chain.

Contents

Chapter 1

Introduction

Dark matter was first mentioned by Fritz Zwicky in 1933 [1]. He used Doppler shift measurements to determine the velocities of galaxies in Coma cluster and applied the virial theorem to extract the mass required to maintain such velocity profile. The required mass was 400 times higher than the expected mass of visible matter, predicted by measuring the luminosity of the cluster. The missing mass was assigned to non-visible matter and named dark matter. Another way to account for the missing mass is modified gravity. However, the newest observational evidence, including the Bullet Cluster, strongly prefers the theory of dark matter [2]. The Bullet cluster resulted from a collision of two galaxy clusters. The analysis of this cluster uses gravitational lensing data thus the gravitation force law is not included in the calculations. A spacial offset of 8σ significance was measured between the centrer of total mass and the center of the baryonic mass peaks. This could not be explained by the modified theory of general relativity.
Even though the number of observational evidence for dark matter is increasing, no dark matter particle was ever detected. Multiple dark matter theories suggest candidates and gives predictions for properties such as mass or spin. Any measurement of these properties would put constrains on the dark matter models. The existing techniques to detect dark matter can be divided into direct and indirect dark matter searches as well as collider experiments. In the first two cases the huge background is the main drawback. One of the direct search techniques measures recoil energy of nuclei scattered off the dark matter particles. The background for such measurement consist of neutrino-, neutron- and electron-induced recoil [3]. The indirect search is, for example, looking for charged antinuclei produced in the annihilation or decay of dark matter. On earth we would see these antinuclei as cosmic rays. In this case, the background consists of the same charged antinuclei produced in ordinary matter interactions [4]. The collider experiments are searching for dark matter particles produced in the particle collisions. Dark matter particle would escape the detectors unnoticed. Thus the collider experiments are looking for the missing energy in the collisions [5].
Cosmic rays were discovered by Victor Franz Hess in 1912 who later was awarded a Nobel prize for it. Before Hess experiment, it was thought that all radiation measured on earth is produced by radioactive decays in the earth crust. Under this assumption it was expected that measuring the radiation further away from earth's surface would result in smaller fluxes. Hess conducted 7 balloon flights during 1912 using Wulf electrometers, measuring the ionized particle flux at different altitudes. The result was opposite than expected - the flux increased going to higher altitudes. This could only be explained by postulating that the radiation enters

our atmosphere from above [6]. The Sun was rejected as a possible source of this radiation because the conclusion of the experiment didn't change even when the measurement was conducted during near-total eclipse. The concept of galactic cosmic rays was introduced. The antimatter discovery in cosmic rays followed in 1932 by Carl David Anderson who shared Nobel prize with Victor Hess. While investigating cosmic rays using cloud chamber photographs, he found particle tracks which could be explained only by the existence of positively charged electrons [7].

The origin of cosmic rays for a long time was a mystery even though it was widely agreed that they should stem from supernovae. This was finally confirmed by the NASA's Fermi Gamma-ray Space Telescope observations. The signature of proton acceleration is neutral pions produced in collisions with interstellar material. Neutral pions decay into gamma rays. Such spectral feature was detected in two supernova remnants (SNRs) indicating them as acceleration sites [8]. Particles accelerated by SNRs are called primary. This mechanism cannot explain the antiparticles seen in cosmic rays. Antiparticles are either created as secondary particles in cosmic ray interactions with interstellar medium or originate from exotic sources such as evaporating primordial black holes, annihilating or decaying dark matter. To gain any information from the measured flux one needs theoretical or numerical models to interpret it. The different antimatter production sources are governed by different physical processes thus producing antiparticles with different momentum spectra. If the exotic signal to secondary background ratio is high enough, the signature of exotic sources can be extracted from the measured spectra.

The simulations of cosmic rays consist of two main components: the production of antimatter and its propagation towards the earth including interactions with the interstellar medium. The production of antiparticles and interactions in the interstellar medium are the subject of particle physics and collider experiments. The propagation part is purely astrophysical and can be constrained from primary to secondary particle ratio measurements.

The launch of the Alpha Magnetic Spectrometer (AMS-02) in 2011 started a new precision era in cosmic ray measurements. The uncertainties of the measured particle and antiparticle fluxes are smaller than the current uncertainties for cosmic ray simulations. The only confirmed antimatter particles detected are antiprotons and their flux agrees in uncertainty limits with the theoretical predictions. This means that the exotic antiproton component is either of the same magnitude as background or even lower. One way to reduce background in such experiment is to measure heavier antinuclei. The number of antinuclei produced depends on the probability of the required energy collision to happen and the probability of produced antinucleons to coalesce. Heavier antinuclei production requires higher energy collision which reduces the first probability. The second probability is reduced by the fact that more baryons must be produced in one collision and all antinucleons must be close in phasespace. Thus the secondary flux for antinuclei is smaller with increasing mass number.

Antideuteron flux prediction requires perfect understanding of the already measured antiproton flux and hadronic interactions. Antimatter can be produced within the interstellar medium mainly via p+p collisions (60%) but a fraction of it originates from p+A and A+A collisions (40%). Accelerator-based experiments allow to study such production cross sections. The data for antiproton production in collisions as well as measurements of momentum spectra of antiprotons produced in p+p collisions are really scarce. This limits the understanding of antiproton flux immensely.

In this work we investigated the cosmic ray propagation and production. First, we study the

propagation of cosmic rays in galaxy, heliosphere and earth's environment using different Monte Carlo (MC) simulations. We constrain the propagation parameters using measured proton and helium fluxes as well boron to carbon ratio data. Secondly, we study the antiproton production using different existing cross section parametrizations and MC generators and compare them to existing accelerator data. Lastly we use the analyzed antiproton production cross sections for antiproton production in the galaxy and propagate them to earth and compare the resulting flux to existing balloon and satellite measurements.

Chapter 2

Dark Matter

2.1 Observational Evidence of Dark matter

The idea of dark matter comes from observational evidence in the universe. The velocities of galaxies in galaxy clusters and the galactic rotation curves were the first two measurements concluding the requirement of dark matter [1][9]. Later on the cluster collisions and the effect of gravitational lensing were observed. The cosmic microwave background measurements improved our understanding of cosmological structure formation and demands the existence of dark matter as well. The galaxy cluster measurement by Zwicky is already explained in the introduction. The rest will be presented in the following chapter.

2.1.1 Galactic rotation curves

The orbital speed of visible stars or gas dependence on radial distance from the center of the galaxy is called the galactic rotation curve. The rotation of matter in the galaxy was expected to follow the Keplerian motion and its' velocity profile to decrease radially:

$$\frac{dv}{dr} = \frac{d\sqrt{\frac{GM}{r}}}{dr} = -\frac{1}{2}\sqrt{\frac{GM}{R^3}} = -\frac{v}{2r} \tag{2.1}$$

The first analysis of galactic rotation curves by Horace W. Babcock in 1939 [10] and Jan Oort in 1940 [11] showed that the velocity profile is rather flat. The optical rotation curves were later on investigated by Vera Rubin and her colleagues. In Figure 2.1, their results on the observed 21 Sc galaxies published in 1980 are shown. The authors concluded that the rotational curves exhibit a behaviour different from expected Keplerian radial decrease which can be explained by non-luminous matter [9]. The analysis of radio telescope maps of 21 cm line of atomic hydrogen delivered similar results [12].

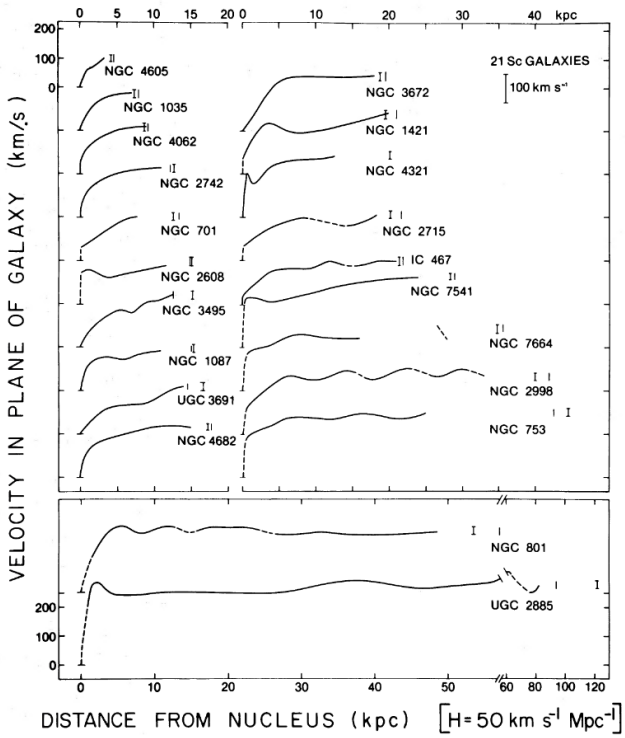

Figure 2.1 Mean velocities in the plane of the galaxy, as a function of linear distance from the nucleus of the galaxy. Curve drawn is rotation curve formed from the mean velocities on both sides on the major axis. From [9].

2.1.2 Gravitational lensing

Gravity in general relativity is understood as an interaction between matter and space-time. Matter and energy curves the space-time thus changing its geodesics. Matter and radiation travels along these geodesics as they are the shortest path between two points. As dark matter interacts gravitationally, it changes the curvature of space-time thus bending light passing by and causing gravitational lensing. Depending on the line of sight in the universe, strong or weak gravitational lensing might occur. In case of strong gravitational lensing, multiple images, arcs or Einstein rings can be produced. In case of weak gravitational lensing, the background objects can be distorted and this effect can be interpreted as coordinate transformation. In both cases, the mass of the lensing galaxy can be extracted from the geometrical distortion measurements.
The weak-lensing observations of a 1E 0657-558 cluster, also known as Bullet cluster, merger gave an opportunity to analyse the gravitational potential without any assumptions about gravitational force law [2]. The gravitational potential of such merger traces the distribution of matter. In case of no dark matter component, it should agree with the visible matter component seen in X-Ray measurements. But in the presence of dark matter, the gravitational potential should be "spatially coincident with the collisionless galaxies" [2]. Clowe et al. derived the map of gravitational potential using images from several datasets. As mentioned in the introduction, a spatial offset of 8σ significance between the visible mass distribution and the one derived from gravitational potential measurements was present.

2.1.3 Cosmic microwave background

At the early stage, the universe was filled with glowing plasma. As the universe expanded, the plasma and the radiation cooled down causing the protons and electrons to create a bound state of neutral hydrogen atom. The photons in plasma were constantly scattered by Thomson radiation but after the recombination the universe became transparent. This period is called photon decoupling. The cosmic microwave background (CMB) radiation are the relic radiation of the photons that existed at the epoch of photon decoupling.
Before the neutral hydrogen formed, the distribution of matter was almost uniform. The small density variations were caused by quantum mechanical fluctuations. These fluctuations caused gravity to pull both the normal and the dark matter to the higher density centers. The normal matter would fall in these centers until the pressure of photons would overcome the gravitational pull causing the matter to move outwards. At the point, when gravity would overcome the photon pressure, the normal matter would start fall in again. Dark matter interacts only gravitationally, thus there was no force to stop it from falling in the higher density centers. The size of the fluctuation depends on the size of these centers. The falling matter was hotter while the outwards moving matter was cooled down. The temperature differences in CMB measurements shows the distribution of dark matter before the recombination epoch. The Planck Collaboration analyses its data by fitting it to the ΛCDM model which assumes that the universe consists of dark energy, cold dark matter and ordinary matter. The last results published in 2018 gives dark matter density $\Omega_c h^2 = 0.120 \pm 0.001$ and baryon density $\Omega_b h^2 = 0.0224 \pm 0.0001$ which means 5.35 times more dark matter than ordinary matter [13].

2.2 Dark Matter Particles

Multiple particles were suggested as dark matter candidates. They must satisfy following conditions: be stable (on the order of Hubble time), have the right relic density and interact very weakly with the electromagnetic radiation [14]. Part of dark matter particle zoo is shown in Figure 2.2. The plot shows predicted masses and interaction cross sections for different candidates.
Standart Model neutrinos were considered as a possible dark matter candidate but the experimental results on relic abundance ruled out this possibility. Neutrinos are not abundant enough to account for dark matter component [15]. One of the Standard Model (SM) problems are the neutrino masses. The masses of fermions in SM comes from left- and right-handed field coupling. As in SM there are only left-handed neutrino fields, neutrinos should be massless. This could be resolved by introducing the right-handed neutrinos. Besides having opposite chirality, these neutrinos are not charged weakly. They have no SM gauge interactions and thus are called sterile neutrinos. A sterile neutrino can decay radiatively and produce monoenergetic X-ray flux. This can be used at indirect search of sterile neutrinos [16][17].
Other popular dark matter candidates are axions. They were introduced to solve the problem of CP violation. Following the experimental constrains, the axions should be extremely light and weakly interacting. The relic density of axions depend on the assumed production mechanism. Multiple direct detection experiments based on different physical processes are looking for axion [18][19][20]. The most widely studied dark matter candidates are WIMPs. They are predicted by three theories: supersymmetry (SUSY), universal extra dimensions (UED) and little Higgs. The most accepted candidates are suggested by SUSY and UED. If WIMPS exist,

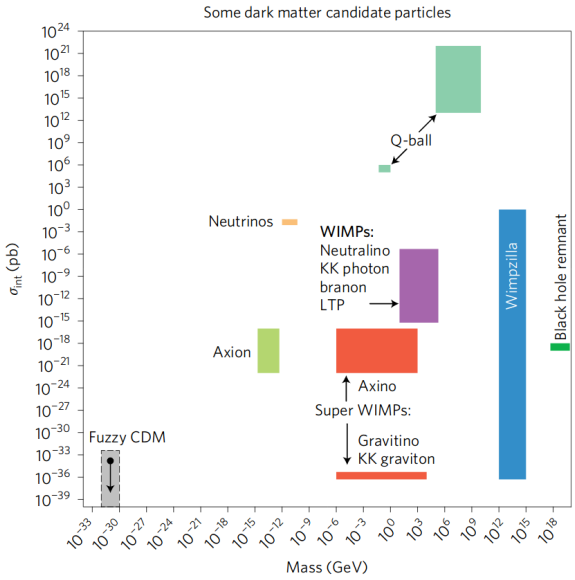

Figure 2.2 Dark matter candidates cross section dependence on particle mass. From [21].

they would be naturally produced with the right relic density and this possibly coincidence is referred to as the WIMP miracle [22]. There are numerous experimental ways to detect WIMPS [23]. In the scope of this thesis, the indirect detection is discussed.

2.2.1 WIMPs

The dark matter search consists of indirect and direct detection as well as collider production experiments.

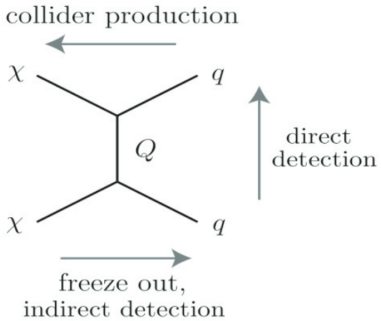

Figure 2.3 Example process for charged SM particle production in the annihilation of WIMPs. From [24].

In case of WIMPs, the direct search analyses dark matter particle scattering with nuclei by looking at nuclear recoil. The indirect search is looking for WIMP annihilation or decay products in our and other galaxies. The collider experiments are trying to produce dark matter particles in collisions and detect missing energy in transverse plane. These processes can be seen in toy Feynman diagram in Figure 2.3.
As mentioned before, WIMPs can be generated by three different physics theories, but the most analyzed WIMP candidates are neutralinos predicted by SUSY. Neutralinos can annihilate into

all SM particles producing two main signatures: high energy neutrino flux and anomalies in cosmic ray fluxes. Main annihilation channels can be split in several sections: weak gauge-boson final states, final states containing Higgs bosons, fermion final states and in some cases even final gluon and final photon states. The branching rations depend on the neutralino model. For example, if the neutralino mass is not high enough to produce the weak gauge-bosons, this channel is closed. In Figure 2.4 the Feynman diagrams contributing to neutralino annihilation into fermions are showed. All mentioned annihilation channels can be found in the theoretical work of Jungman et. al. [22]

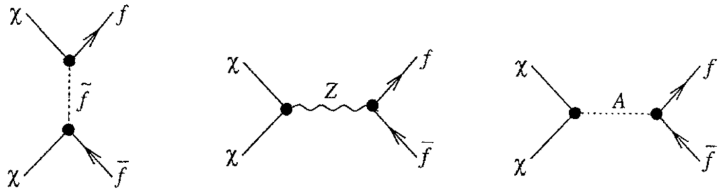

Figure 2.4 Diagrams contributing to neutralino annihilation into fermions. From [22].

The produced particles might emit other particles if they have sufficient energy. One of such possible processes is shown in Figure 2.5. In this work we are only interested in the charged antibaryon channel. If all contributing annihilation channels are considered it is possible to predict the spectra of produced baryons. Neutralinos annihilate in the halo of the galaxy and the produced particles propagate through the interstellar medium to all directions. On earth they can be measured as cosmic rays in satellite or balloon experiments.

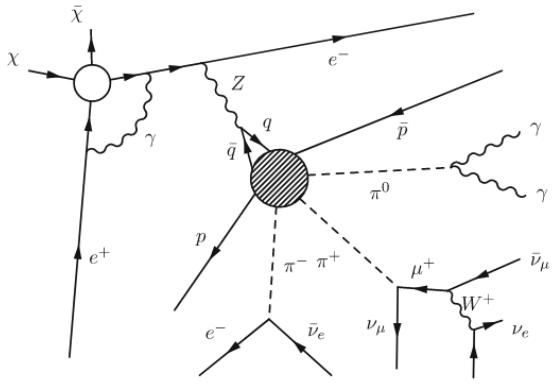

Figure 2.5 Example process for charged SM particle production in the annihilation of WIMPs. From [23].

2.2.2 Indirect dark matter detection: Charged cosmic rays

Neutralino is not the only WIMP particle decaying or annihilating into SM particles. It was given as an example for the sake of clarity. The baryonic matter can be produced by other dark matter candidates besides WIMPs as well. In case of the indirect dark matter search the most important part is to know the energy range of produced baryonic particles as this is necessary in the planning of the experiments. Besides the so called exotic antibaryon production, which

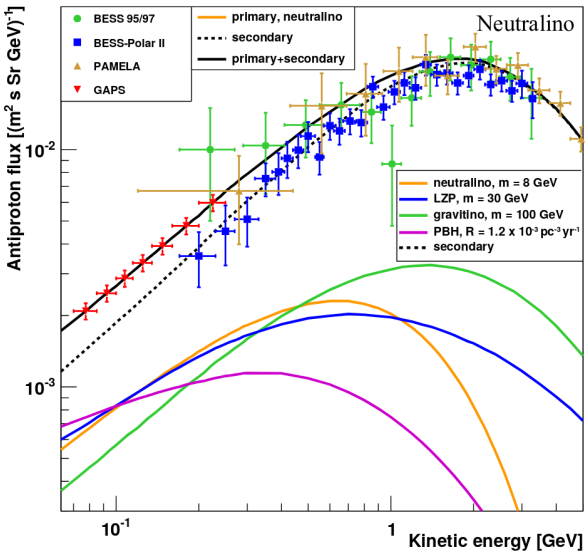

Figure 2.6 Experimental antiproton flux data and dark matter model predictions. From [25].

in this case is dark matter annihilation and decay, antibaryons are produced in the collisions of primary cosmic rays and the interstellar medium (ISM) particles.
The idea behind the indirect dark matter search is to measure the cosmic ray flux, compare it to existing models for the background flux - the secondary antiprotons from collisions in ISM - and search for deviations from the expected flux. Possible deviation can be interpreted as exotic component. Even if no deviations from theoretical expectations are seen, the upper limits on dark matter particle mass and annihilation cross sections can be computed. The most suited antiparticles for such experiments are antiproton, antideuteron and antihelium. In all cases, the antinuclei produced in dark matter interactions have kinetic energies lower than 10 GeV.
Currently only the antiproton cosmic ray flux is measured. Many research groups published experimental data for different antiproton energy ranges. In Figure 2.6 one can see the predicted antiproton flux for several different dark matter candidates together with background predictions and some of the existent experimental data. As the background prediction agrees with the data rather well, the exotic dark matter component must be the same or lower order of magnitude. As the antiproton background flux is large in comparison to dark matter component, it gives limited information about the dark matter properties. Heavier antinuclei have smaller background flux as their production requires coalescence. Predictions for antideuteron background flux and the dark matter component can be seen in Figure 2.7. At very low energies, the background should be by several orders of magnitude lower than the antiproton flux created in dark matter annihilations and decays. As mentioned before, the concept of indirect search is to measure cosmic ray flux and compare it to theoretical background predictions. The experimental data shown in the Figure 2.6 is rather old. The Alpha Magnetic Spectrometer (AMS-02) experiment started a new precision era. The data became so precise, that existent model uncertainties are higher that the measurement errors. This is clearly visible in Figure 2.8, where the main sources of uncertainties are shown. The goal of this work is to investigate the propagation and production of background antiprotons to understand the measured antiproton flux better.

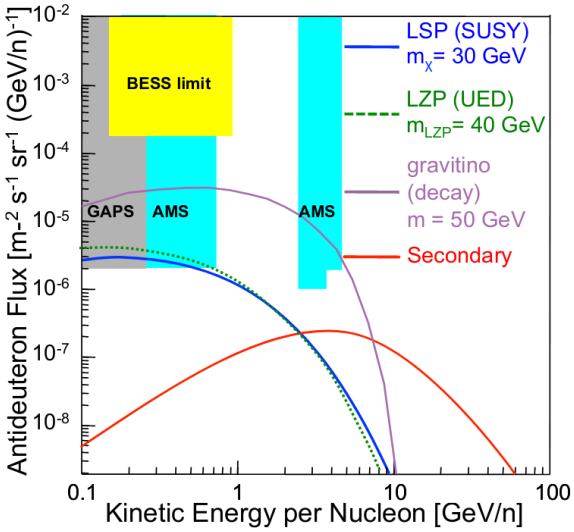

Figure 2.7 Predicted antideuteron background and dark matter flux components. The shaded regions show the existent experimental sensitivities. From [26].

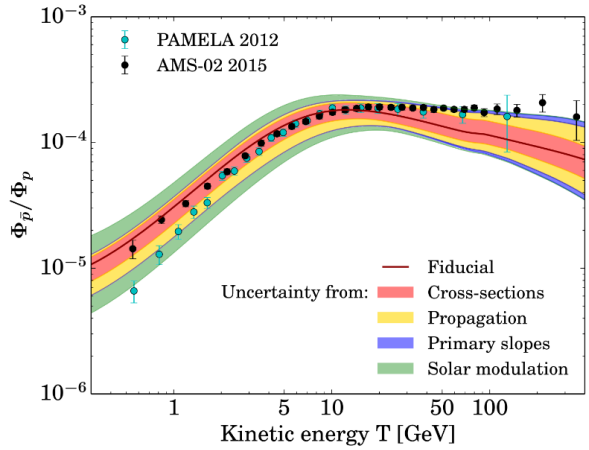

Figure 2.8 Antiproton flux measurements and model uncertainties. From [27].

Chapter 3

Cosmic Ray Propagation

3.1 Main Cosmic Ray Acceleration Mechanisms

The discovery of cosmic rays experimentally is already described in the Introduction. After it was known that some particles are coming from outside of the atmosphere, a theory was needed to explain, how and where these particles can be produced. In 1949 Enrico Fermi suggested a theory for the origin of the cosmic rays [28]. Accordingly to it, particles in interstellar medium can be accelerated by gaining energy from collisions against moving magnetic clouds. This theory is now called 2nd order Fermi acceleration. It had several drawbacks such as too long acceleration times, an unclear particle injection mechanism as it requires the injected particles to already have few 100 MeV energy and the power-law was not universal (it is dependent on the magnetic cloud velocity). After Fermi's suggestion, several scientists came up with the different idea of acceleration by shock waves [29]. Finally, in 1978 Anthony Raymon Bell published his theory of diffusive shock acceleration [30]. Now it is also known as 1st order Fermi acceleration.

3.1.1 2nd order Fermi acceleration

The principle of the 2nd order Fermi acceleration is based on several assumptions:

1. Magnetized plasma clouds are randomly moving in ISM.
2. Charged particles undergo "**collisionless** scattering" in the inhomogeneous magnetic field inside the cloud.
3. Particles do not lose energy inside the cloud
4. After the interaction with the cloud, the particles in general gain (head-on collisions) or lose (tail-on collisions) energy.

Let's assume that we have a head-on collision as shown in Figure 3.1. The further derivation is based on [31]. For simplicity, let's assume that the particle is already moving in relativistic speed $E \approx pc$. It enters the magnetic cloud with the total energy E_1. In the rest-frame of the cloud, the particle has the energy:

$$E_1^{'} = \gamma E_1 (1 - \beta cos\theta_1) \tag{3.1}$$

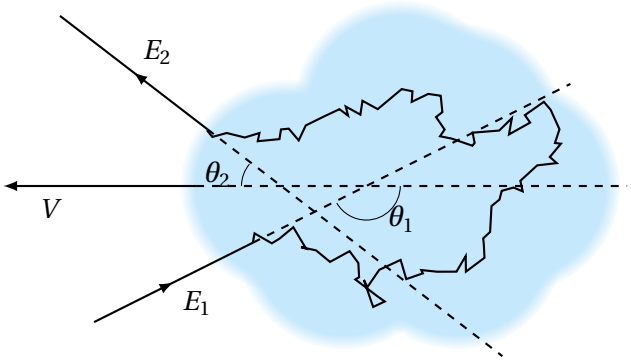

Figure 3.1 Particle interaction with magnetized cloud in interstellar medium.

Where $\beta = V/c$ is the speed of the cloud and $\gamma = 1/\sqrt{1-\beta^2}$ is the Lorentz factor. As mentioned before, the particle doesn't lose energy inside the cloud, only the direction of the particle changes. Thus $E_2^{'} = E_1^{'}$. When particles escape the cloud, their energy in lab frame will be:

$$E_2 = \gamma E_2^{'}(1 + \beta\, c\, o\, s\, \theta_2^{'}) \tag{3.2}$$

If we combine equations 3.1 and 3.2 we obtain:

$$\frac{E_2 - E_1}{E_1} = \frac{1 + \beta\cos\theta_2^{'} - \beta\cos\theta_1 - \beta^2\cos\theta_2^{'}\cos\theta_1}{1-\beta^2} - 1 \tag{3.3}$$

One particle collides with multiple magnetic clouds moving towards randomly distributed directions.
In the cloud frame, the escape angle is supposed to be isotropic so that $\langle\cos\theta_2^{'}\rangle = 0$. The collision probability depends on the relative velocity $c - V\cos\theta_1$ (if the cloud is faster than the particle, the collision would never happen). Thus the average of the incident angle:

$$\langle\cos\theta_1\rangle = \frac{\int_{-1}^{1}\cos\theta_1(c - V\cos\theta_1)d\cos\theta_1}{\int_{-1}^{1}(c - V\cos\theta_1)d\cos\theta_1} = -\frac{V}{3c} = -\frac{\beta}{3} \tag{3.4}$$

The incident and escape angles are independent from each other, thus the average energy gain:

$$\frac{E_2 - E_1}{E_1} = \frac{1 - \beta\cos\theta_1}{1-\beta^2} - 1 = \frac{1 - \frac{\beta^2}{3}}{1-\beta^2} - 1 \tag{3.5}$$

The magnetic clouds are non-relativistic thus:

$$\frac{E_2 - E_1}{E_1} \sim \frac{4}{3}\beta^2 \tag{3.6}$$

The energy gain due to this Fermi mechanism is second order function of the magnetic cloud velocity. The spectrum of cosmic ray particles can be calculated by solving the diffusion equation. The integral spectral index in the solution is inversely proportional to the energy gain:

$$\Gamma \sim \frac{1}{\frac{4}{3}\beta^2} \tag{3.7}$$

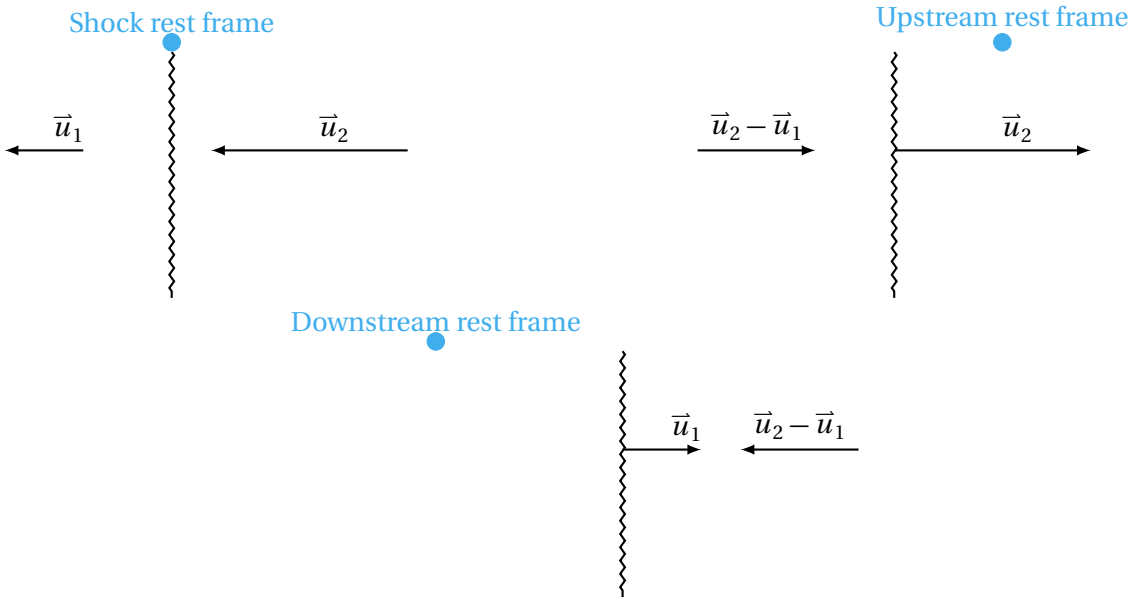

Figure 3.2 Different reference frames for the shock wave acceleration mechanism.

3.1.2 1st order Fermi acceleration

The 2nd order Fermi mechanism is ineffective, because depending on the collision, the energy can be gained or lost. In the 1st order Fermi mechanism, the downstream and upstream gas collide at the shock front. It can be seen in Figure 3.2 In the shock rest frame, both gases move to the same direction, different velocities. From upstream and downstream rest frames, respectively, the downstream and upstream gas seems coming closer. Thus particles on both sides of the shock front, sees the collision as head-on. In the rest frame of the downstream gas, the gas behind the shock front has an apparent velocity equal to $\vec{u}_2 - \vec{u}_1$. The upstream gas, in its' own rest frame sees the same. Thus it is possible to describe the acceleration mechanism with the same Equation 3.3 but in this case $\vec{V}=\vec{u}_2 - \vec{u}_1$. As in 2nd order Fermi acceleration, the average energy gain is required. In this case one can imagine an isotropic flux approaching the shock front with an angle $\theta_2^{'}$. The actual flux which traverses the shock front area depends on this angle. Thus the normalized probability for the particles to escape the shock front with an angle $\theta_2^{'}$ is $2\cos\theta_2^{'}$ and the average escape angle:

$$\langle \cos\theta_2^{'} \rangle = \frac{\int_0^1 \cos\theta_2^{'} 2\cos\theta_2^{'} d\cos\theta_2^{'}}{\int_0^1 2\cos\theta_2^{'} d\cos\theta_2^{'}} = \frac{2}{3} \tag{3.8}$$

For the incoming particle, the same logic can be applied but the integral is for $-1 \leq cos\theta_1 \leq 0$ and thus $\langle \cos\theta_1 \rangle = -\frac{2}{3}$. The average energy gain is:

$$\frac{E_2 - E_1}{E_1} = \frac{1 + \frac{4}{3}\beta + \frac{4}{9}\beta^2}{1-\beta^2} - 1 \sim \frac{4}{3}\beta = \frac{4}{3}\frac{u_2 - u_1}{c} \tag{3.9}$$

The integral spectral index for this accelerations mechanism is (given in [31]):

$$\Gamma \sim \frac{3}{\frac{u_2}{u_1} - 1} \tag{3.10}$$

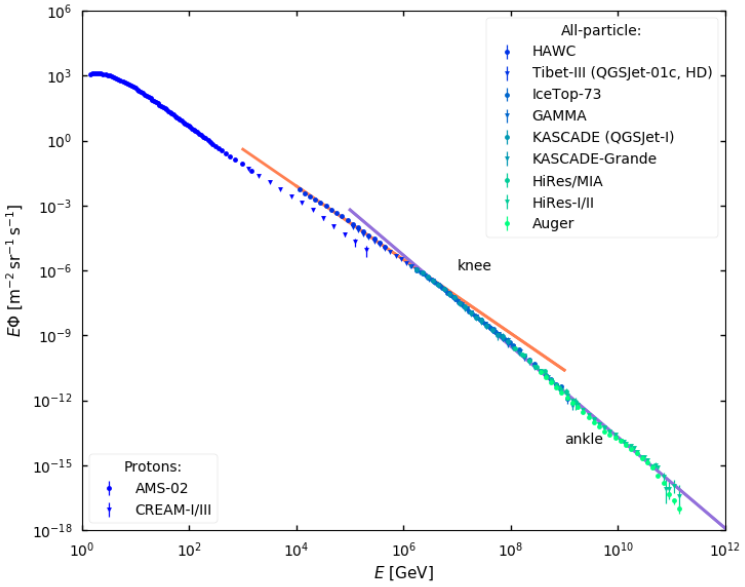

Figure 3.3 Cosmic ray flux of different particle species produced using the following experimental data: Auger [32], AMS-02 [33], CREAM-I/III [34], GAMMA [35], HAWC [36], HiRes/MIA [37], HiRes-I and HiRes-II [38], IceTop-73 [39], KASCADE [40], KASCADE-Grante [41], Tibet-III [42]. The orange line represents differential specral index $\alpha = -2.7$, violet - $\alpha = -3.1$

3.1.3 The cosmic ray spectra

The measured cosmic ray spectra for different particles can be seen in Figure 3.3. It can be very well described by power law of energy. The orange line represents a power law with a differential spectral index $\alpha = -2.7$ and this function can explain the data from 10 GeV to 1 PeV. From 10 PeV to 1EeV the index changes to $\alpha = -3.1$ and is violet line represents this regime. The part between these two different index regions is called the knee. Above 10 EeV the spectra can be reproduced with spectral index $\alpha = -2.6$. The energies, at which the spectral index changes in this case is called the ankle [31]. The origin of the knee and ankle is not very well understood. The energies reached before the knee can be explained by shock acceleration in supernova explosions. The particles with higher energy than the ankle are believed to come from extra-galactic sources. The energies important to indirect dark matter search are very low compared to these scales, thus only the supernovae sources are of interest.

3.2 The Galaxy Setup

Low energy cosmic rays which reach earth are produced in Milky Way galaxy and propagate through its' interstellar medium. Understanding the "setup" of our galaxy is important for indirect dark matter search as it defines the physics behind the measured fluxes. As mentioned before, cosmic rays originate from supernova explosions. While travelling in the galaxy, they interact with the interstellar medium.

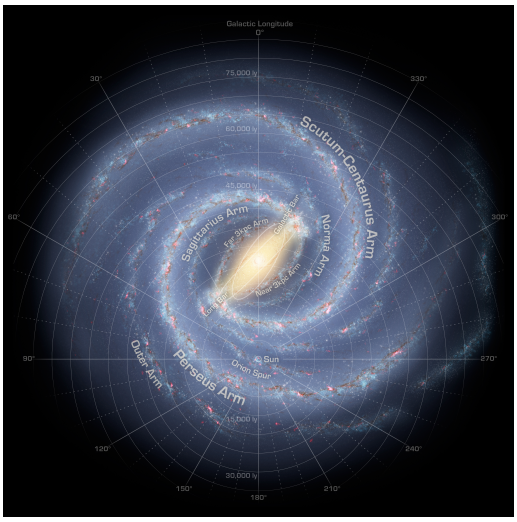

(a) Artist view of the Milky Way galaxy. (NASA/JPL-Caltech/R. Hurt (SSC/Caltech))

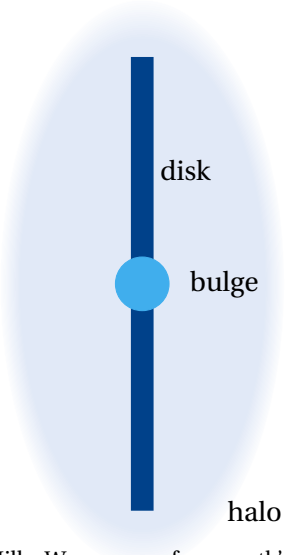

(b) The Milky Way as seen from earth's line of sight. The separate parts are not to size.

Figure 3.4 The Milky Way galaxy.

3.2.1 The Milky Way

The Milky way is a barred spiral galaxy as seen in Figure 3.4a. As shown in Figure 3.4b, it consists of [31]:

1. a thin disk (20 kpc radius and 400-600 kpc thickness);
2. a galactic center also called the bulge (2-3 kpc radius);
3. a spheroidal halo of old stars and globular cluster (30kpc minor axis).

The disk consists of the stars and the interstellar medium (ISM). The dust, gas and cosmic rays makes up the matter component of the ISM. The magnetic fields in the galaxy are part of the ISM as well. The Sun lies in the Orion Arm, in the Local Interstellar Cloud. The precise distance between the sun and the galactic center is not known as multiple analysis give different results, but the values range between 7 kpc and 9 kpc [43]. The standard value is considered to be 8.5 kpc.

3.2.2 Interstellar medium

As mentioned before, the interstellar medium consists of dust, gas, cosmic rays and magnetic fields. Even though the interstellar dust makes up only about 1% of the ISM, it plays a crucial role in the formation of stars [44]. The dust originates from material ejected by stars: in stellar explosions, by stellar winds, by radiation pressure. The ejecta consists mainly of silicate and graphite grains which later can grow by interacting with the most abundant elements in ISM as hydrogen, oxygen or nitrogen.
The gas exists in the form of interstellar clouds, intercloud medium and coronal gas. The composition of the gas is:

1. Hydrogen (90%)

(a) Neutral hydrogen

(b) Molecular hydrogen

(c) Ionized hydrogen

2. Helium (9%)

3. Other atoms, ions and molecules (1%)

These gasses make up 99% of the interstellar medium and they interact with the cosmic rays producing new particles. Their distribution in the galaxy can be mapped using spectroscopy. Hydrogen distributions are shown in the Figure 3.5.

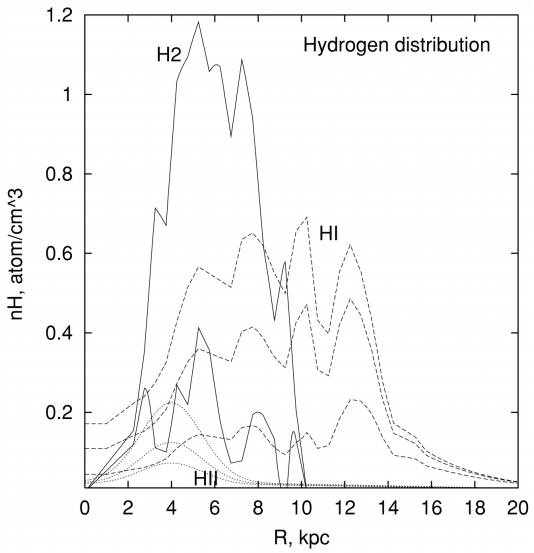

Figure 3.5 The hydrogen distributions in the galaxy as a function of the distance from the galaxy center. Decreasing density lines are for z = 0, 0.1, 0.2 kpc. Taken from [45]. The mathematical models can be found in the same paper, appendix A.

Neutral hydrogen - HI

Neutral hydrogen can be observed by detecting the 21 cm hyperfine line [46]. The energy of the ground state of the neutral hydrogen depends on the spin alignment of the proton and the electron. The parallel spin configuration is slightly higher in energy. Thus when the electron spin flips in neutral hydrogen, energy corresponding to 1420 MHz radiation is released and can penetrate the dust clouds and be detected. Absorption studies are possible as well [44]. The tabulated neutral hydrogen distribution as a function of the distance from the galaxy center can be found in [47]. The vertical distribution of the neutral hydrogen can be found in [46] for $R < 8$kpc and in [48] for $R > 10$kpc. All mentioned distributions are obtained by measuring the 21 cm hyperfine line. In Moskalenko et al paper [45], all this data is used to derive the spacial distribution of neutral hydrogen as a function of the distance from the galaxy center and the distance from the galactic plane. The resulting distribution can be seen in Figure 3.5 as dashed lines.

Molecular hydrogen - H2

Since there is no radiative transition between the two possible molecular H_2 states (ortho- and parahelium)[49], the direct astronomical detection of molecular hydrogen is very difficult. But the distribution of H2 can be extracted from the measurements of carbon monoxide (CO) molecule. The ratio of the molecular hydrogen mass and CO luminosity is approximately constant and can be used as conversion factor [50]. The molecular hydrogen distribution from CO survey can be found in [51]. In the Moskalenko et al paper this distribution has been expressed as a function of the distance from the galaxy center and the distance from the galactic plane. The resulting distribution can be seen in Figure 3.5 as solid lines.

Ionized hydrogen - HII

Very hot young starts of O and B spectral types emit photons which ionize the surrounding hydrogen gas and heats it up. The electrons captured by hydrogen nuclei can have different energy levels. The HII regions can be mapped by looking at the emission lines from electronic transitions to lower energy levels until the ground state is reached. Different measurements are available as well, for example pulsar dispersion measure and radio-wave scattering. Data from such experiment was used by Cordes et al. to define the galactic distribution of free electrons [52]. In the Moskalenko et al paper this distribution has been expressed as a function of the distance from the galaxy center and the distance from the galactic plane. The resulting distribution can be seen in Figure 3.5 as dotted lines.

Galactic magnetic fields

The origin of galactic magnetic fields is not well understood. The first theories suggested purely primordial origin but they predicted 50 to 100 times too strong magnetic fields thus this idea was assumed to be wrong [53]. Current theories suggest that ionized gas in ISM can amplify weak initial magnetic fields. The hydrodynamic motion of plasma acts as a dynamo and with time the field stabilizes [54]. The physics of such processes is described by magneto-hydrodynamics (MHD).
Multiple techniques exist to measure the magnetic field of Milky Way - analyzing the polarization of starlight, the Zeeman splitting of 21 cm neutral hydrogen line and the synchrotron emission of electrons spiraling in the galactic magnetic field. The strength of Milky Way large scale magnetic field is estimated to be around $2.5\text{x}10^{-10}$T [44]. The small scale magnetic fields can be up to 3 times stronger [55].

3.2.3 Supernovae and their distribution in the galaxy

Molecular clouds have temperatures of 10 K - 50 K thus regions of higher density are formed. If the gravitational force in a region is higher than the opposing forces, the molecular cloud implodes and forms a star [56]. Every star changes in time and this process is called stellar evolution.
Supernova explosions can be caused by two scenarios. White dwarfs have inactive carbon-oxygen cores. If a white dwarf accretes mass from its companion in a binary star, its core can ignite. This causes thermal runaway reactions and the core undergoes a thermonuclear explosion. The core is supported only by the degenerate-electron pressure. In non-degenerate

stars, the energy released in thermonuclear reactions can be dealt with by thermal expansion. But the degenerate-electron pressure does not depend on the temperature and thus the core temperature increases freely, accelerating the thermonuclear reactions even more. When the temperature becomes high enough to create a thermal pressure comparable with the degenerate-electron pressure, the star starts expanding. If the thermonuclear flame propagating outwards becomes supersonic, the core detonates causing a shock wave [57]. The other scenario happens when the gravity pressure in a massive star core exceeds the thermal pressure. Massive stars are supported mainly by thermal pressure. Hydrogen is fused in star core, releasing a lot of energy and inducing helium fusion. This chain stops when iron is produced because iron fusion absorbs energy. The thermal pressure starts to gradually decrease until it becomes smaller than gravity pressure. The collapse of the core increases the density in inner layers of the core so much, that the iron nuclei breaks up to helium and neutrons and emits energy. The increased thermal pressure stops the collapse of the inner core and the outer core material bounces off it causing a shock wave [58].
As explained in section 3.1.2, these shock waves accelerate the cosmic rays. These cosmic rays have to propagate trough the galaxy to reach a detector in the solar system. To solve the differential transport equation, source spectra are currently implemented according to the 1st order Fermi acceleration. The distribution of the supernovae must be measured.
The result of supernova explosion is the supernova remnant (SNR) that is an expanding nebula consisting of the interstellar medium particles swept by the shock wave and the ejecta of supernova itself. There are three types of remnants. In the thermonuclear supernova, the star is destroyed completely resulting in a nebula without a star in the center called shell type remnant. In the collapse supernova, the inner core forms a neutron star. The final result might be either plerion - a nebula powered by pulsar winds - or a composite remnant - the mixture of the plerion and shell remnants. The shell SNRs can be detected by radio-frequency absorption-line observations. The radial distribution of shell SNRs is parametrized as surface density and this have been done by Case and Bhattacharya [59]. The other type SNRs can be mapped using the pulsars by measuring their emitted electromagnetic waves concentrated in the gamma-ray band. The Energetic Gamma Ray Experiment Telescope (EGRET) mapped the high energy gamma ray sky. The distribution of cosmic ray sources can be derived to reproduce the cosmic ray distribution obtained from the EGRET data [60]. This was done by A. Strong and I.Moskalenko in [61]:

$$\rho(R,z) = \rho_0 \left(\frac{R}{R_{sun}} \right)^a \exp\left[-b \left(\frac{R - R_{sun}}{R_{sun}} \right) - \frac{|z|}{z_0} \right] \tag{3.11}$$

The radial part of this distribution as well agrees with newest measurements of SNRs and pulsars [62]. As it is explained in [61]: "The z-dependence of ρ is nominal and simply reflects the assumed confinement of sources to the disk."

3.3 Cosmic Ray Propagation

Cosmic ray particles, before they are detected, travels through the galaxy, heliosphere and earths' magnetic field and the atmosphere. The processes of cosmic ray propagation in these environments are described in this chapter.

3.3.1 Galaxy

The cosmic ray flux at certain position and time can be calculated by solving the transport equation:

$$\frac{\partial \psi}{\partial t} = q(\mathbf{r},p) + \mathbf{div}(D_{xx}\mathbf{grad}\psi - \mathbf{V}\psi) + \frac{\partial}{\partial p}p^2 D_{pp}\frac{\partial}{\partial p}\frac{\psi}{p^2} - \frac{\partial}{\partial p}\left[\psi\frac{dp}{dt} - \frac{p}{3}(\mathbf{div}\cdot\mathbf{V})\psi\right] - \frac{\psi}{\tau_f} - \frac{\psi}{\tau_r} \tag{3.12}$$

The physical meaning of separate terms in this equation is [63]:

- $q(\mathbf{r},p)$ - the source function. It can be the primaries (particles accelerated in supernovae) or secondaries (produced in cosmic ray collisions with ISM gas, nuclear fragmentation products). It can include exotic sources as well.
- $\mathbf{div}(D_{xx}\mathbf{grad}\psi)$ - the diffusion term. Particles diffuse to lower density regions. D_{xx} is the spatial diffusion coefficient.
- $\mathbf{div}(\mathbf{V}\psi)$ - the convection term. The convection is caused by Galactic winds which blow the charged particles out from the disk to halo or even to intergalactic medium. $\mathbf{V}$ is the convection velocity.
- $\frac{\partial}{\partial p}p^2 D_{pp}\frac{\partial}{\partial p}\frac{\psi}{p^2}$ - the diffusive reacceleration term. The process is explained by charged particle reacceleration in magnetic clouds by 2nd order Fermi acceleration. D_{pp} is the momentum diffusion coefficient.
- $\frac{\partial}{\partial p}\psi\frac{dp}{dt}$ - the momentum losses via ionization and bremsstrahlung.
- $\frac{\partial}{\partial p}\frac{p}{3}(\mathbf{div}\cdot\mathbf{V})\psi$ - adiabatic momentum losses. It depends on the convection velocity so it is related to Galactic winds as well. The energy loss is based on the 1st order Fermi acceleration. (If energy is lost or gained depends on the sign of $\mathbf{div}\cdot\mathbf{V}$.
- $\frac{\psi}{\tau_f}, \frac{\psi}{\tau_r}$ - the fragmentation and decay of the cosmic ray particles.

In addition to these processes, cosmic ray particles can interact with the ISM gas.
The simplest model, an approximation of equation 3.12, assumes that cosmic rays can propagate freely in a confined volume with a probability to escape and is called leaky box model. In this model the diffusion and convection terms are exchanged with a characteristic escape time: $\frac{\psi}{\tau_{esc}}$. The spallation and source terms are still included but the system is assumed to be in equilibrium - the time derivative is equal to 0. This model is important because it provides simplified predictions for secondary to primary ratios which depends on the characteristic escape time and thus provides good check of the diffusion and convection terms. Usually the boron to carbon ratio is used as it is not abundant in primary cosmic rays thus being purely secondary in oxygen and carbon spallation. The model gives prediction for boron to carbon ratio using the fact that the flux of carbon and oxygen are nearly the same and boron is stable (as given in [31]):

$$\frac{\psi_B}{\psi_C} \approx \frac{\lambda_{esc}(E)}{1+\lambda_{esc}(E)/\lambda_B}\frac{\sigma_{C\to B}+\sigma_{O\to B}}{m_p} \tag{3.13}$$

$\sigma_{O\to B}$ is the boron cross section from oxygen and $\sigma_{C\to B}$ is from carbon. The average amount of traversed matter is related to the escape time $\lambda_{esc}(E) = \beta c \rho \tau_{esc}(E)$, β is the velocity of the

particle, c - speed of light, ρ - the density of interstellar medium, m_p is the proton mass. Thus measuring the boron to carbon ratio gives direct access to energy dependence of diffusion and convection parameters.
The equation 3.12 can be solved numerically as well. Several packages are available, for example GALPROP.

3.3.2 Heliosphere

Cosmic rays are influenced by the solar wind and the magnetic field of the sun. The sun can be modelled as hot ionized gas - plasma. Similarly, to the galactic magnetic field, the solar magnetic field is continuously regenerated by the movements of plasma in convection zone - the dynamo mechanism [64]. The strength of this magnetic field has an 11 years cycle while the polarity of solar magnetic field reverses every 22 years. The charged particles ejected from the corona (upper part of the sun's atmosphere) and moving away from the sun are called solar wind. The moving plasma carries magnetic field as well. The solar activity is usually measured in two ways - sunspot number and neutron monitoring. The sunspots are temporary lower temperature regions in Sun's photosphere caused by the magnetic field flow. The increasing number of these sunspots implies an increasing magnetic field of the sun and vice versa [65]. This process is monitored by measuring the neutron flux reaching the earth. Most of these neutrons are secondaries from primary cosmic ray interactions with the earth's atmosphere. The amount of such primaries depends on the solar modulation. Thus, for a known local interstellar flux, it is possible to tune the solar modulation parameters using neutron monitoring data as the measured neutron flux depends on how many primaries are able to propagate trough the heliosphere and reach the earth's atmosphere.
The process of solar modulation can be described very similarly to the galactic propagation [66] [67]:

$$\frac{\partial \psi}{\partial t} = \mathbf{div} \cdot (\kappa \cdot \mathbf{grad} \psi) - (\mathbf{V} + \mathbf{V}_D) \cdot \mathbf{grad} \psi + \frac{p}{3} (\mathbf{div} \cdot \mathbf{V}) \frac{\partial \psi}{\partial \ln p} \tag{3.14}$$

κ is the diffusion tensor, $\mathbf{V}$ is the solar wind velocity, $\mathbf{V}_D$ is the drift velocity of the particle in the heliospheric magnetic field, p is the momentum of the particle and the full term stands for adiabatic momentum losses.
The solution of this equation is rather complicated and usually it is solved numerically. Very popular way to account for solar modulation is using force field approximation introduced by Gleeson and Axford [68]. It works under certain assumptions: the drift is neglected, the cosmic ray distribution is spherically symmetric, the solar wind is moving radially with constant speed and the diffusion tensor is isotropic. The system is in steady state ($\frac{\partial \psi}{\partial t} = 0$). The cosmic ray flux after the solar modulation can be calculated using only one parameter - the solar modulation potential - applied on the local interstellar flux (LIS):

$$J(E_{kin}, \phi) = J_{LIS}\left(E_{kin} + \frac{Ze}{A}\phi\right) \frac{E_{kin}(E_{kin} + 2m)}{\left(E_{kin} + \frac{Ze}{A}\phi\right)\left(E_{kin} + \frac{Ze}{A}\phi + 2m\right)} \tag{3.15}$$

J is the cosmic ray flux at earth's proximity, J_{LIS} is the local interstellar flux, E_{kin} - the kinetic energy, m - the mass (rest energy), Z and A - the charge and mass numbers of a particle. The ϕ is the solar modulation potential. The force field approximation works only for high energy particles and it is particle charge-sign and magnetic field polarity independent. Low energy cosmic rays require the numerical solution of the heliospheric transport equation.

3.3.3 Earth's atmosphere and magnetic field

The last component of cosmic ray propagation is the earth's environment which consist of magnetic field and the atmosphere. The magnetic field consists of internal and external parts. The origin of internal magnetic field is believed to be similar to the galactic and heliospheric magnetic fields - the generation by dynamo effect occurring in the core of earth. The external field is created by electric charges in the ionosphere [69]. Differently from the galactic and solar cases, the hadronic interactions are a lot more probable as the atmosphere is very dense compared to interstellar or interplanetary medium. The propagation part consists again of diffusion and convection in the magnetic field, but in this case it is common to use models of the geomagnetic field and use Monte Carlo simulations to propagate particles step by step while the hadronic and electroweak interactions must be included using Monte Carlo generators for particle shower creation. In the collisions of cosmic rays and atmospheric particles both leptons and hadrons can be produced as well as their antiparticles. More about the effects of atmosphere and geomagnetic fields on the cosmic ray flux will be described in section 5.4 .

3.4 Cosmic Ray Measurements

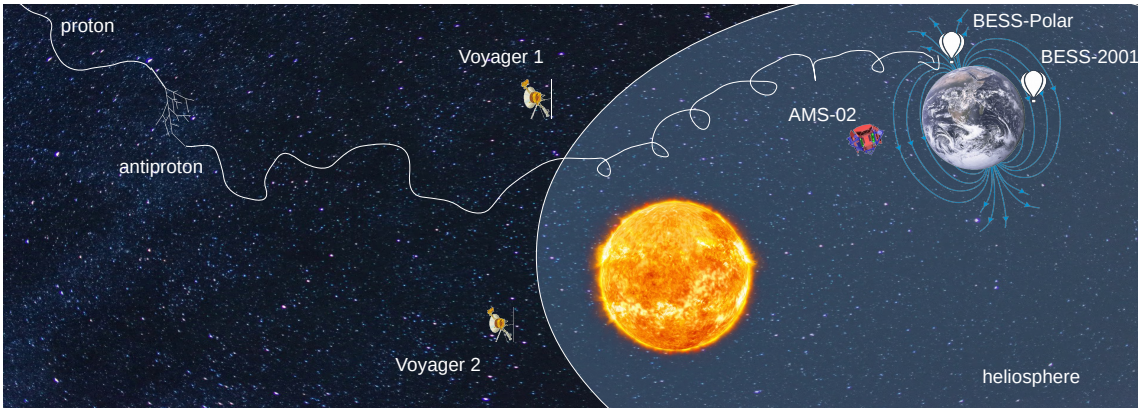

Figure 3.6 The location of cosmic ray detectors. Not up to scale.

Transport equations in general have several parameters which define the diffusion, convection and other propagation components. They are not observables which can be measured. The cosmic ray fluxes for different particle species at different positions and at different times are measured instead. The propagation of cosmic rays is solved numerically and the parameters of the models are chosen by fitting procedures. The final simulated flux is fitted to the measured flux. To constrain every single part of the propagation chain consisting of the galaxy's, the sun's and the earth's environments, the measurements are required at every single component. In this thesis several experiments will be used to restrict the parameters:

- Local interstellar flux (LIS) - Galactic propagation
  - Voyager probes - low energy cosmic ray flux.
  - Cosmic Ray Energetics and Mass experiment (CREAM-III) - high energy cosmic ray flux.

- Top of the Atmosphere flux (TOA) - Solar modulation
  - Alpha Magnetic Spectrometer (AMS-02).
  - Balloon-borne Experiment with Superconducting Spectrometer (BESS) Polar.
- Flux inside earth's environment
  - Balloon-borne Experiment with Superconducting Spectrometer (BESS) 2001.

3.4.1 Local interstellar flux

The local interstellar flux is the galactic flux not influenced by solar or planetary magnetic fields. For low energy particles the flux must be measured outside the heliosphere. The solar modulation of high energy particles is extremely small thus the flux can be measured inside the heliosphere.

Voyager

The twin spacecraft Voyager 1 and Voyager 2 had a mission to explore the solar system outer planets and now it is exploring the interstellar medium. The probes were launched in 1977 and are still sending valuable data to earth. Onboard instruments include the two High Energy Telescopes (HET-I and HET-II) and the four Low Energy Telescopes (LET A,B,C, and D).

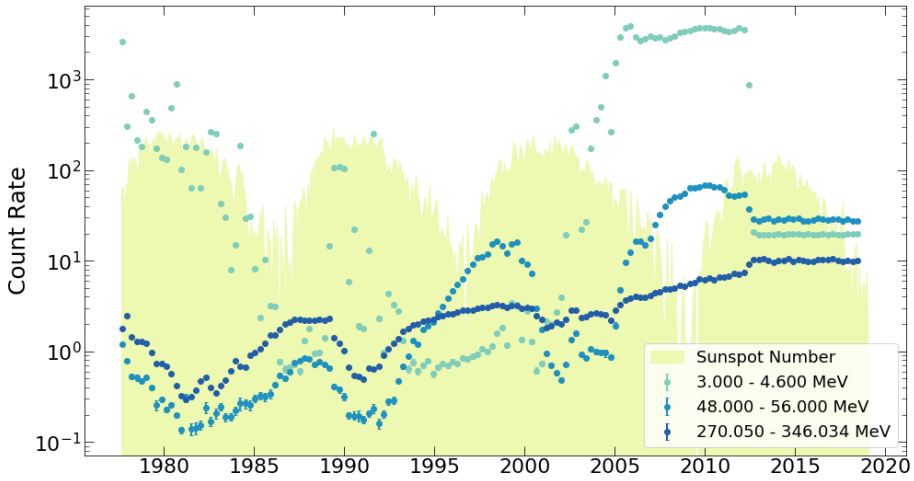

Figure 3.7 The time dependence of the count rate of the cosmic ray protons measured by Voyager. The light green region shows sunspot number in arbitrary units from SILSO database: http://sidc.be/silso/home.

They consist of a multi-element stack of solid state detectors and measure the cosmic ray fluxes of several particle species including proton, helium, carbon and boron. The cosmic ray fluxes of hydrogen and helium are accessible online on NASA's website: https://voyager.gsfc.nasa.gov/spectra.html. The cosmic ray flux rates in time can be found https://voyager.gsfc.nasa.gov/flux.html. The

following information can be used to evaluate if the detector is outside heliosphere. The proton count rates measured by Voyager 1 are shown in Figure 3.7 for three different energy bins. It can be seen that during periods of low solar activity (low number of sunspots), the proton number increases. After the year 2012 the count rate becomes steady and is not influenced by solar modulation - the probe is outside the heliosphere. The increase of the count rate just before leaving the heliosphere comes from the so called hydrogen wall - protons accumulated at the limit between heliopause and the bow shock. Voyager 1 measures particles in energy range between 3 MeV and 661.40 MeV. In this thesis the data averaged in the period between 2017-01-01 and 2018-10-12 is used.

CREAM-III

The Cosmic Ray Energetics and Mass (CREAM) experiment goal was to measure high energy cosmic ray particles. It is a balloon-borne experiment and the flights were conducted on several occasions from 2004 to 2016. The third flight (CREAM-III) was launched in Antarctica on 2007-12-19 and it landed on 2008-01-17. The float altitude was between 37 and 40 km. The proton flux was measured in kinetic energy range from 10^3 GeV to 2.51×10^6 GeV; the helium flux - from 2.51×10^2 GeV/n to 6.31×10^4 GeV/n [34]. CREAM uses a silicon charge detector, timing charge detector, and scintillating fiber hodoscopes to measure the charge of an incident particle. A transition radiation detector (TRD) and an ionization calorimeter are used to measure the energy of the particle.

3.4.2 Top of the atmosphere flux

The top of the atmosphere flux is the flux propagated through the galaxy and the heliosphere. The measurements must be conducted either outside the geomagnetic field or where it is extremely small and the density of the atmosphere must be low. It can be either balloon-borne or satellite experiment.

AMS-02

The Alpha Magnetic Spectrometer (AMS-02) is a state-of-the-art particle detector operating on the International Space Station (ISS). The detector accepts only particles coming from top to bottom and its anti-coincidence counter rejects particles entering through the sides. The time of flight detector measures the velocities of the low energy particles; the transition radiation detector - the velocities of the highest energy particles. The ring imaging Cherenkov detector extremely accurately measures the velocity of fast particles. The total energy of the particles is measured using the electromagnetic calorimeter. The AMS-02 contains a permanent magnet which bounds the charged particles and the silicon tracker measuring the coordinates of these charged particles. The tracks of the charged particles in the magnetic field are used to identify the particles. The AMS-02 was launched on the Space Shuttle Endeavour on May 16, 2011.
The AMS-02 collaboration published antiproton and proton flux data. The proton flux is based on the measurements conducted from 2011-05-19 to 2013-11-26 in kinetic energy range from 0.49 GeV/n to 1416.32 GeV/n [70]. The antiproton flux is based on the measurement conducted from 2011-05-19 to 2015-05-26 in kinetic energy range from 0.49 GeV/n to 353.56 GeV/n [71].

BESS-Polar

The Balloon-borne Experiment with Superconducting Spectrometer Polar flights were conducted above Antarctica. The first flight (BESS-Polar I) was launched on 2004-12-13 and lasted for 8.5 days. The balloon flew at the altitudes from 37 km to 39.5 km and geomagnetic cutoff rigidity below 0.2 GV. The cutoff rigidity ($R = p/q$ - p is the momentum; q is the charge) is a limit for cosmic ray particle energy, below which the particles are reflected by geomagnetic field. The second flight (BESS-Polar II) was launched on 2007-12-23 and lasted for 24.5 days. It flew at the altitudes from 34 km to 38 km and cutoff rigidity below 0.5 GV.
The published proton flux covers the range from 0.2 GeV to 166.8 GeV [72]. The antiproton flux from Polar-I flight was published for kinetic energies from 0.1 GeV to 4.20 GeV; from Polar-II from 0.17 GeV to 3.46 GeV [73] [74].

3.4.3 Particle flux inside the earth's environment

To see the influence of the geomagnetic field and the particle interactions in the atmosphere, the experiment must be conducted at high geomagnetic cutoff rigidity and low altitudes.

BESS-2001

The BESS-2001 balloon flight was launched at Ft. Sumner, New Mexico, USA on 2001-04-24 and lasted for one day. It reached 36 km altitude and during the flight the cutoff rigidity was about 4.2 GeV. The published proton data is for the energy range from 0.46 GeV to 10.00 GeV separately for different atmospheric depths [75].

Chapter 4

Hadronic Interactions of Cosmic Rays

The presence of the antimatter in cosmic rays is either due to exotic sources or due to cosmic ray interactions with interstellar medium. In the following chapter the production of antiprotons in different collision systems are discussed.
Particle collisions can be either elastic or inelastic and can be quantified by measuring cross sections. In elastic collisions the particles bounce off each other without creating new particles while in the case of inelastic collision new particles are produced.
In cosmic ray studies, one is not interested in the total inelastic cross section but in the antiproton production cross section. The inclusive invariant differential cross section is required:

$$f = E\frac{d^3\sigma}{dp^3} \tag{4.1}$$

This can be understood as the probability to produce an antiproton of the energy E and the momentum p in a collision and this quantity is invariant under Lorentz transformation. An inclusive antiproton production cross section means that all reactions producing at least one antiproton are included no matter what the rest of the products are: $p + p \rightarrow \bar{p} + X$.
Other important variables in this chapter will be longitudinal (p_L) and transverse (p_T) momentum. The coordinate system of the collision is usually chosen in such a way that the z direction is parallel to the beam axis. The longitudinal momentum in such cases is the p_z component of momentum. The transverse momentum is the momentum of the particle in the transverse plane with respect to the beam axis:

$$p_T = \sqrt{p_x^2 + p_y^2} \tag{4.2}$$

$$p_L = p_z \tag{4.3}$$

In 1969 Feynman introduced the parton model [76]. A particle, for example a proton, within this framework is composed of partons (quarks and gluons). At low collision energy, the resolution is bad and only the valence quarks can be resolved. The resolution increases with the collision energy because of Heisenberg's uncertainty principle and the quark and gluon sea can be resolved at very high energies. The longitudinal momentum of the particle is distributed between these partons. The probability to find a parton with certain longitudinal momentum can be described by parton distribution function. This function depends on so called Feynman

scaling variable which shows the longitudinal momentum fraction carried by parton:

$$x_f = \frac{p_L^*}{2\sqrt{s}} \tag{4.4}$$

p_L^* is the longitudinal momentum in center-of-mass frame and s is the center of mass energy. The momentum distribution of the partons depends not on the collision energy, but only on the momentum fraction carried by parton. For produced particles, the Feynman scaling variable shows what longitudinal momentum fraction was transferred. It is called scaling variable because at high energies the inclusive invariant cross section does not depend on the collision energy if it is expressed in terms of p_T and x_F:

$$f = E\frac{d^3\sigma}{dp^3} = \frac{E}{\pi}\frac{d^2\sigma}{dp_L dp_T^2} = \frac{2E}{\pi\sqrt{s}}\frac{d^2\sigma}{dx_F dp_T^2} \tag{4.5}$$

Thus the momentum distribution of produced particles can be deduced from one collision energy and used for the rest:

$$f(\sqrt{s}, x_F, p_T) \rightarrow f(x_F, p_T) \tag{4.6}$$

Another possible scaling variable is x_R:

$$x_R = \frac{E^*}{E_{max}^*}, \text{ where } E_{max}^* = \frac{s - M_X^2 - m^2}{2\sqrt{s}} \tag{4.7}$$

E^* is the energy of the particle in center-of-mass frame; E_{max}^* is the maximum energy a particle could have. M_X^2 is the minimal mass of the recoiling particles. The radial scaling variable describes the phase space suppression because of the kinematic boundary - the probability to produce a particle with energy close to E_{max} is really small. Similarly to x_F, the invariant cross section at high energies does not depend on the collision energy. x_R scaling is valid at energies higher than 10 GeV. [77]
One more way to describe particle production in collisions is using differential multiplicity, defined as:

$$\left(\frac{d^3n}{dp^3}\right) = \frac{1}{\sigma_{inel}}\left(\frac{d^3\sigma}{dp^3}\right) \tag{4.8}$$

n is the multiplicity; σ_{inel} - the total inelastic cross section.
The theoretical predictions for the invariant cross section is given by constituent exchange model. Baryons and mesons are made up of quarks. The constituent exchange model states, that particles in a collision interact by exchanging either valence or sea quarks or gluons and in this way the new particles are created. Annihilation might occur instead of exchange. The interacting quark fragmentation creates light-cone shaped jets. The momentum distribution of the created fragments can be calculated using the dimensional-counting rule. This gives a prediction for the invariant cross section of produced particles:

$$f \propto (1-x)^n, \tag{4.9}$$

n is the fragmentation power and is defined by the dimensional counting rule. It depends on the minimal number of spectator quarks required to fullfil the quantum number conservation requirements. In case of $p + p \rightarrow \bar{p} + X$, the quark exchange model predicts n=9 [78]. x is the momentum fraction of the jet which is directly not observed but is approximately equal to x_R. Based on the constituent exchange model, several parametrizations for the invariant antiproton production cross section exist.

4.1 p+p collisions

In this work we compared two different parametrizations of invariant inclusive cross section. Both of them are based on the constituent exchange model. The first one was published by L.C.Tan and L.K. Ng in 1983 when the high energy data was not available [79]. It will be referred to it as Tan and Ng parametrization. The newer parametrization was suggested by M. W. Winkler and R. Kappl in 2014 (updated by M. W. Winkler on 2017) and will be referred to as Winkler parametrization [80] [81]. Within the scaling hypothesis, it was assumed that at high energies the total inelastic cross section becomes constant but the high energy collision measurements showed that σ_{inel} increases with the collision energy. This effect is included in the Winkler parametrization.
So far, only the prompt production of antiprotons was mentioned but antiprotons can be produced in antiproton and antihyperon decays as well. All possible antiproton production channels are:

$$p + p \rightarrow \bar{p} + X \tag{4.10}$$

$$p + p \rightarrow \bar{n} + X, \quad \bar{n} \rightarrow \bar{p} + e^+ + \nu_e \tag{4.11}$$

$$p + p \rightarrow \bar{\Lambda} + X, \quad \bar{\Lambda} \rightarrow \bar{p} + \pi^+ \tag{4.12}$$

$$p + p \rightarrow \bar{\Sigma}^- + X, \quad \bar{\Sigma}^- \rightarrow \bar{p} + \pi^0 \tag{4.13}$$

In the simplest case, isospin effects are neglected. For example, in the Tan and Ng parametrization, the antineutron production rates are considered to be equal to the antiproton rates and the hyperons are not considered at all. Winkler has data driven parametrization (described in section 4.1.2) of antineutron production including isospin effects and the antihyperon production.
For the cosmic ray studies, the antiproton production cross section parametrization is required as function of the kinematic variables. In this section we only introduce the parametrizations. Later on they are used in our analysis where we will present comparison to the experimental data.

4.1.1 Tan and Ng parametrization

The Tan and Ng parametrization is fitted to the inclusive invariant antiproton cross section in $p + p$ collisions measured at the CERN intersecting storage ring facility over the range $23\text{GeV} \leq \sqrt{s} \leq 62\text{GeV}$ [82].
The parametrization for the antiproton invariant inclusive cross section as a function of p_T and x_R:

$$f(x_R, p_T) = f(x_R) \exp\left(-\left(A(x_R)\, p_T + B(x_R)\, p_T^2\right)\right) \text{ [mbGeV}^{-2}\text{c}^3\text{]}, \tag{4.14}$$

where:

$$f(x_R) = 1.05 \cdot 10^{-4} \exp(-10.1\, x_R)\theta(0.5 - x_R) + (3.15 - 1.05)(1 - x_R)^{7.90} \tag{4.15}$$

$$A = 0.465 \exp(-3.7 \cdot 10^{-2} x_R) + 2.31 \exp(1.4 \cdot 10^{-2} x_R) \tag{4.16}$$

$$B = 3.02 \cdot 10^{-2} \exp\left(-3.19\,(x_R + 0.399)\right)(x_R + 0.399)^{8.39} \tag{4.17}$$

$$\theta(u) = \begin{cases} 0 & \text{for} \quad u < 0 \\ 1 & \text{for} \quad u \geq 0 \end{cases} \tag{4.18}$$

As mentioned before, at low energies only the valence quarks are resolved in a collision. Thus at $\sqrt{s} < 10$ GeV the momentum distribution of produced antiprotons starts depending not only on the transferred momentum fraction but on the collision energy as well. The radial scaling breaks down and the correction factor is required. At low energies the finite hadron mass must be considered thus the radial scaling variable must be changed to:

$$x_T = \frac{E^* - mc^2}{E^*_{max} - mc^2} \tag{4.19}$$

The flux must be multiplied by the correction factor R at $\sqrt{s} < 10$ GeV. Tan and Ng used the earlier mentioned CERN intersecting storage ring facility experimental data and parametrized $\frac{1}{R}$ as:

$$R^{-1} = 1 - \exp\Big(-\Big(1 - \exp\Big(-A(x_T)\big(\sqrt{s} - 6.566\big)^{B(x_T)}\Big)\Big)\exp\big(C(x_T)\big(\sqrt{s} - 6.566\big) - D(x_T)\big)\Big) \tag{4.20}$$

$$A = 0.306\exp(-0.120\,x_T) \tag{4.21}$$

$$B = 0.0552\exp(2.72\,x_T) \tag{4.22}$$

$$C = 0.758 - 0.680\,x_T + 1.54\,x_T^2 \tag{4.23}$$

$$D = 0.594\exp(2.87\,x_T) \tag{4.24}$$

4.1.2 Winkler parametrization

The Winkler parametrization is fitted to the NA49 measurements of pp collisions at a fixed target experiment with a beam momentum of 158 GeV/C [83]. Similarly to the Tan and Ng parametrization, the radial scaling is assumed for energies $\sqrt{s} > 10$ GeV and for the lower energies the correction factor is applied. Besides that, the main difference is that the total inelastic cross section is not assumed to be constant at high energies. The inclusive invariant antiproton production cross section is expressed as:

$$f(x_R, p_T) = 0.047 R \sigma_{\text{inel}} (1 - x_R)^{7.76} (1 + X(m_T - m))^{-\frac{1}{0.168X}}, \tag{4.25}$$

where m_T is the transverse mass and is equal to $\sqrt{m^2 + p_T^2}$. The correction factor for scaling violation is:

$$R = \left(1 + 1 \cdot 10^{-3}\left(10 - \frac{\sqrt{s}}{GeV}\right)^5\right)\exp\left(0.7\left(10 - \frac{\sqrt{s}}{GeV}\right)\big(x_R - x_{R,min}\big)\right) \tag{4.26}$$

the same as in Tan and Ng parametrization and is applied only for $\sqrt{s} \leq 10$ GeV. At higher energies $R = 1$. The σ_{inel} is taking care of the observed rise in total inelastic cross section at high energies:

$$\sigma_{inel} = 30.9 - 1.78\log\sqrt{s} + 0.72\log^2\sqrt{s} \tag{4.27}$$

Another scaling violation comes from X which accounts for the increase in cross section at large p_T:

$$X = 0.038\log^2\left(\frac{\sqrt{s}}{\sqrt{s}_{th}}\right) \tag{4.28}$$

The $\sqrt{s}_{th} = 4m$ is the threshold energy for antiproton production.
As mentioned before, all possible antiproton production channels have been included. Winkler assumes that the antiproton momentum distribution for all channels are the same thus the antihyperon and antineutron channels are included by scaling prompt antiproton channel:

$$f = f^0_{\bar{p}}(2 + \Delta_{\mathrm{IS}} + 2\Delta_{\bar{\Lambda}}) \tag{4.29}$$

The $2 + \Delta_{\mathrm{IS}}$ term accounts for the antineutron channel and includes the isospin asymmetry effects while $2\Delta_{\Lambda}$ accounts for antihyperon channel decaying to either $\bar{p}$ or $\bar{n}$. The Winkler parametrization for these variables is introduced below. Depending on the collision energy, the parametrization predicts the total antiproton multiplicity to be made up of: ≈37% prompt production, ≈45% antineutron decay and ≈ 18% antihyperon decay.

Antineutrons and isospin effects

Antiprotons can be produced in antineutron decay:

$$\bar{n} \rightarrow \bar{p} + e^+ + \nu_e \tag{4.30}$$

Baryon number conservation forces the baryon antibaryon production. Thus if an antiproton is produced in a collision, a neutron or a proton must be produced as well. The resulting final states are hence $\bar{p}n$ and $\bar{p}p$; and $\bar{n}n$ and $\bar{n}p$ in case of antineutron production. The $\bar{p}n$ and $\bar{n}p$ have opposite isospins. Depending on the isospins of the colliding particles, the production of one of them can be preferred thus creating asymmetry in the antineutron and antiproton yields. In case of $p + p$ collisions, the experimental data shows that $\bar{n}p$ final state is favoured thus producing more antineutrons than antiprotons. The difference can be parametrized and fitted to existing data from the NA49, Fermilab, STAR and ALICE experiments. The following formula is used [81]:

$$\Delta_{\mathrm{IS}} = \frac{f^0_{\bar{n}}}{f^0_{\bar{p}}} - 1 = \frac{c_1}{1 + \left(\frac{s}{c_2}\right)^{c3}} \tag{4.31}$$

In [81] only the upper limit for $c_2 < (100\ \mathrm{GeV})^2$ is given. We fit the function 4.31 to the data used by [81] and get $c_1 = 0.28$, $c_2 = 12.12$ and $c_3 = 1.04$.

Antihyperons

Antiprotons can be produced in the hyperon decays:

$$\bar{\Lambda} \rightarrow \bar{p} + \pi^+ \tag{4.32}$$

$$\bar{\Sigma}^- \rightarrow \bar{p} + \pi^0 \tag{4.33}$$

The ratio for antihyperon production can be defined as:

$$\Delta_{\Lambda} = \frac{\bar{\Lambda}}{\bar{p}} \times \mathrm{Br}\left(\bar{\Lambda} \rightarrow \bar{p} + \pi^+\right) + \frac{\bar{\Sigma}^-}{\bar{p}} \times \mathrm{Br}\left(\bar{\Sigma}^- \rightarrow \bar{p} + \pi^0\right) \tag{4.34}$$

The Br stand for the specific decay branching ratio. This ratio is a function of the collision energy. Using several experimental data results, Winkler comes to the parametrization [81]:

$$\Delta_{\Lambda} = 0.81\left(0.31 + \frac{0.3}{1 + \frac{(146\ \mathrm{GeV})^2}{s}}\right)^{0.9} \tag{4.35}$$

4.2 p+He, He+p and He+He collisions

The cosmic rays and the interstellar medium have not only a proton component, but helium and even heavier nuclei as well. The fractions of antiprotons produced in different collision systems depends on the used cross section model but on average the fractions summarized in Table 4.1 are obtained.

Table 4.1 Antiproton production contributions from different collision systems.

Collision	Antiproton fraction [%]
p+p	∼54
p+He, He+p, He+He	∼36
heavier nuclei	∼10

Winkler provides parametrization for the $p+A$ and $A+A$ collisions by introducing the projectile and target overlap functions. Another way to describe the antiproton production in such collision systems is to use Monte Carlo generators for particle production. Later on in our antiproton production analysis we use one of such parametrizations published Simon et al. [84]. In this chapter the Winkler and Simon et al parametrizations will be introduced.

4.2.1 Simon et al parametrization

Simon et al used a Monte Carlo model DTUNUC to study antiproton production in various collision systems. The resulting antiproton production cross section, the proton and helium interstellar local fluxes measured by the IMAX experiment [85] and the heavier nuclei local interstellar fluxes from the HEAO-C2 experiment [86] are used to calculate the antiproton source function for different collisions. The antiproton number in the galaxy depends not only on the antiproton production cross sections but on the amount of particles that collide - the cosmic interstellar flux of nuclei and the density of target particles in the interstellar medium. The antiproton source function thus is an integral over all cosmic ray particle species and all interstellar medium particles. It is the antiproton production cross section weighted by the number of collisions per unit volume per unit time ($\mathrm{cm^{-3}s^{-1}GeV^{-1}}$):

$$Q(E_{\mathrm{kin},\bar{p}}) = 2\sum_{j}^{ISM}\sum_{i}^{CR} 4\pi n_j \frac{d\sigma^{i,j}}{dE_{\mathrm{kin},\bar{p}}}(E_{\mathrm{kin},\bar{p}}, E_{\mathrm{kin},i}) I_i(E_{\mathrm{kin},i}) dE_{\mathrm{kin},i}, \tag{4.36}$$

where i is the projectile particle - cosmic ray particle; j is the target particle - interstellar medium particle; n_j is the density of target particles in the interstellar medium; $\sigma^{i,j}$ is the antiproton production cross section for $i+j$ collision; $E_{\mathrm{kin},\bar{p}}$ and $E_{\mathrm{kin},i}$ are the kinetic energy of the produced antiproton and the kinetic energy of the cosmic ray particle; I_i is the cosmic ray flux of i particle.
The shape of the antiproton source function for $p+p$ collisions is very similar to the shape of the antiproton source function for all colliding systems. Which means that the momentum distribution of antiproton flux doesn't change if all collision systems are included instead of only $p+p$. Thus it is possible to scale the antiproton cross sections for $p+p$ in a way, that the antiproton source function computed using only the scaled $p+p$ cross sections would agree with the local interstellar flux including all colliding systems. Simon at al published the

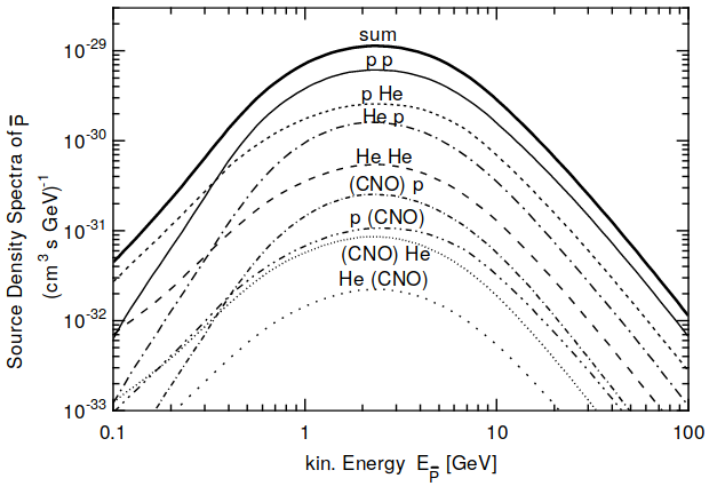

Figure 4.1 The antiproton source density for different collision systems from [84].

calculated antiproton source functions for both cases and expressed their obtained ratio of the two fluxes as a function of the antiproton kinetic energy:

$$\frac{Q_{\text{all}}}{Q_{p+p}} = \frac{0.12}{\left(\frac{E_{\text{kin},\bar{p}}}{1000}\right)^{1.67}} + 1.78 \tag{4.37}$$

The resulting fluxes from [84] can be seen in the Figure 4.1. This scaling is applied in GALPROP Monte Carlo simulation. The main problem is that the compared antiproton source function depends not only on the cross sections but on the interstellar gas density model and the local interstellar flux of primary particles. The local interstellar fluxes used by Simon et al are from very old measurements with huge uncertainties and as the fluxes were measured inside the heliosphere, the force field approximation was used to demodulate the top of the atmosphere fluxes to get local interstellar fluxes. This scaling should be used only under the assumption that the same ISM densities and LIS as in [84] are used which is never the case. Thus using this scaling will always introduce huge uncertainties.

4.2.2 Winkler parametrization

If the target and projectile fragmentation can be assumed to be independent, the inclusive particle production cross section can be factorized in target and projectile components. Then the total antiproton multiplicity can be expressed as [87]:

$$\left(\frac{dn}{dx_F}\right) = \left(\frac{dn}{dx_F}\right)^{\text{pro}} + \left(\frac{dn}{dx_F}\right)^{\text{tar}} \tag{4.38}$$

In a collision the produced particles populate both the forward and backward hemispheres in the center of mass frame. The forward hemisphere is dominated by the projectile fragmentation and vice versa - the backward hemisphere is dominated by the target fragmentation. In the NA49 collaboration analysis of $p + C$ collisions it was observed that this assumption holds true at forward and backward rapidities but at the midrapidity the contributions from

projectile and target star overlapping [83]. NA49 published an overlap functions for the target and the projectile which show what fraction of produced antiprotons come from projectile fragmentation and which part from the target fragmentation in $p+p$ collisions. It is given in Table 14 in [83]. The target contribution to the total inclusive antiproton multiplicity:

$$\left(\frac{d\,n^0_{\bar{p}}}{d\,x_f}\right)^{\text{tar}}_{hp} = F_{\text{tar}}(x_F)\left(\frac{d\,n^0_{\bar{p}}}{d\,x_f}\right)_{pp}, \tag{4.39}$$

where F_{tar} is the fraction of target contribution to the total multiplicity. The same expression holds for the projectile contribution, using the projectile overlap function: $F_{\text{pro}} = 1 - F_{\text{tar}}$. So in a collision of projectile h and proton target, the target fragmentation contribution to the total antiproton multiplicity is proportional to the multiplicity of the antiprotons produced in $p+p$ collision. This relation can be applied to express the antiproton multiplicity in heavier nuclei collisions. For example, a collision of proton and carbon can be seen as many $p+p$, $n+n$ and $p+n$ collisions. Expressed in projectile and target terms, only the antiproton multiplicities in $p+p$ and $n+n$ collisions are required as $p+n$ can be factorized. The p and n wave functions can form an SU(2) isospin doublet which means that they transform into each other under SU(2) transformations. In case of strong interaction it means that these particles behave very similarly which implies that $n_{p+p\to\bar{n}} = n_{n+n\to\bar{p}}$:

$$\left(\frac{d\,n^0_{\bar{p}}}{d\,x_f}\right)_{n+n\to\bar{p}} = \left(\frac{d\,n^0_{\bar{p}}}{d\,x_f}\right)_{p+p\to\bar{n}} = (1+\Delta_{\text{IS}})\left(\frac{d\,n^0_{\bar{p}}}{d\,x_f}\right)_{p+p\to\bar{p}} \tag{4.40}$$

At the second step we apply the isospin asymmetry factor. In a collision, one nucleon from the projectile interacts with more than one nucleon from the target nucleus. The average number of interactions in the nucleus i can be described as:

$$\langle \nu_i \rangle = A_i \frac{\sigma_{pp,inel}}{\sigma_{pi,inel}} \tag{4.41}$$

A_i is number of nucleons in nucleus i. Applying all these corrections, the antiproton multiplicities in $p+A$ and $A+A$ collisions can be expressed as [81]:

$$\left(\frac{d\,n^0_{\bar{p}}}{d\,x_f}\right)_{ij} = \left(\langle \nu_i \rangle \left(1+\frac{N_i}{A_i}\Delta_{IS}\right) F_{\text{pro}}(x_F) + \langle \nu_j \rangle \left(1+\frac{N_j}{A_j}\Delta_{IS}\right) F_{\text{tar}}(x_F)\right)\left(\frac{d\,n^0_{\bar{p}}}{d\,x_f}\right)_{pp} \tag{4.42}$$

The $\frac{N_i}{A_i}$ is neutron to nucleon ratio to scale the isospin effect depending on the number of neutrons. It has been shown in [83] that the prediction for antiproton multiplicities in a $p+C$ collision using the projectile and target model agrees with the NA49 data at 158 GeV/c proton beam momentum.

The data for antiproton production in heavier nuclei collisions is very scarce. In case of astroparticle physics, both the momentum distribution of produced antiprotons and the total antiproton cross section are important. The precise model for antiproton production is required for a wide range of projectile momentum. The existent data for $p+A$ collisions:

Table 4.2 Experimental data of antiproton production in $p + A$ collisions.

Experiment	**Collision**	$\sqrt{s_{NN}}$[**GeV**]	**Measurement**	**Published in**
NA49	$p + C$	17.238	$f(x_F, p_T)$	[83]
LHCb	$p + He$	110	$f(p, p_T)$	[88]

Chapter 5

Simulation Tools for Propagation

As it was described in chapter 3.3, the propagation of cosmic rays can be described by the transport equation. The transport equation is rather complex but it can be solved numerically. There are several tools available. One of the goals of this work is to create a propagation scheme from existing Monte Carlo simulations and constrain the parameters using experimental data described in section 3.4. The final constrained propagation scheme is showed in the Figure 5.1.

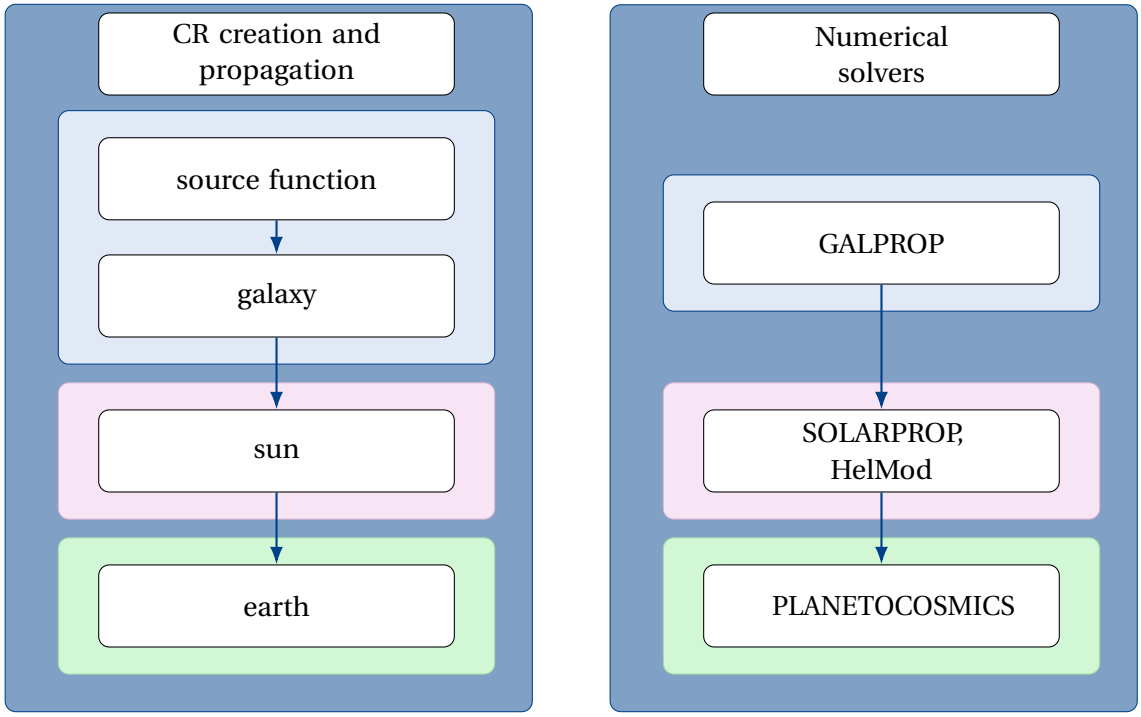

Figure 5.1 Propagation scheme.

The source term for the primary particles is the spectra produced by the acceleration in supernovae remnants while for the secondary particles the source term is described as in equation 4.36. The propagation in the galaxy, the heliosphere and the earth's environment are as explained in chapter 3.3. In the final scheme we use following software packages for the propa-

gation: GALPROP [89] (available on https://galprop.stanford.edu/); SOLARPOP [90] (available on http://www.th.physik.uni-bonn.de/nilles/people/kappl/) and HelMod [91] (available on http://www.helmod.org/) [1], PLANETOCOSMICS [92] (available on http://cosray.unibe.ch/ laurent/planetocosmics/).

5.1 GALPROP

"GALPROP is a numerical code to calculate the propagation of relativistic charged particles and the diffuse emissions produced during their propagation." [93] Many options can be chosen by the user: different interstellar gas distributions, different antiproton cross sections, source distribution in the galaxy and so on. In this chapter we will introduce our setup of GALPROP and how some of the propagation parameters influence the final local interstellar flux.

5.1.1 The galaxy setup and the main parameters

The GALPROP parameters can be set in a so called *galdef* file. The propagation parameters in GALPROP must be tuned so, that the calculated local interstellar flux would agree with the measured fluxes. The parameter space in GALPROP is rather huge and only the Voyager and CREAM-III experiments measure local interstellar flux. To use solar modulated data to constrain the local interstellar flux, one must introduce a model for heliospheric propagation in the fitting procedure. Such study has been carried out by Boschini et al [94]. In our work we use their results for the propagation parameters, source function parameters and injection spectra from a *galdef* file we received from the authors. In this subsection we list the parameters and models we use in our GALPROP simulations.
In our GALPROP setup, the cosmic ray source we chose to use the supernovae distribution based on equation 3.11 reads as:

$$\rho(R,z) = \left(\frac{R}{R_{sun}}\right)^{\alpha} \exp\left[-\beta\left(\frac{R-R_{sun}}{R_{sun}}\right)\right] \exp\left(-\frac{|z|}{z_{scale}}\right) \tag{5.1}$$

The last exponential term describes the z coordinate dependence of the source function.

Table 5.1 Source parameters.

Variable	**Parameter**	Explanation
z_{scale} [kpc]	source_parameters_0 = 0.2	
α	source_parameters_1 = 1.5	
β	source_parameters_2 = 3.5	
r_{max} [kpc]	source_parameters_3 = 20.0	If $R > r_{max}$, then $\rho(R,z) = 0$
r_{const} [kpc]	source_parameters_4 = 20.0	If $R > r_{const}$, then use r_{const} instead of R in equation 5.1

In GALPROP this is option **source_model = 1**. The source parameters, used in our simulation, are shown in Table 5.1.

[1] For solar modulation, we considered force field approximation as well.

The injection spectra of particles in GALPROP are parametrized as a double broken power law (explained in section 3.1.3). This introduces two rigidity break parameters nuc_rigid_br0 [GeV] and nuc_rigid_br0 [GeV] (R_i), where the power index changes, and three power indexes nuc_g_0, nuc_g_1, nuc_g_2 (γ_j). The employed parameters are:

Table 5.2 Source parameters.

Species	**nuc_rigid_br0 [GeV]**	**nuc_rigid_br [GeV]**	**nuc_g_0**	**nuc_g_1**	**nuc_g_2**
Default	7.0	325.0e3	1.9	2.42	2.42
e	5.8	95	1.45	2.75	2.487
p,d	6.8	365.0	1.668	2.441	2.283
He^3,He^4	6.9	330.0	1.703	2.384	2.206
C	6.0	330.0e3	1.98	2.423	2.415
O	7.4	340.0e3	1.94	2.455	2.443

We use isotopes up to nickel. The *Default* source parameters are used for all explicitly not mentioned isotopes. The kinetic energy range for particle injection is from **Ekin_min = 1.0e0** MeV to **Ekin_max = 1.0e8** MeV. The isotropic abundances are given in Appendix A of this thesis.

For the interstellar hydrogen distributions, we use the parametrizations as described in section 3.2.2. The mathematical expressions can be found in Appendix A of [45]. The helium gas is taken as a fraction of hydrogen gas: **He_H_ratio = 0.11**

The total cross sections are used from the Barashenkov and Polanski CROSEC code and the nuclei production cross sections are used from both experimental data and simulations as described in Model chapter in [95] by Moskalenko et al. The parameter options in GALPROP: **total_cross_section = 2** and **cross_section_option = 012**.

The propagation in GALPROP is described by transport equation 3.12. It is solved using the Crank-Nicholson finite difference method. We use the 2D (**n_spatial_dimensions = 2**) option, where the galaxy and cosmic rays are radially symmetric and thus (R,z) coordinates are used. The galaxy size is described by following parameters:

Table 5.3 The Galaxy dimensions. Given in [kpc].

Parameter	**r_min**	**r_max**	**z_min**	**z_max**
Value	0	20	-4	4

The diffusion coefficient in GALPROP is parametrized as a function:

$$D_{xx} = \beta^{\eta} D_0 \left(\frac{r}{D_{br}} \right)^{D_i}, \tag{5.2}$$

where r is the rigidity of a particle, β is the relativistic speed of a particle, η is the index for β dependence, D_0 is the diffusion coefficient value for normalization, D_{br} is the rigidity break at which the index D_i changes from D_1 to D_2. The parameters used in our GALPROP simulation:

Table 5.4 Propagation parameters.

Parameter	**D0_xx**	**D_rigid_br**	**D_g_1**	**D_g_2**	**eta**
Value	4.3e28	4.5e3	0.395	0.404	0.91

The diffusive reacceleration in our simulations is turned on (**diff_reacc = 1**). The diffusive reacceleration coefficient D_{pp} in GALPROP is expressed as:

$$D_{pp} = f(D_1)p^2 \frac{\left(V_{alf} \times 10^5\right)^2}{D_{xx}}, \tag{5.3}$$

where $f(D_1) = \frac{4}{3D_1(4-D_1)(4-D_1^2)}$, p is particle momentum and V_{alf} is the speed of magnetohydrodynamic Alfven wave. The V_{alf} is calculated in GALPROP by scaling some chosen v_{Alfven} coefficient to the magnetic field and the interstellar gas density at coordinate of interest. We use magnetic field model **B_field_model = 060100020**. In our simulation: **v_Alfven = 28.5**.

The convection in our simulation is turned on as well (**convection = 1**). The convection velocity **V** is a linear function in z with initial value V_0 and constant increase equal to $\frac{d\mathbf{V}}{dz}$. In our simulation: **v0_conv = 12.4** and **dvdz_conv = 9.8**.
The solution of the transport equation requires time limits and the Crank-Nicholson method requires the time step size. In our simulation: **start_timestep = 0.1e9** , **end_timestep = 1.0e2**, **timestep_factor = 0.75** and **timestep_repeat = 30** (number of repeats per time step).

Normalization

The final simulated local interstellar fluxes must be normalized. The proton flux is normalized at kinetic energy **proton_norm_Ekin = 1.0e+5** MeV to be **proton_norm_flux = 4.474e-9** $\mathrm{cm}^{-2}\ \mathrm{sr}^{-1}\ \mathrm{s}^{-1}\ \mathrm{MeV}^{-1}$. All other isotopes are normalized to proton flux accordingly to their abundances.

5.1.2 The local interstellar flux dependence on propagation parameters

The transport equation is a function in time, momentum, radial distance and the z position. Which means that changes in propagation parameters cannot be converted straight forward to changes in the local interstellar flux. To understand how a change in one parameter would change the local interstellar flux, one must solve the transport equation numerically. In this subsection we discuss how different parameters changes the final local interstellar flux.
Some of the parameters have very small influence on the final local interstellar flux. For example, the convection turned off or on with the convection velocity parameters as described in previous subsection, changes the flux only up to 5% at energies lower than 10 GeV. Diffusive reacceleration being turned on results in the up to 4% decrease of the flux at energies lower than 10 GeV.
The local interstellar flux is most sensitive to the changes in the parameters of injection spectra (**nuc_rigid_br*i*** and **nuc_g_*i***), the spectral index of diffusion coefficient (**D_g _1**), the diffusion normalization coefficient (**D0_xx**) and the half-width (**z_max**=-**z_min**). In Figure 5.2 we show how the primary proton local interstellar flux depends on these parameters. The shown local interstellar flux is calculated at 8.5 kpc distance from the galaxy center - the location of solar

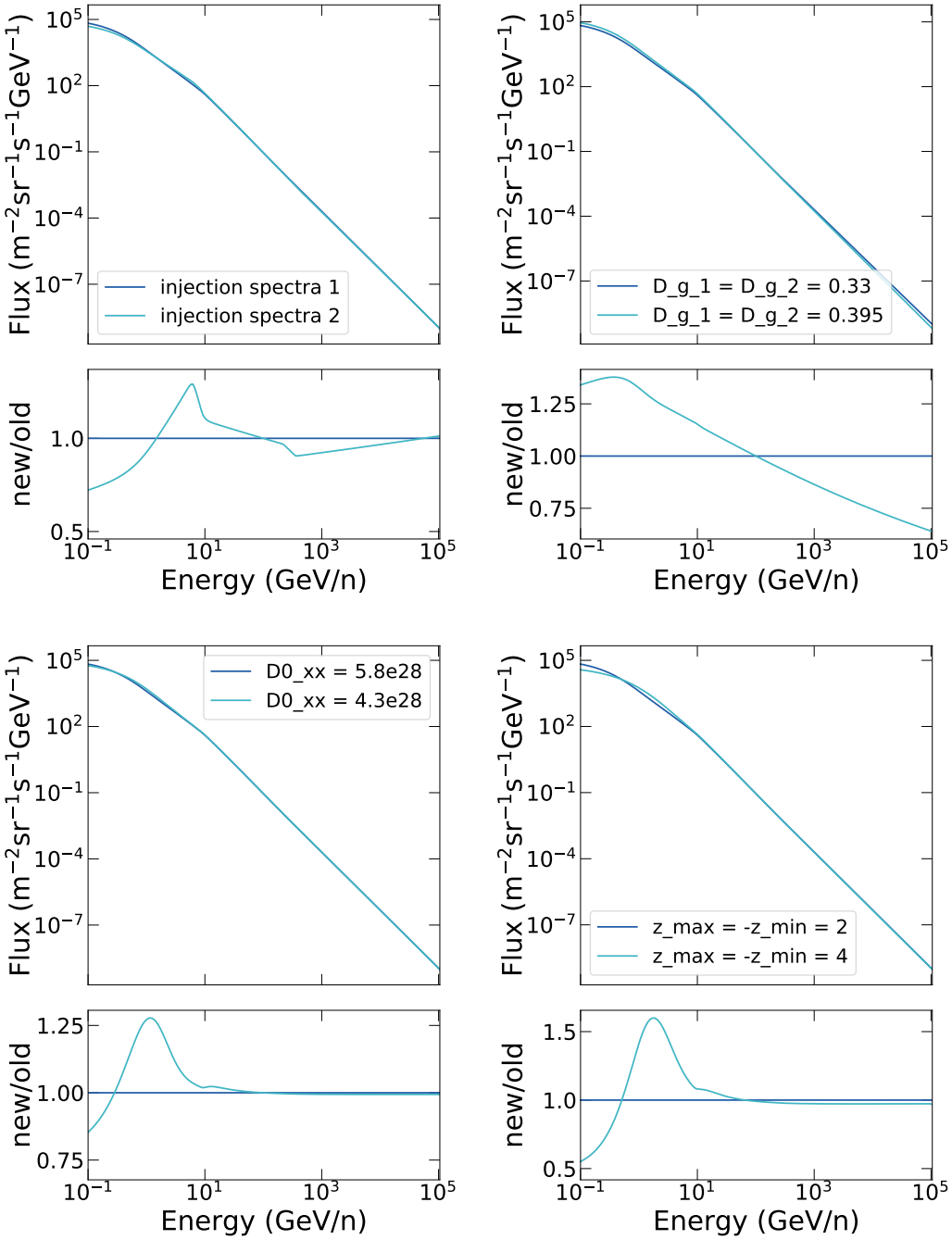

Figure 5.2 Proton local interstellar flux dependence on different parameters. In case of the injection spectra, the parameter set 1 is **nuc_rigid_br0 = 10, nuc_rigid_br = 220, nuc_g_0 = 1.9, nuc_g_1 = 2.4, nuc_g_2 = 2.3** and the parameters set 2 is **nuc_rigid_br0 = 7, nuc_rigid_br = 360, nuc_g_0 = 1.69, nuc_g_1 = 2.44, nuc_g_2 = 2.33**

system. In every plot for different parameter, the upper panel shows the fluxes computed with two different parameter values and the lower panel shows the ratio of the two fluxes.
The injection spectra parameters control the initial proton momentum spectra which is created at supernova explosions. Two different parameter sets are compared in Figure 5.2.
The diffusion normalization coefficient changes the magnitude of diffusion coefficient. As we can see in Figure 5.2, at low energies lower diffusion results in decreased flux, while the flux between 300 MeV and 7 GeV increases.
The spectral index of diffusion coefficient changes the momentum dependence of the diffusion coefficient. As shown in equation 5.2, the diffusion coefficient $D_{xx} \propto \left(\frac{r}{D_{br}}\right)^{D_i}$ and thus increasing the spectral index at rigidities $r < D_{br}$ results in lower diffusion coefficients at these rigidities and at rigidities $r > D_{br}$ - in higher diffusion coefficient. The effect of such change on the proton local interstellar flux can be seen in D_g_1 =D_g_2 plot.
The half-width of the galaxy changes the upper and lower limits of the galaxy halo height. This changes the distribution of the cosmic ray sources and thus the initial conditions of transport equation, as particles can be created at different distance from galactic disk. In Figure 5.2, it shown how the proton local interstellar flux changes if the half-width is doubled.

5.2 Solar Modulation Simulation

The local interstellar flux is computed at the position of solar system. Then the cosmic ray particles must be propagated through the heliosphere. As introduced in section 3.3.2, it can be done by solving the transport equation 3.14 either numerically or with the force field approximation. The two available numerical solvers are HelMod and SOLARPROP. In this section we introduce all three option and the main differences between them.

5.2.1 Force Field Approximation

The force field approximation was already introduced in section 3.3.2 and is shown in equation 3.15. The only free parameter - the solar modulation potential - must be fitted to the data. The solar modulation potential can be calculated using the neutron monitoring data and it has been done by Usoskin[96] but it is dependent on the local interstellar flux used in the calculations. The particle propagation in the heliosphere depends on the qA sign, where q is the particle charge and A is the magnetic field polarity. The force field approximation is charge-sign and magnetic field polarity independent.

5.2.2 HelMod

The latest HelMod version 4.0 includes both the charge-sign and the magnetic field polarity dependence. HelMod solves equation 3.14 for two different regimes: the outer and inner heliosphere. As the Voyager data showed, these regions can be explained only by different propagation parameters. The precise description of the HelMod model can be found in [91]. The solar modulation is calculated using the sunspot number data. The model has three parameters which can be tuned so that the top of the atmosphere flux would agree with the data: ρ_i, g_{low} and k_{hs}. ρ_i is the ratio of the diffusion coefficient component perpendicular to the magnetic field and the diffusion coefficient component parallel to the magnetic field; g_{low} is the upper limit of g parameter which is inverse proportional to the strength of the

solar modulation, hence it is equal to 0 at high solar activity and it takes the maximal value g_{low} at low solar activity [97]. k_{hs} is the scalar diffusion coefficient used for propagation in the outer heliosphere. The authors of HelMod used an iterative procedure incorporating the GALPROP simulations to find the best fit values for these parameters and obtained: $\rho_i = 0.065$, $g_{low} = 0.5$ and $k_{hs} = 0.00003$ [91].
The only drawback of the current HelMod implementation is that heavier than antiproton nuclei are not included in the framework.

5.2.3 SOLARPROP

The transport equation 3.14 can be rewritten as a set of stochastic differential equations (SDEs). SOLARPROP solves such SDEs using the backwards approach - the pseudo particles are created at the earth level and simulated backwards until they reach the heliopause. As it can be seen from the transport equation 3.14, the diffusion tensor, drift velocity and magnetic field models are necessary to describe the propagation. Several different models are available in SOLARPROP. We chose to use the **standard2D** model [98]. The model is dependent on the tilt angle of the heliospheric current sheet[2] and the solar activity. The tilt angle is the angle between the solar magnetic field dipole axis and the solar rotation axis. SOLARPROP uses the available databases for both tilt angle and solar activity. In the official version, the tilt angle data available on http://wso.stanford.edu/Tilts.html [99] (WSO database) is used until 2015 March. For the solar activity, SOLARPROP uses the force field potential ($\phi_{Usoskin}$) calculated by Usoskin et al in 2011 [96] which is based on neutron monitoring data. The solar activity dependence of the diffusion tensor is parametrized using a normalization κ_0 which is a function of $\phi_{Usoskin}$ [67]:

$$\kappa_0 = \tilde{\kappa_0} \begin{cases} \frac{137}{\phi_{Usoskin}} - 0.061, & \text{if qA<0} \\ \frac{7}{100}\frac{137}{\phi_{Usoskin}} - 0.061, & \text{if qA>0} \end{cases} \tag{5.4}$$

Where q and A are the particle charge and the magnetic field polarity, respectively. The $\tilde{\kappa_0}$ is the total normalization constant of κ_0. It is dependent on the local interstellar flux used as an input and has to be chosen by the user. In our propagation scheme we use the local interstellar fluxes simulated by GALPROP, scan several $\tilde{\kappa_0}$ values and compare the resulting top of the atmosphere fluxes to the AMS-02 and BESS-Polar data.
As mentioned before, in the official SOLARPROP version, the available tilt angle data is until 2015 March. We updated the tilt angle datatable by using the last available version from WSO database which includes data until 2019 August. We updated the Usoskin potential datatable to the newest version as well [100].

5.2.4 Comparison

In this subsection we compare the three introduced solutions for solar modulation.
In case of the force field approximation, we need a solar modulation potential. We use the modulation potential values published by Usoskin et al in 2017 [65]. In case of HelMod, no

[2] As mentioned before, the solar polarity reverses every 22 years. The surface, where the solar magnetic field changes polarity from north to south, is called the heliospheric current sheet.

additional fit parameters are required. In case of SOLARPROP, we employ the $\tilde{\kappa_0}$ value that allows to reproduce the particle flux on the top of the atmosphere predicted using the force field approach at cosmic ray energies higher than 700 MeV for the qA>0 case. For this we scan several $\tilde{\kappa_0}$ values and choose best fit value. This is done to simplify the comparison of the polarity and charge sign dependence of the fluxes.
The polarity dependence can be analysed only in the SOLARPROP model because it has an option to manually choose the polarity, tilt angle and Usoskin potential value. In Table 5.5, we summarize the parameter values chosen for our comparison among the different solar propagation models.

Table 5.5 Parameters for polarity testing.

Tilt angle	$\phi_{Usoskin}$**[MV]**	**Polarity**	$\tilde{\kappa_0}$
45°	600	+1	2.5
45°	600	-1	2.5

In Figure 5.3, we show the top of the atmosphere fluxes calculated using SOLARPROP and the force-field approximation.

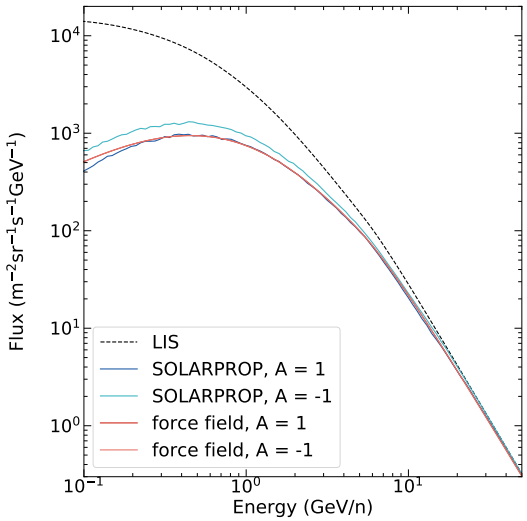

Figure 5.3 Polarity dependence.

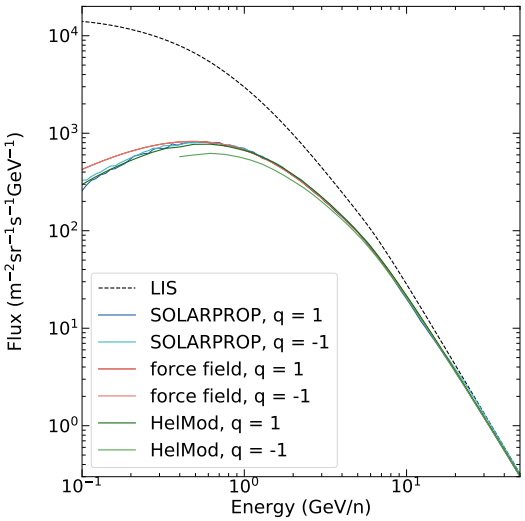

Figure 5.4 Charge-sign dependence.

The dashed black line is the local interstellar flux. The same local interstellar flux is used for all simulations shown in Figures 5.3 and 5.4 and it is computed for protons using GALPROP with parameters described in section 5.1. The force field approximation is insensitive to the polarity, thus in the plot the fluxes lie on top of each other. In case of SOLARPROP, we see that the polarity dependence is important at energies lower than 300 MeV. If $qA < 0$, cosmic ray flux is modulated less than in case of $qA > 0$.
To compare the charge sign dependence, we use the same local interstellar flux for all models and simulate the top of the atmosphere flux twice - once with particles of charge $q = 1$ and once with particles of $q = -1$. To have the same polarity sign, we choose one date for all simulations - 2015 March. The solar magnetic field was of positive polarity during this period (based on WSO data available at http://wso.stanford.edu/Polar.html). In Table 5.6 we show

the parameters used in the simulations.

Table 5.6 Parameters employed for the charge-sign testing.

Date	$\phi_{Usoskin}$**[MV]**	**Charge**	$\tilde{\kappa_0}$
2015-05	654	+1	1.7
2015-05	654	-1	1.7

In Figure 5.4, the three models are shown. In case of force field approximation, the fluxes for $q = 1$ and $q = -1$ are the same and thus in the plot they lie on each other. The force field approximation agrees with HelMod and SOLARPROP results at energies higher than 500 MeV. At lower energies the force field modulation becomes weaker than predicted by numerical solvers. In case of HelMod we see, that the charge-sign dependent modulation starts already at around 5 GeV and the difference between different charge particles is huge compared to the SOLARPROP prediction. The negative charge test particle flux, produced in HelMod, has the lower energy limit at 400 MeV (the publicly available model does not calculate lower energy modulations except if the chosen dates are for specific past experiment).
From these results we conclude, that the force field approximation is not sufficient in our analysis. Both the HelMod and SOLARPROP models have the charge-sign and the polarity dependence. The charge-sign dependence in SOLARPROP at energies of interest is extremely small while in HelMod the flux is modulated a lot stronger in case of $qA < 0$. The opposite effect was observed in case of polarity changes in SOLARPROP, where the modulation is weaker in case of $qA < 0$. In the current literature, most of the studies suggest results in agreement with the HelMod prediction - for the flux to be modulated more intensively in case of $qA < 0$ [101]. It has been shown in some studies that the flux ratio for $qA > 0/\ qA < 0$ is energy dependent and in fact can be lower than 1 [102]. It has been shown as well, that the ratio of $qA > 0/\ qA < 0$ strongly depends on the tilt angle and the strength of the magnetic field [103].
In our work we use both models.

5.3 PLANETOCOSMICS

The last propagation part takes care of the earth's atmosphere and the magnetic field. PLANETOCOSMICS is a simulation tool based on Geant4. User can define specific location where the flux should be measured by creating a detector at this location. In PLANETOCOSMICS actual particles are simulated in the same fashion as in a Monte Carlo code. Every particle reaching the simulated detector has a direction and thus one knows from which side the particle enters the detector. To compare the experimental data to the PLANETOCOSMICS results, one must simulate similar conditions - the location of the detector, the acceptance angle of the detector and so on. In Geant4 one must choose a physics list. We use the FTFP_BERT list which is a string model based on FRITIOF description of string excitation and fragmentation. It uses the Geant4 Bertini cascade for primary protons, neutrons, pions and kaons below 10GeV. In PLANETOCOSMICS simulations we use the atmosphere model NRLMSISE00 and the internal magnetic field model IGRF. The starting position of the particles is a sphere of 70000 km radius. For the particles to be distributed uniformly on a sphere, the particle source function must be weighted by $\frac{1}{2}\cos(y)$, where y is the latitude. The physical effects of propagation in earth environment on the cosmic ray flux are presented in the next section together with the

simulation results.

5.4 Propagation results

We use the experiments described in the Cosmic ray measurements subsection to constrain our propagation parameters for the full propagation scheme.
First we simulate the local interstellar flux of protons and helium using GALPROP and compare to Voyager and CREAM-III data. We use HelMod and SOLARPROP for the solar propagation and compare our results to the AMS-02 and BESS-Polar data. In the final step, we simulate the proton flux for BESS-2001 experiment using Planetocosmics and discuss the effects of geomagnetic field and the atmosphere.

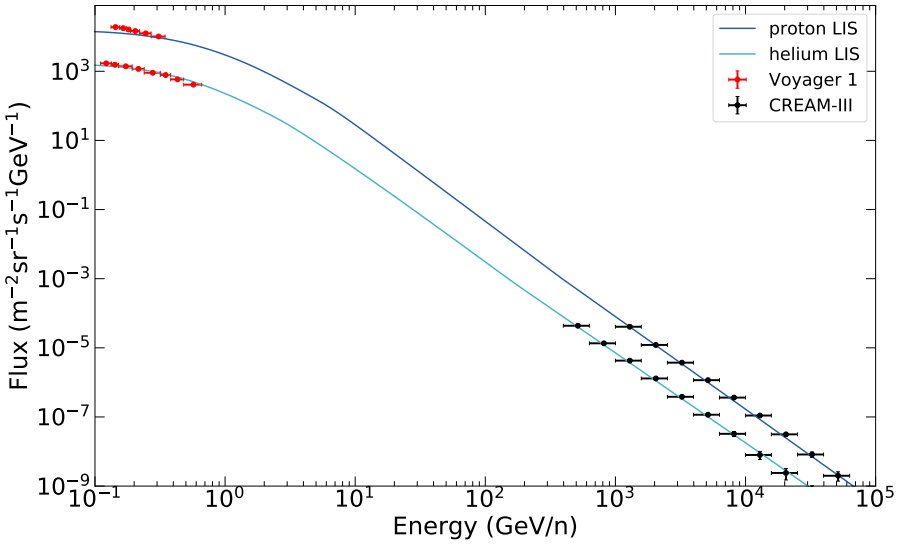

Figure 5.5 Local interstellar flux of proton and helium produced using GALPROP.

In Figure 5.5, the proton and helium local interstellar fluxes are shown. They are obtained using GALPROP v56 and the parameters, shown in section 5.1. Both local interstellar fluxes are in a good agreement with the high energy CREAM-III data and low energy Voyager I data. The proton flux at very low energies is slightly lower than the data. For the antiproton production, the proton kinetic energy threshold is $6m_p = 5.628$ GeV. Thus the small discrepancy between the lowest energy Voyager I bins and the produced local interstellar flux does not influence the antiproton spectra.
Voyager I measured boron and carbon local interstellar fluxes at energies per nucleon between 5 MeV and 111.5 MeV. The estimated B/C in this energy region fluctuates between values 0.127 and 0.162 [104]. In our simulation it is increasing from 0.08 to 0.165 in this energy region.
As we use the same parametrization of GALPROP as Boschini et al [94] but slightly different version of the code, we compare our obtained local interstellar fluxes with the published ones. Boschini et al used GALPROP v55 which is publicly not available but a short description of it can be found in [105]. We use the publicly available GALPROP v56 code. In Figure 5.6 we compare our results with the Boschini et al. The vertical lines in the ratio plots are at the energies, where

the rigidity breaks of the injection spectra are. The red dot shows the maximum of the first peak while the blue dot shows the minimum of the second peak in the ratios. In our model the transitions between different spectral indexes are less smooth. We see, that at the energies, where rigidity breaks are, our results are different than Boschini et al. In case of protons, we observe a 10% increase in the flux at 6 GeV energy compared to Boschini et al; in case of helium - 24% increase at 2.8 GeV.

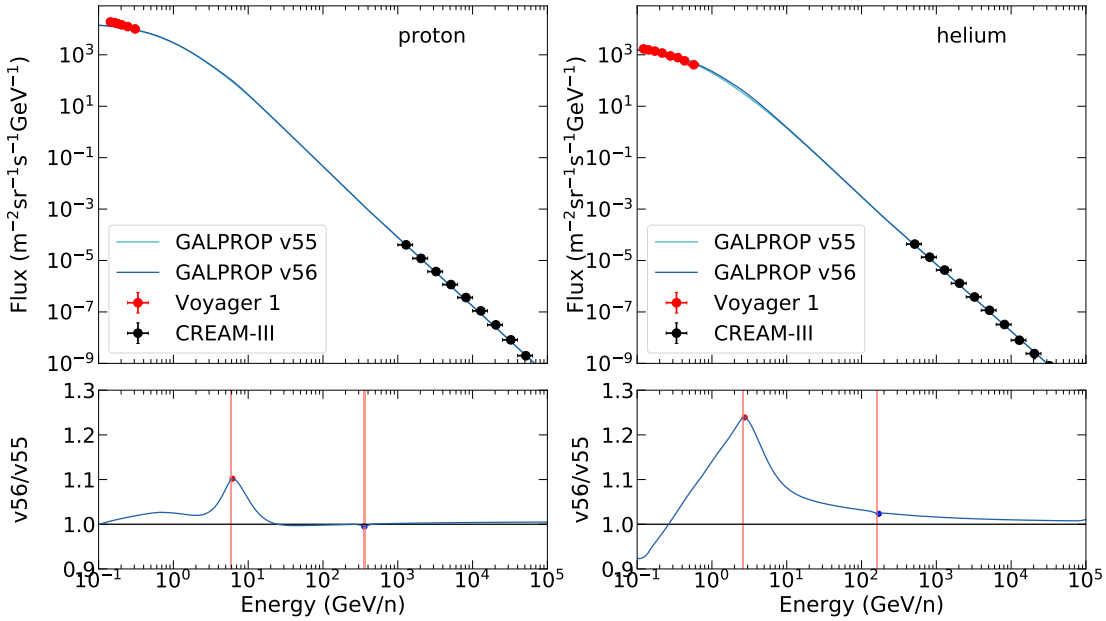

Figure 5.6 Comparison of the local interstellar fluxes obtained using public GALPROP v56 and the local interstellar fluxes published by Boschini et al using GALPROP v55. The vertical lines in the ratio plots are at locations where the rigidity breaks of the injection spectrum are. In the ratio plots, the red dot shows the maximum of the first peak and the blue dot shows the minimum of the second peak.

We use HelMod and SOLARPROP to propagate our obtained proton local interstellar flux in the heliosphere and compare it to the AMS-02, BESS-Polar I and BESS-Polar II experimental data. The diffusion tensor in the SOLARPROP model, shown in equation 5.2, requires the user-defined normalization only because its normalization depends on the initial local interstellar flux which is used. By default $\tilde{\kappa_0}$ is equal to 1 as the implemented κ_0 expression was tuned using the local interstellar flux chosen by SOLARPROP developers. As we use our obtained local interstellar flux shown in Figure 5.5, we need define the $\tilde{\kappa_0}$ value ourselves. $\tilde{\kappa_0}$ is constant in time and thus has to be chosen only once by comparing SOLARPROP results to experimental data. Our proton local interstellar flux has a 10% peak at 6 GeV energy compared to Boschini et al results. This feature will be propagated to the top of the atmosphere flux as well. Thus $\tilde{\kappa_0}$ can not be tuned to reproduce the experimental data as it would result in the overfiting of the solar modulation. On the other side, the HelMod model is tuned using the Boschini et al local interstellar flux which is obtained using the same parametrization of the galaxy and propagation parameters and we don't need to renormalize it. Thus we scanned several values of the $\tilde{\kappa_0}$ parameter and chose the ones for which SOLARPROP reproduces the structure of proton flux obtained using HelMod for the BESS-Polar I data the best.

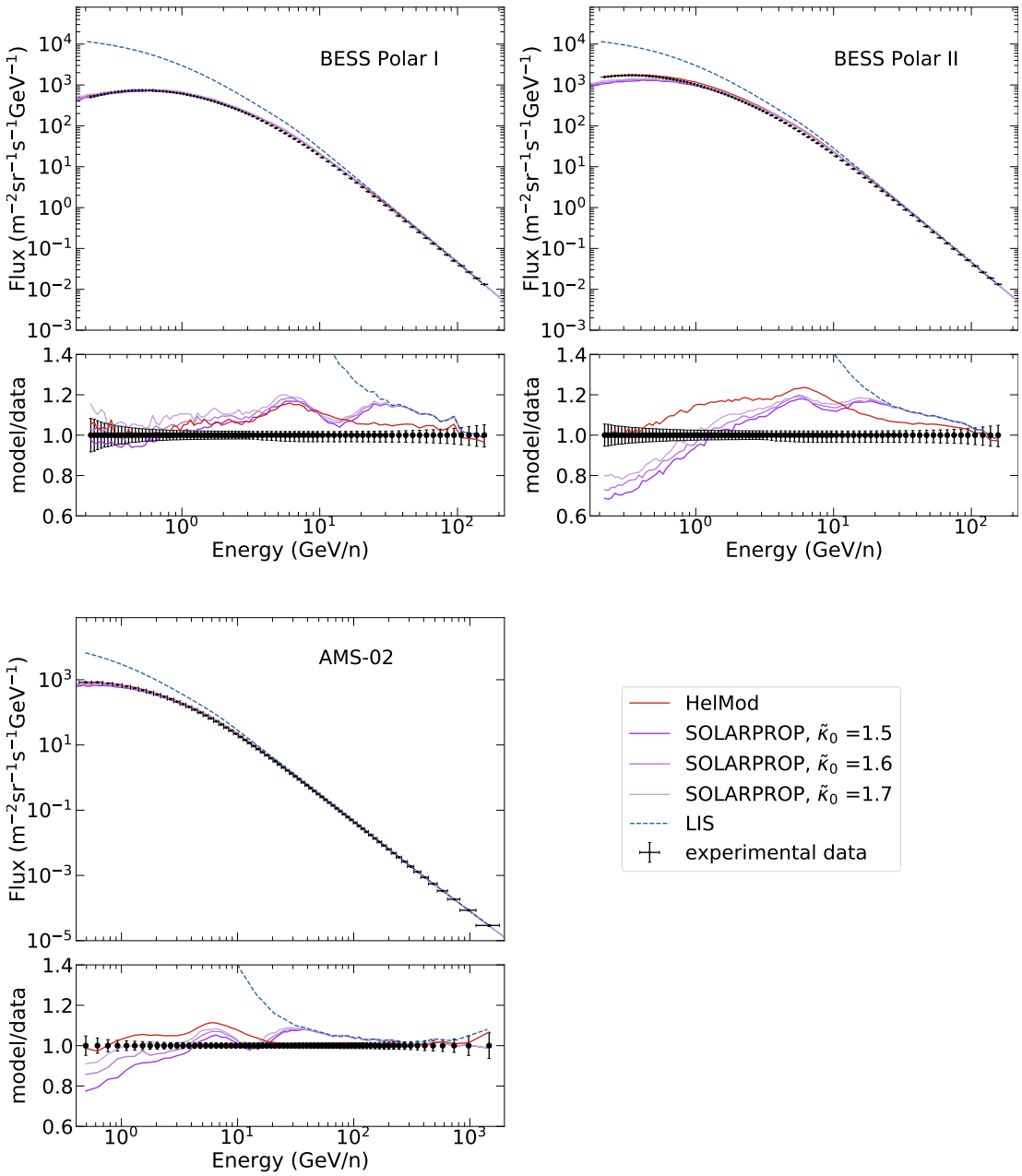

Figure 5.7 The comparison of HelMod and SOLARPROP solar modulation models. The top of the atmosphere fluxes are simulated for AMS-02, BESS-Polar I and BESS-Polar II experiments.

The resulting top of the atmosphere fluxes for AMS-02, BESS-Polar I and BESS-Polar II are shown in Figure 5.7. At around 6 GeV energy we see, that the simulated fluxes for all experiments are too high using both solar propagation models and we can observe a peak structure in the model over data ratio. As the peak is in both solar modulation models, it is safe to assume that it is a problem of the local interstellar flux. As shown before, our local interstellar flux has an increase in flux at the same energy range compared to the Boschini et al. At the energies $\sqrt{s} > 20$ GeV, the HelMod result is in perfect agreement with the AMS-02 data. Another important observation is, that the two models - HelMod and Solarprop - behave very differently in

general. In case of HelMod, the solar modulation is already visible at around 100 GeV - 200 GeV while, in case of SOLARPROP, the solar modulation starts at around 30 GeV. If we compare the low energy results for BESS Polar I and AMS-02 experiments, we see that the SOLARPROP model is not constant. To fit both datasets the best would require using different $\tilde{\kappa_0}$ which is physically incorrect as it is only the normalization factor for neutron monitoring data and the time dependence has to come purely from the neutron monitoring data. Thus we choose to use HelMod model for solar propagation in the antiproton study later on.

The last part of the cosmic ray propagation occurs in the earth's environment. The presence of the earth's magnetic field and the atmosphere complicates the interpretation of cosmic ray measurements. This is especially important in the case of low energy antiparticles. Because of this, the AMS-02 experiment was installed on the ISS, to have as little influence from earth as possible. In case of our antiproton cosmic ray studies, we use only AMS-02 data and thus the earth propagation part is not required. For the sake of cosmic ray propagation scheme completeness, we investigated the Planetosmics Monte Carlo simulations and compared our results to the BESS-2001 data.
In Planetocosmics the source of cosmic ray particles must be defined by the user as well as the detector geometry. We use the starting position for proton propagation to be at 70000 km altitude which provides a precise magnetic field simulation and an acceptable computation time. Particles are homogeneously distributed on an earth-concentric sphere of $R_{source} = 70000 + 6371.2$ km radius (6371.2 km is the radius of the earth) and propagated towards earth including interactions with the geomagnetic field and the atmosphere. The top of the atmosphere flux, defined by the user, is used for the initial particle energy distribution. We simulate our detector at the atmospheric depth equal to 26.4 g/cm^2[75] which is equivalent to the altitude of the detector $h_{det} = 25.2842$ km (the conversion between atmospheric depth and the altitude depends on the atmospheric model, thus this altitude is specific for our simulation). In Planetocosmics, the detector is a shell of radius $R_{det} = h_{det} + 6371.2$ km. We define the detector limits in geographic coordinates: latitude $31° < \alpha < 39°$ and the longnitude $-116° < \beta < -91°$ accordingly to the balloon flight location [75]. The BESS-2001 detector was made to measure vertical fluxes an thus has the opening (zenith) angle of $\cos\theta_z \geq 0.9$ which is implemented in our Planetocosmics simulation as well.
The count of particles, detected with a given detector geometry, must be converted to the isotropic flux. The normalized flux is calculated as $f = f_D \frac{N_r/t}{N_s/t}$, where f_D is the flux, measured by the detector, N_r/t and N_s/t are the rate of expected real primary particles and the rate of simulated primary particles. $\frac{N_s}{t}$ is simply the number of simulated primary particles divided by time $\frac{prim}{t}$. The expected real particle rate of an isotropic flux for a spherical shell (the starting geometry for primary particles) is calculated as:

$$\frac{N_r}{t} = 4\pi R_{source}^2 \times \pi \int_{E_{min}}^{E_{max}} f_{prim}, \tag{5.5}$$

where $4\pi R_{source}^2$ is the starting sphere area. $\pi \int_{E_{min}}^{E_{max}} f_{prim}$ is the integral of the top of the atmosphere flux used for the primary particle energy distribution. The flux measured by a detector is proportional to the detected particle count and has to be normalized to the detector

geometry:

$$f_D = \frac{N_c}{t}\frac{1}{A_{det}} = \frac{N_c}{t}\frac{1}{(\beta_{max}-\beta_{min})(\sin\alpha_{max}-\sin\alpha_{min})R_{det}^2\Omega}, \tag{5.6}$$

where N_c is the particle count, α_{max} and α_{min} are the latitudinal limits of the detector, β_{max} and β_{min} - longitudinal limits of the detector, Ω is the solid angle range (detector acceptance): $\Omega = 2\pi(1-\cos\theta_z)$. As mentioned before, the detector is simulated as a sphere, but locally it behaves as a planar detector as the radius of the sphere is large compared to the detector dimensions. The acceptance of a planar detector is dependent on the cosine of the angle between the particle incident angle and the normal to the surface. Thus in the counting procedure of the detected particles to obtain N_c, the detected particles must be weighted by $\frac{1}{\cos\theta}$ on event by event basis.
To have differential cosmic ray flux, this analysis has to be done for separate energy bins and the f flux has to be normalized to the energy bins used in the analysis. In Figure 5.8a, the resulting cosmic ray flux is shown.

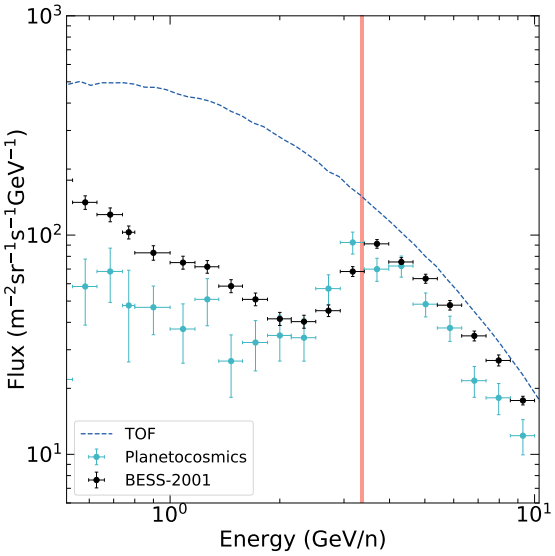

(a) The proton cosmic ray flux measured by BESS-2001 at 26.4 g/cm^2 atmospheric depth and Planetocosmics results. The red vertical line shows the geomagnetic cut-off energy.

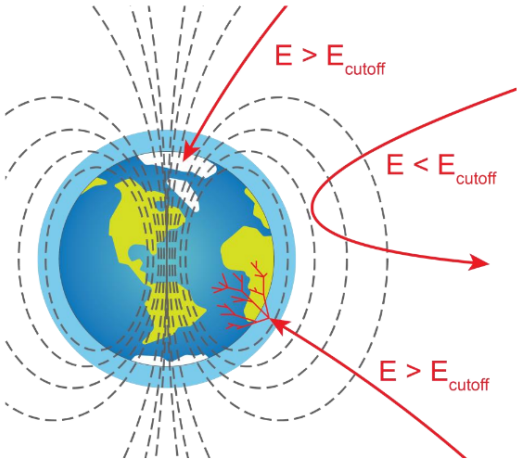

(b) The geomagnetic field and cosmic ray particle interaction scenarios.

Figure 5.8b shows three possible scenarios for a particle entering the geomagnetic field and the atmosphere. The geomagnetic field has a cut-off rigidity - particles with lower rigidity than cutoff are deflected by the geomagnetic field ($E < E_{cutoff}$). The cut-off rigidity during the BESS-2001 flight is estimated to be 4.2 GV and for protons the cutoff energy thus is 3.37 GeV [75]. It is shown as a red vertical line in Figure 5.8a. The Planetocosmics simulation is able to reproduce this behavior as seen in Figure 5.8a. If a particle has enough energy, it enters the deeper layers of the atmosphere. It can either collide with atmospheric particles or reach the detector with modulated energy. In case of a collision, new particles are produced. This effect can be best seen at the energies lower than the cutoff, as the primaries are deflected and the measured flux consists mainly of the secondaries from atmospheric interactions. Even

though we obtain the same geomagnetic field and atmospheric interaction behaviour, the Planetocosmics simulated flux is lower than measured by BESS-2001. It can be either related to too strong solar modulation or the atmosphere model used in Planetocosmics.

Chapter 6

Antiproton Production

The cosmic ray antiprotons consist of the secondary particles produced in the interstellar medium. In the scope of this thesis we investigate only the antiproton production in ordinary matter collisions. As the interstellar medium and the cosmic rays are mainly protons and helium nuclei, their collisions make up around 92% of produced antiprotons. In this chapter we investigate existing parametrizations and event generator results for antiproton production in $p+p$ and $p+He$ collisions.

6.1 Parametrizations

The official GALPROP version has two antiproton production parametrizations implemented - by Tan et al [79] described in section 4.1.1 and by Kachelriess et al [106] which is shortly introduced below and we will refer to it as Kachelriess parametrization. We implemented the Winkler parametrization [81] which was described in section 4.1.2. In this section we compare these three parametrizations with measurements collected at accelerator experiments .
The Kachelriess et al parametrization is based on modified version of QGSJET-II-04 Monte Carlo generator which the authors named QGSJET-IIm. Particle production in QGSJET is described using string fragmentation. Kachelriess et al modified the string fragmentation procedure for low energy collisions to enhance the antiproton production. The resulting invariant differential cross sections for antiproton production are already implemented in GALPROP as interpolation of values from a look-up table for p+A and He+A collisions up to iron.
In case of cosmic ray physics, both the total inclusive antiproton production cross section and the invariant differential cross section are important. The first one defines, how many antiprotons are produced and the second one provides the momentum distribution.
First we show the multiplicity comparison of the three parametrizations. At high energies we use experimental data summarized in [81] and shown in Table 6.1; at low energies - experimental data summarized in Antinucci et al paper [107]. The three parametrizations we are using are for the antiproton inclusive invariant differential cross sections and the data is given as multiplicity. To convert the differential cross section to multiplicity, the equation 4.8 has to be applied. Kachelriess et al and Tan et al does not give any expression for the total inelastic cross section thus for all three parametrizations we use Winkler parametrization of total inelastic cross section for $p+p$ collision, shown in equation 4.27. The Winkler parametrization of total

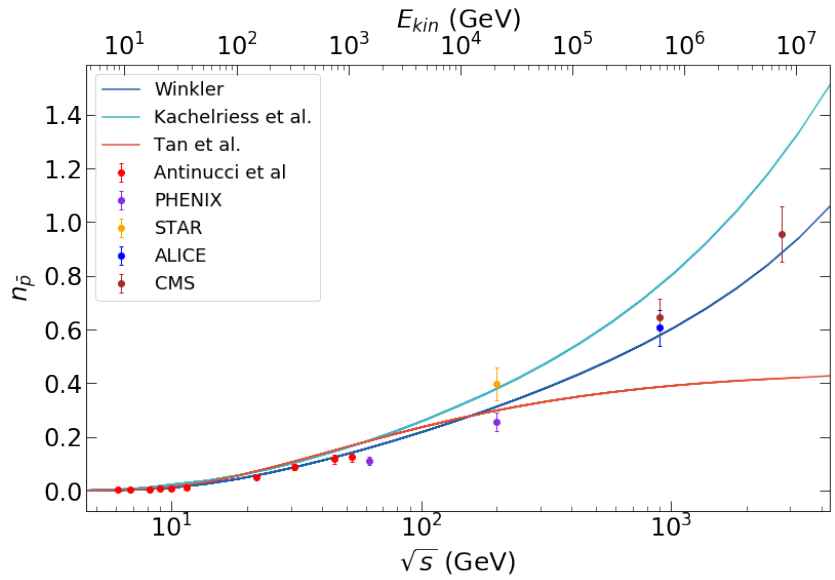

Figure 6.1 Antiproton multiplicity in $p+p$ collisions.

inelastic cross section agrees well with data [81], thus it is a good reference for multiplicity calculation. This is a good choice, because in case of cosmic ray studies we use only the inclusive differential cross section and calculating multiplicities for all parametrizations using the same inelastic cross section, lets us compare the energy dependence of the multiplicity between the parametrizations.

In Figure 6.1, we show the prompt production antiproton multiplicities. As Kachelriess implementation includes two channels - prompt production and antineutron decay channel, to obtain Figure 6.1, we assume that both channels have the same cross sections. When Feynman scaling was formulated, he assumed that the total inelastic cross section becomes constant at high energies. Later the high energy data showed that the Feynman scaling is violated as the inelastic cross section increases with the $\sqrt{s}$. As shown in [81], not only the total inelastic cross section scaling is violated, but the antiproton inclusive differential cross section scaling is violated as well. The Tan and Ng parametrization was developed in 1983 when only low energy data was available thus it predicts constant antiproton multiplicities at high energies.

In case of the Kachelriess and Winkler parametrizations, the high energy data was already available. The Kachelriess parametrization overestimates the multiplicities at high energies but is in better agreement with the STAR data point at $\sqrt{200}$ GeV. The Winkler parametrization fits both low and high energy data well. However, in the antimatter cosmic ray studies we are mostly concerned with the collisions at lower energies. In Figure 6.2 we show the lower energy region of multiplicities shown in Figure 6.1. The Tan and Ng parametrization overestimates the antiproton production at $\sqrt{s} > 10$ GeV. The Kachelriess parametrization overestimates the antiproton production at full collision energy range shown in Figure 6.2. The antiproton multiplicity is completely off at $\sqrt{s} = 10$ GeV. The Winkler parametrization fits the low energy data well.

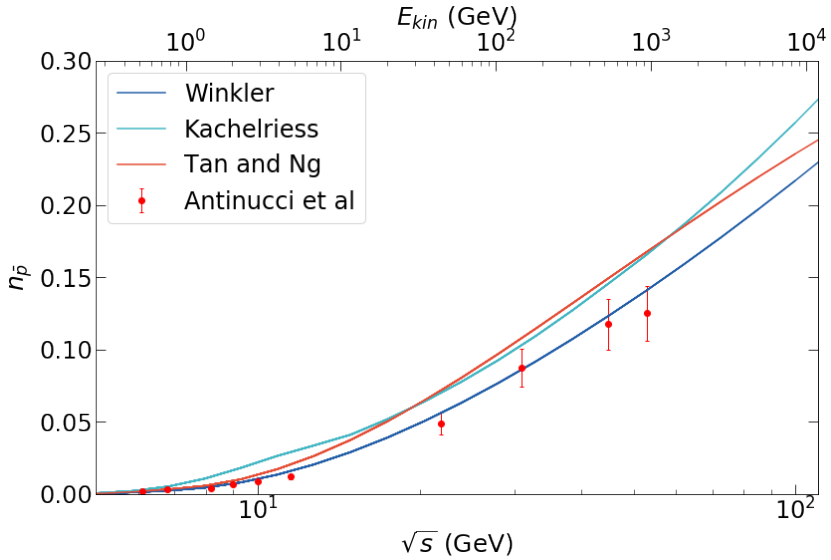

Figure 6.2 Antiproton multiplicity in $p+p$ collisions. Low energy region.

The prompt antiproton momentum for two collision energies are shown in Figure 6.3. At $\sqrt{s} = 4.54$ GeV, we again see that Kachelriess overestimates the antiproton production. The center of the momentum distribution of all three parametrizations is at around $p_{\bar{p}} = 2$ GeV/c. In case of the collision energy $\sqrt{s} = 43.33$ GeV, we see that the momentum distribution calculated using Kachelriess parametrization is shifted to lower energies compared to the other two parametrizations.

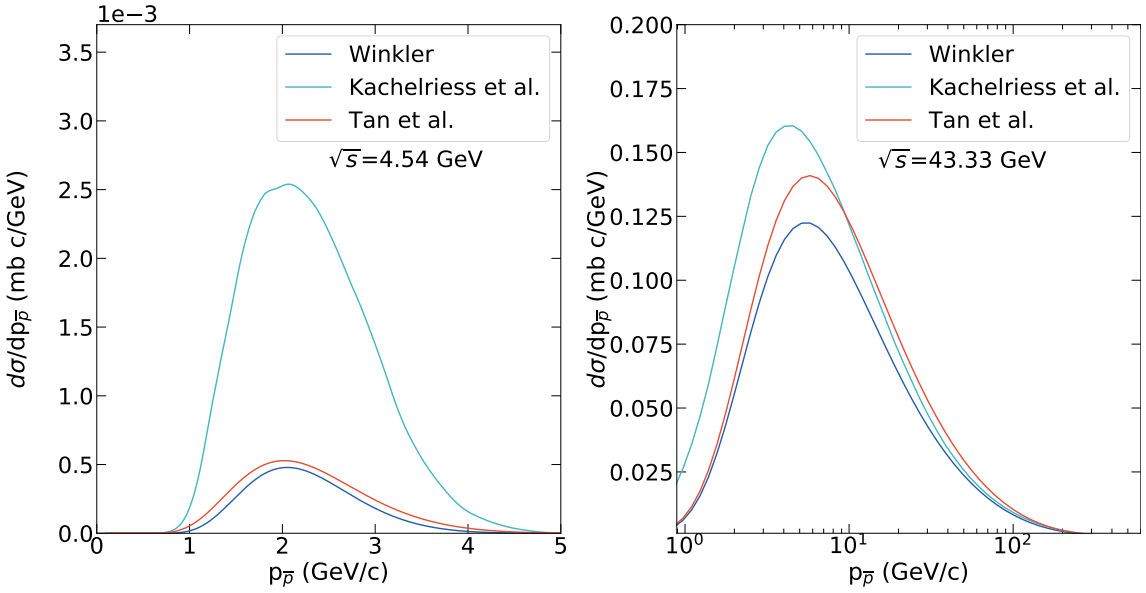

Figure 6.3 The momentum distribution of prompt produced antiprotons.

As mentioned in section 4.1, the antiprotons in cosmic rays are produced not only in prompt production, but from antineutron and antihyperon decays as well. In case of Tan and Ng parametrization, only antineutron decay channel is included under assumption that antipro-

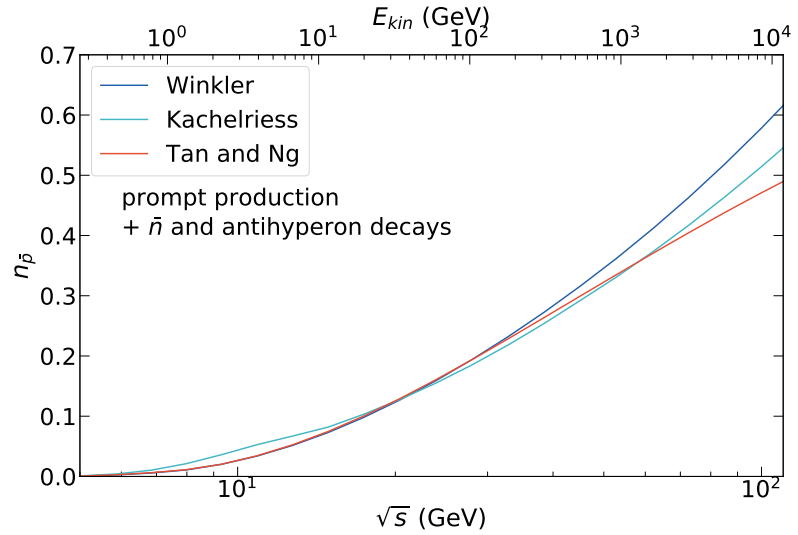

Figure 6.4 The multiplicity of antiproton production from all channels: prompt, antineutron decay, antihyperon decay.

ton production in prompt and antineutron decay channels are the same. In Kachelriess, only the antineutron decays are included, as produced in QGSJET-IIm simulations. In case of Winkler parametrization, both decay channels - antineutron and antihyperon - are included as described in section 4.1.2. In Figure 6.4, the total antiproton multiplicities are shown including all channels. The Kachelriess parametrization antiproton multiplicities are still much higher at around $\sqrt{s} = 10$ GeV energies. At higher collision energies, the Winkler parametrization show higher values than the other two parametrizations. The momentum distributions are not shown, because in all parametrizations it is assumed, that the antiprotons from antineutron and antihyperon decays have the same momentum distribution as prompt antiprotons.

Table 6.1 Experimental data for prompt antiproton multiplicities in $p+p$ collisions.

Experiment	$\sqrt{s}[GeV]$	n
PHENIX	62	0.109±0.015
PHENIX	200	0.255±.035
STAR	200	0.397±.061
ALICE	900	0.606±.067
CMS	900	0.647±.066
CMS	2760	0.956±.102

6.2 Event Generators

Cosmic ray antiprotons are created not only in $p+p$ collisions but in heavier nuclei collisions as well. The available antiproton production data in $p+He$ collisions is very scarce while for $He+He$ collisions there is no data at all. This can be solved by using event generators. Event generators are necessary for heavier antinuclei production as well. For example, the

formation of antideuterons can be described by the coalescence model which provides the probability for antiproton and antineutron to form an antideuteron depending on the relative momentum of the initial $\bar{p}$ and $\bar{n}$ pair. Thus the coalescence model must be applied event by event on the $\bar{p}$ and $\bar{n}$ pairs of known relative momentum. This can be done only with an event generator. Thus we use several event generators for $p+p$ production and compare resulting antiproton momentum distributions with NA49 data to see if the generators are reliable.
We investigate the antiproton production in the following event generators: GiBUU 2019 (The **Gi**essen **B**oltzmann–**U**ehling–**U**hlenbe transport model)[108], EPOS 3.117 (**E**nergy conserving quantum mechanical approach, based on **P**artons, parton ladders, strings, **O**ff-shell remnants, and **S**plitting of parton ladders)[109] and PYTHIA 8.24 [110].

GiBUU is a transport model for low energy MeV and GeV collisions and was written to describe the interactions of elementary projectiles with nuclear targets. In case of two-body collisions, GiBUU separates two energy regions, where different methods are used to obtain the cross sections. At low energies ($\sqrt{s} < 2.6$ GeV in case of the baryon-baryon collisions), the production cross sections are given by the Breit-Wigner resonance formula and additionally non-resonant background processes are included. For high energies, GiBUU uses PYTHIA 6.4 as an event generator. In the overlap region, GiBUU has a "transition window". A collision in this window can be simulated using either low or high energy description and the choice is probabilistic. The transport model in GiBUU is based on the BUU equation which "describes the space-time evolution of a many-particle system under the influence of mean-field potentials and collision term".

EPOS is based on the parton model. At high energies, the inclusive cross sections in general can be expressed by convoluting a parton-parton interaction cross section with two parton distribution functions. The deep inelastic scattering gives information about the parton distributions while the interaction cross sections can be calculated from perturbative QCD. This image is based on the emission of partons which are generally off-shell and can emit new partons. In EPOS it is defined as parton ladder. In hadron-hadron collisions, after the two parton interaction, the observer partons are the off-shell remnants which emit new particles. The parton ladder produce particles mainly at central rapidities; remnants - at large rapidities. The exclusive cross section calculation is implemented using the parton-based Gribov-Regge theory for multiple scattering including the total energy conservation [111]. The hadrons are created from partons using string fragmentation. At high energies and high multiplicities, the string density increases and they cannot decay independently. EPOS uses hydrodynamics to describe the evolution of the low energy high density string regions while high energy strings which can escape these regions form jets but they are still influenced by the flow.

PYTHIA is based on multiple parton-parton interactions (MPI). Many different hard processes are available. Each collision simulation includes a hard-process selection, leading-order perturbative QCD calculations, initial and final state parton radiation and beam remnants [112]. The hadronization is done by means of the Lund string fragmentation model. As mentioned in the EPOS description, at high energies collective effects are observed. Instead of using hydrodynamics, PYTHIA 8.24 uses the color reconnection mechanism to account for collectivity [110]. The total, elastic and inelastic cross sections are used from the Regge fits to data.
We use the Monash tune of PYTHIA 8.24.

We compare the invariant double differential antiproton cross section obtained from the three event generators to the NA49 data. NA49 is a detector at the CERN SPS. They measured inclusive double differential invariant antiproton cross sections in $p+p$ collisions at a beam momentum of $p = 158$ GeV/c as a function of x_F and p_T [113]. The published data cover a transverse momentum range from 0.1 GeV/c to 1.5 GeV/c and the Feynman scaling variable ranges from -0.05 to 0.4.
We use the inclusive invariant cross section as shown in 4.5:

$$f(x_F, p_T) = \frac{2E}{\pi\sqrt{s}} \frac{d^2\sigma}{dx_F dp_T^2} \tag{6.1}$$

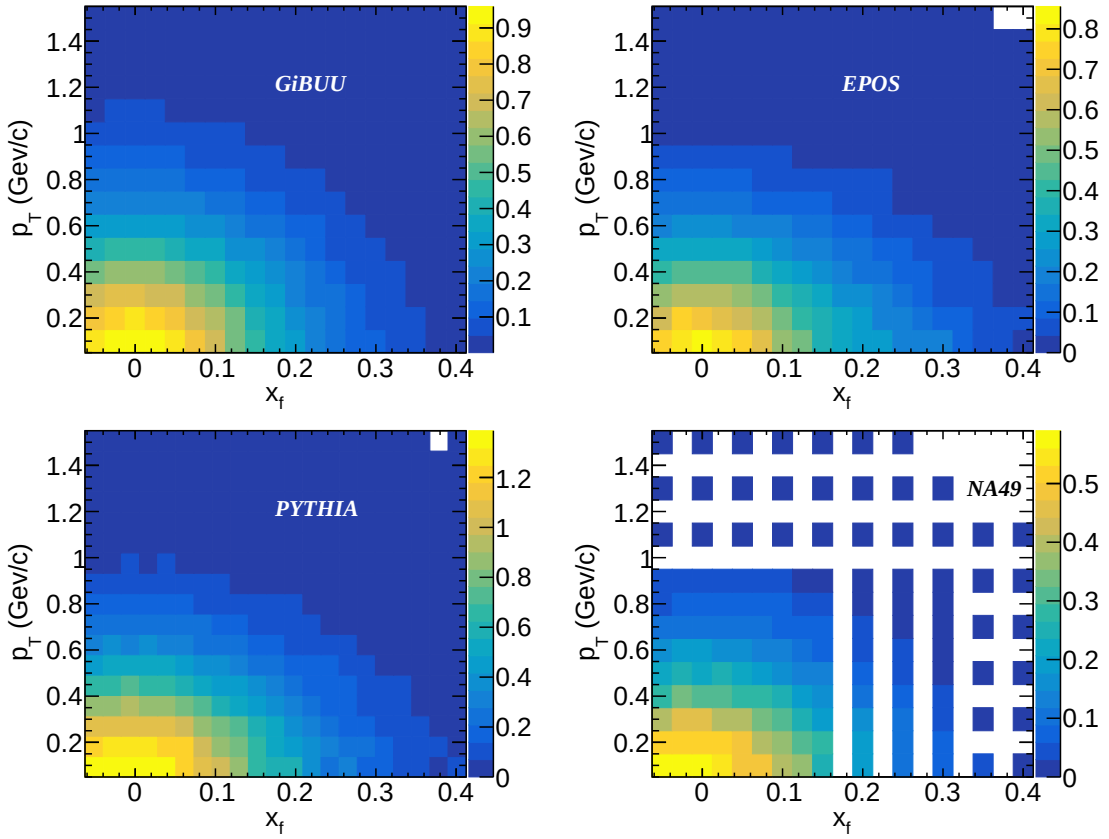

Figure 6.5 The inclusive invariant antiproton cross section $f(x_F, p_T)$ in (mb/(GeV^2/c^3)) measured in $p+p$ collisions in NA49 experiment and obtained using the three event generators: GiBUU, EPOS, PYTHIA.

In case of the generator results, the inclusive invariant cross section is evaluated bin by bin using the following expression:

$$f(x_F, p_T)_{exp} = \frac{2E}{\pi\sqrt{s}} \sigma_{inel} \frac{N_{\bar{p}}}{N_{events}} \frac{1}{\Delta p_T \Delta x_f}, \tag{6.2}$$

where $\frac{E}{p_T}$ is the antiproton energy and momentum and it is applied as a weight in the antiproton counting procedure; $\sqrt{s}$ is the collision energy. $\frac{1}{\Delta p_T \Delta x_f}$ accounts for the bin size. $\frac{N_{\bar{p}}}{N_{events}}$ is

the ratio of produced antiprotons to the total number of events. σ_{inel} is the inelastic cross section at $\sqrt{s}$ energy. We obtain the inelastic cross section for the NA49 collision energy from the generators themselves and the resulting values are shown in Table 6.2.
In Figure 6.5, we show the results from GiBUU, EPOS and PYTHIA event generators and the data published by NA49. All three generators predict higher inclusive invariant antiproton cross sections than measured by NA49. To better see the differences between the generator results and the NA49 data, we show in Figure 6.6 the ratios data versus event generator.

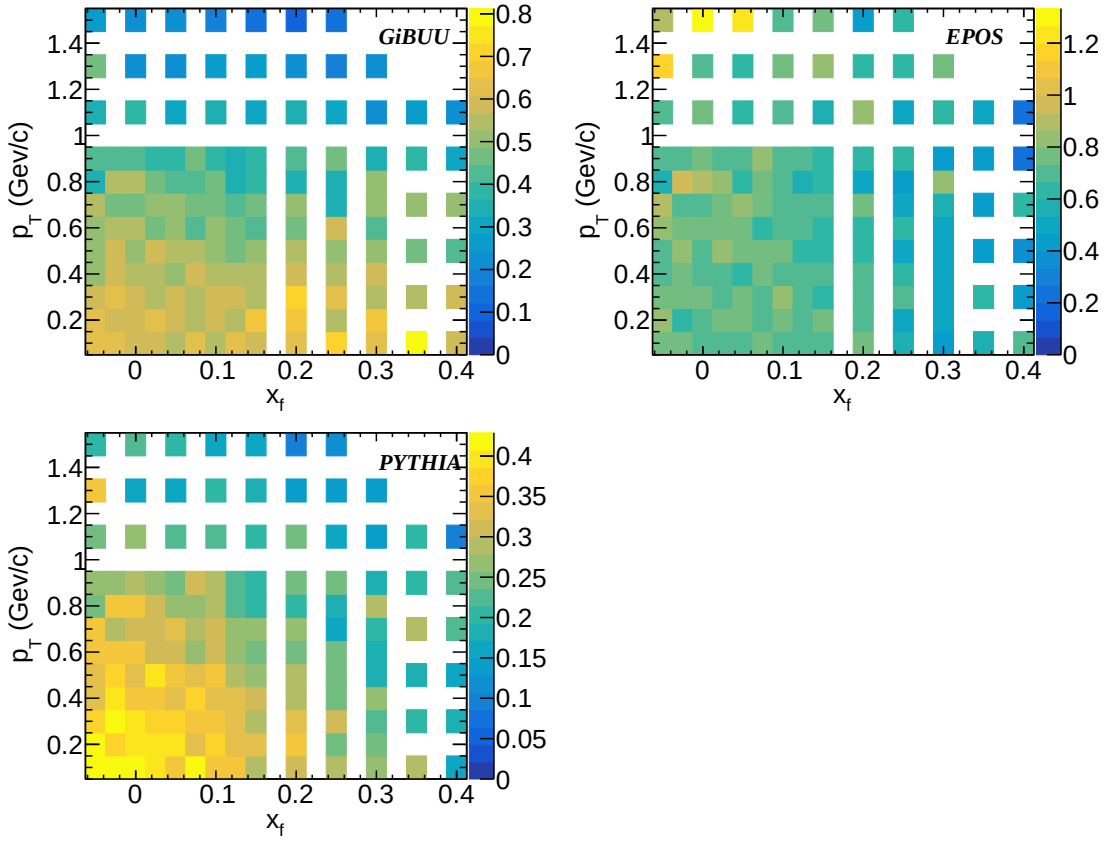

Figure 6.6 The inclusive invariant antiproton cross section $f(x_F, p_T)$ ratio data versus event generator.

Table 6.2 Inelastic cross section for $p+p$ collisions at beam momentum $p = 158$ GeV/c .

Generator	σ_{inel} **(mb)**
GiBUU	32.0
EPOS	31.69
PYTHIA	31.79

From the ratio plots we see, that $f(x_F, p_T)$ distribution produced by EPOS is the most consistent with the data. The invariant cross section dependence on x_F is better reproduced by GiBUU than PYTHIA while the p_T distribution is not consistent with the data in both event generators. In Figure 6.7, we show the inclusive invariant cross section integrated over x_F. As already seen in double differential case, PYTHIA overestimates the cross sections the most. It can be seen, that the transverse momentum dependence of the invariant cross section are similar for

PYTHIA and GiBUU until the last bin. In case of EPOS, as mentioned before, the transverse momentum distribution is rather similar to NA49 data.

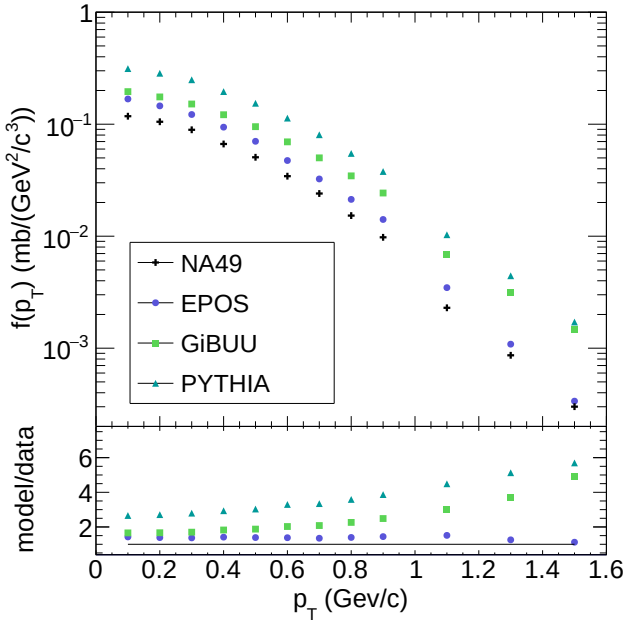

Figure 6.7 The inclusive invariant antiproton cross section $f(x_F, p_T)$ integrated over x_F.

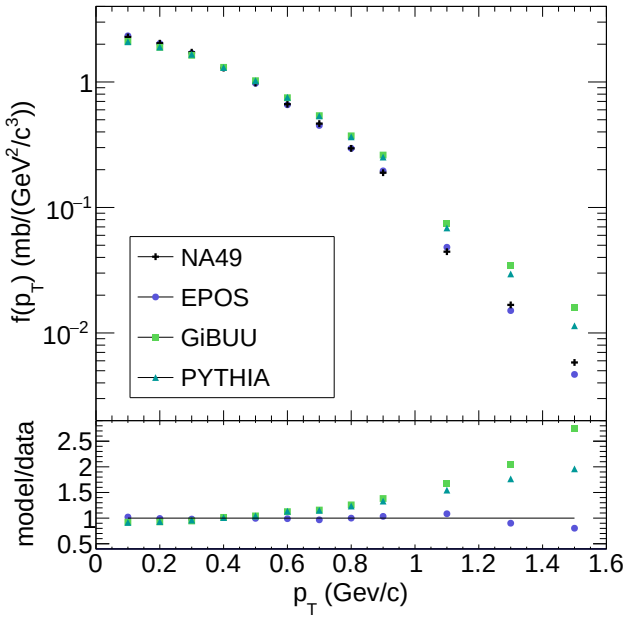

Figure 6.8 The inclusive invariant antiproton cross section $f(x_F, p_T)$ integrated over x_F. The integrals of cross sections are scaled to 1.

In Figure 6.8, we show the same results, but the invariant cross sections are scaled so that

the integral over p_T would equal to 1. Compared to NA49 data, the momentum distribution produced by EPOS is the most similar while the GiBUU is the most different.

6.3 Implementation in GALPROP

As mentioned before, we implemented the Winkler parametrization in GALPROP. It is done accordingly to the equations, described in section 4.1.2. We implemented antiproton production in $p+p$, $p+He$ and $He+He$ collisions.
In case of event generator results, we implemented a general solution. In GALPROP, the momentum grid of protons and antiprotons depends on the **Ekin_min** and **Ekin_max**. We use fixed values for these parameters thus the momentum grid is constant. We use the event generator for all proton momentum values in the grid and then calculate the invariant antiproton cross section in the bins of the central values from the antiproton grid used in GALPROP. Thus the invariant antiproton cross section implementation in GALPROP requires to run the event generator at 276 collision energies and to produce a table of size 276x276 where every value is the invariant antiproton cross section at specific $p+p$ collision energy for specific antiproton momentum.

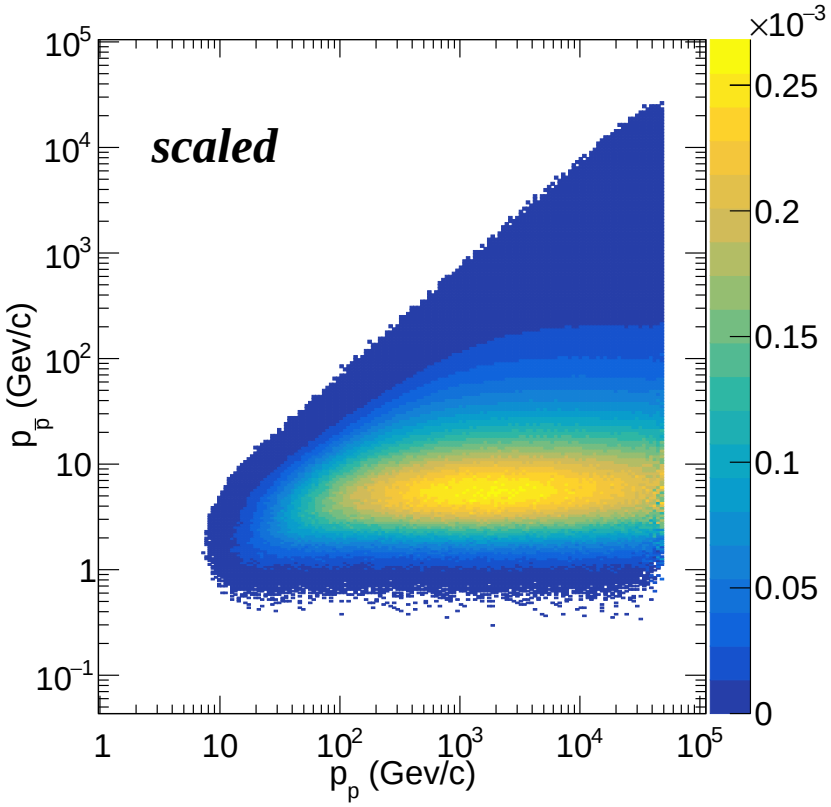

Figure 6.9 The antiproton invariant cross section $\frac{d\sigma}{dp}$ (barn c/GeV) calculated for the GALPROP momentum grid.

As shown before, the Winkler parametrization reproduces the collision energy dependence of the mutiplicities very well thus we scale the generator results for every collision energy, to agree with the values produced by Winkler parametrization. This means that in our GAL-

PROP simulations, the antiproton production cross sections are the same as in the Winkler parametrization, but the momentum distribution of the produced antiprotons is taken from the generator results. The resulting cross sections from GiBUU event generator are shown in Figure 6.9. GiBUU is able to simulate only antiproton production at projectile proton momentum lower than 49952.6 GeV/c, thus in the Figure 6.9, we see a cut-off. We use this result in GALPROP as a look-up table for antiproton production in $p + p$ collisions in the interstellar medium.

Chapter 7

Antiproton Cosmic Ray Flux

In this chapter we show the antiproton fluxes resulting in GALPROP simulation using different invariant antiproton cross sections. We investigate the fraction of antiprotons in the total antiproton flux from different collision systems.

First of all, in section 5.4 we compared our proton flux to the experimental data and saw that at energies around $\sqrt{s} = 6$ GeV, we have a 10% difference. To investigate, how a change in the proton flux influences the antiproton flux, we decreased the proton flux by 10% in GALPROP. The resulting antiproton fluxes and their ratio can be seen in Figure 7.1a. For this test we use the Kachelriess cross sections. Decreasing the proton flux by 10%, decreases the antiproton flux by 10%.
Moreover, the GiBUU event generator can not simulate collisions at a proton momentum $p_p > 49952.6$ GeV/c. Since the GiBUU total antiproton cross sections are normalized to the Winkler parametrization, we use the Winkler parametrization to check how this influences the antiproton flux. In Figure 7.1b we see, that antiproton flux remains unchanged at kinetic energies lower than 100 GeV and then starts immediately decreasing.
GALPROP uses the Tan and Ng parametrization for $p + p$ collisions and scales the results according to the Simon et al. parametrization which are given in chapter 4. The scaling by SImon et al. includes multiple colliding systems simultaneously and thus there is no way to separate the $p + He$ or $He + He$ components from the rest of the colliding systems. In Figure 7.1c we show comparison for both Kachelriess and Tan and Ng parametrizations including all collision systems and only $p + p$ collisions. In the Tan and Ng parametrization, around 52-53 % of antiprotons are produced in $p + p$ collisions, while at high energies - 56%. We see a different behaviour in the Kachelriess parametrization, where at low energies around 54% of antiprotons come from $p + p$ collisions and at higher energies it decreases to 46%.
In Figure 7.1d we show a comparison of antiproton flux created in only $p + p$ collisions and antiproton flux produced in $p + p$, $p + He$, $He + p$ and $He + He$ (we call this proton and helium channels). The antiproton momentum dependence of the ratio is similar for the Kachelriess and Winkler parametrizations. In the case of the Winkler parametrization, at low energies around 59% of produced antiprotons in proton and helium channels comes from $p + p$ collisions. At higher energies this ratio decreases to around 48%. While in the Kachelriess parametrization ratio changes from 61% to 50% and then we see instant drop of antiprotons.

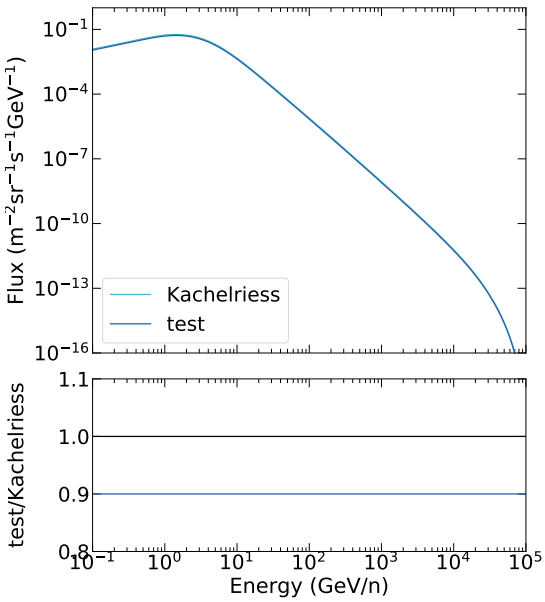

(a) test - 10% antiprotons used.

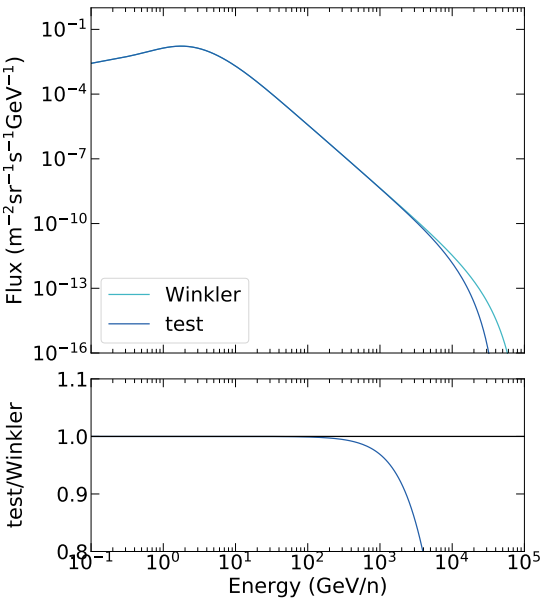

(b) test - only $p_p < 49952.6$ protons are used.

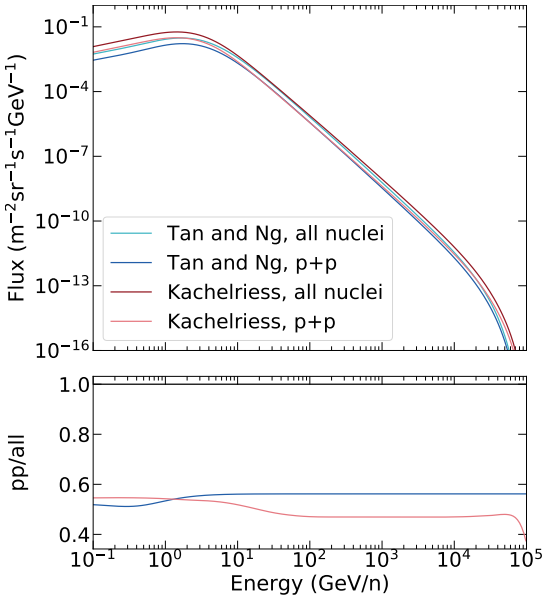

(c) Antiprotons from only $p+p$ collisions compared to all nuclei collisions.

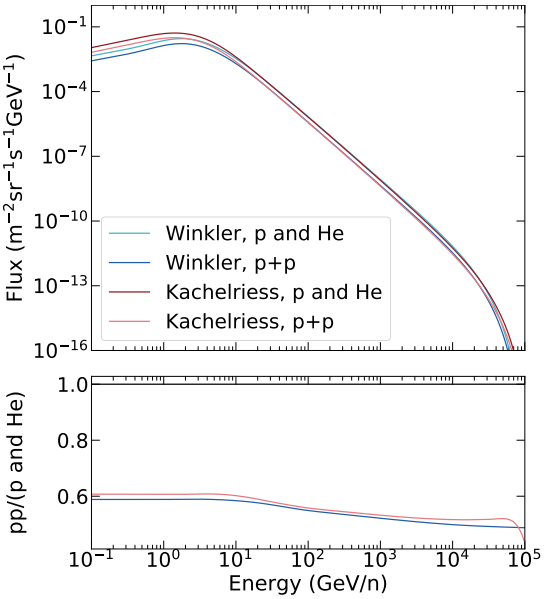

(d) Antiprotons from only $p+p$ collisions compared to antiprotons from proton and helium channels.

Figure 7.1 Comparison of antiproton fluxes. The standard parameters, as described in GALPROP section, are used.

As in the Winkler parametrization we include only the proton and helium channels, we need an estimate of how many antiprotons are produced from collision of heavier nuclei than helium. We get an estimate for this from the Kachelriess parametrization. The result is shown in Figure 7.2a. Proton and helium channels account for 85% to 90% of all produced antiprotons.
Finally, in Figure 7.2b we show a comparison of antiproton fluxes produced in the $p+p$ collisions using the Winkler parametrization and GiBUU event generator results. As mentioned

before, the total antiproton production cross section of GiBUU is scaled to Winkler. Thus the only difference between the parametrizations is the momentum distribution. Using the invariant differential cross sections obtained from the GiBUU event generator, more low energy antiprotons are produced than high energy antiprotons, compared to Winkler parametrization. In GiBUU case, antiprotons with energies higher than 18000 GeV are never produced. This might be a real effect, but it could be as well a problem of statistics during GiBUU run.

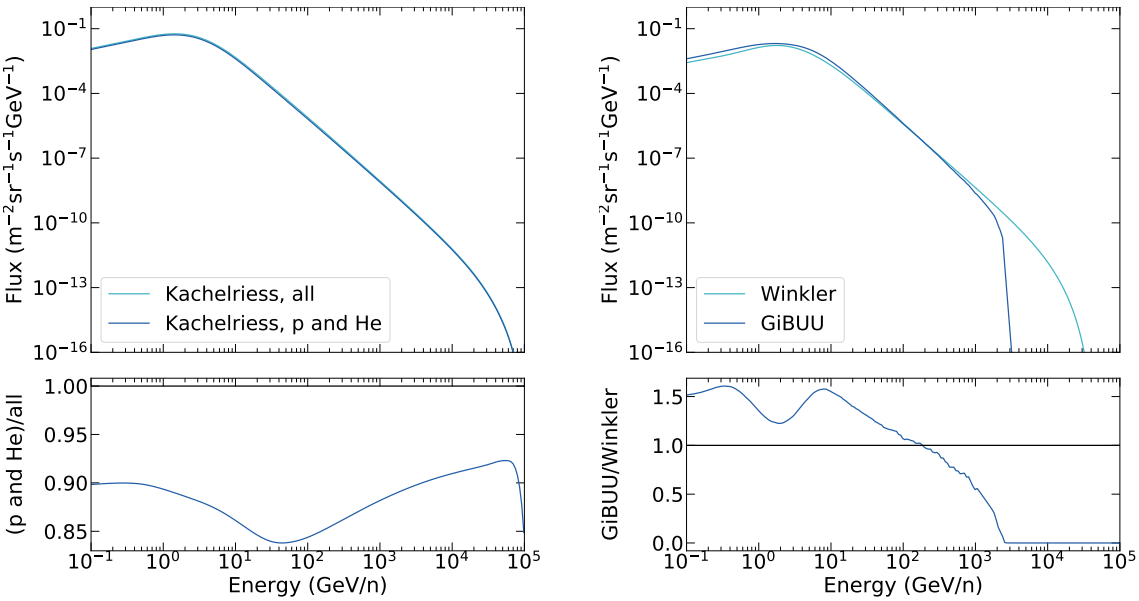

(a) Antiprotons from proton and helium channels compared to all nuclei channel.

(b) Antiproton flux calculated using Winkler and GiBUU inclusive cross sections.

Figure 7.2 Comparison of antiproton fluxes. The standard parameters, as described in GALPROP section, are used.

Finally we propagate the obtained local interstellar fluxes in the heliosphere using HelMod and compare the resulting top of the atmosphere fluxes to the AMS-02 data. We do this for separate antiproton production channels and show fluxes obtained using different invariant cross section parametrizations.

In Figure 7.3a, the antiproton top of the atmosphere fluxes simulated using the Kachelriess and Tan and Ng parametrizations are shown. In both cases, all available collision systems are included. As already mentioned before, the Kachelriess parametrization has $p+A$ and $He+A$ collisions implemented where A are nuclei up to iron. In case of Tan and Ng parametrization, for heavier nuclei GALPROP uses the scaling introduced in section 4.2.1. It includes all collision systems shown in Figure 4.1. The antiproton flux obtained using the Kachelriess parametrization agrees with the data well at high energies but overestimates the flux at low energies. This is not unexpected as the Kachelriess parametrization overestimates the prompt antiproton production at low collision energies compared to the particle collider data as well (shown in Figure 6.2). The antiproton top of the atmosphere flux obtained using the Tan and Ng parametrization fits the low energy data better but underestimates the antiproton flux at $E_{kin} > 2$ GeV.

In Figure 7.3b, we show a comparison of antiproton fluxes produced in $p+p$, $p+He$, $He+p$ and $He+He$ collisions.

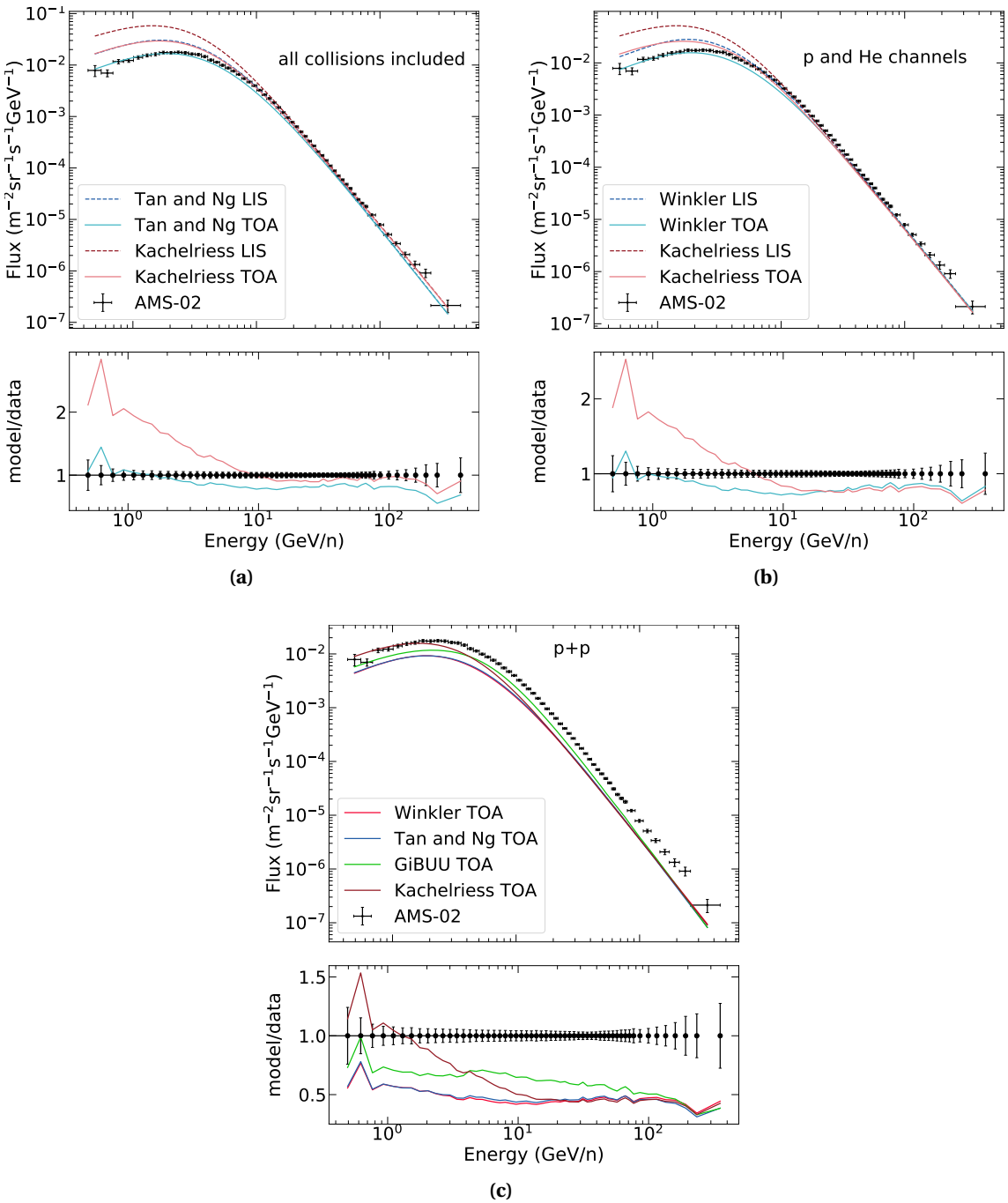

Figure 7.3 The top of the atmosphere flux (TOA) of antiprotons produced using different invariant cross section parametrizations. Each plot represents different antiproton production channels included. (a) all collision systems, available in both parametrizations, are included; (b) - only proton and helium channels: p+p, p+He, He+p and He+He; (c) - only p+p. The dashed lines show the local interstellar fluxes (LIS).

At $E_{kin} > 20$ GeV, the Kachelriess and Winkler parametrization give similar results. At lower energies, the Kachelriess parametrization is overestimating the antiproton production while the antiproton flux obtained using Winkler parametrization fits the AMS-02 data better. In Figure 7.3c, we show comparison of antiproton top of the atmosphere flux produced only in

$p+p$ collisions. The antiproton flux obtained using Winkler parametrization is very similar to the one obtained using Tan and Ng. In case of Kachelriess parametrization, we again see that at low energies it strongly overestimates the antiproton production. In case of the invariant antiproton cross sections obtained from GiBUU event generator, the resulting top of the atmosphere antiproton flux seems to be strongly overestimated at the full energy range of AMS-02 experiment.

Chapter 8

Conclusions and Outlook

We investigated multiple models for cosmic ray propagation. For the propagation in the galaxy, the GALPROP numerical code is used because it realistically describes the galaxy setup and the propagation in the interstellar medium. For solar modulation we investigated three models: the force field approximation, the SOLARPROP and the HelMod numerical codes. The force field approximation is independent of the particle charge and the solar magnetic field polarity thus it is unfit for antimatter studies. The SOLARPROP model has one free parameter which, once chosen, should be the same for all experiments as it is constant in time. We showed in our work, that this is not the case and thus SOLARPROP is unable to reproduce the solar modulation right. The HelMod model is in the best agreement with the data and it models the dependence on the particle charge and polarity in a correct way. The final simulated proton cosmic ray fluxes have a 10% disagreement compared to the data at proton energies around 6 GeV. We showed, that this disagreement comes from the local interstellar flux simulations. For the cosmic ray propagation in earth's environment, we chose to use the Planetocomics Monte Carlo simulation. It reproduces the effects of the geomagnetic field and the interactions in the atmosphere on the local interstellar flux well. The absolute values of the simulated cosmic ray flux are lower than experimentally measured, but it might be an effect of too strong solar modulation or wrong atmosphere modelling.
We studied different antiproton production parametrizations and the event generators. The Tan and Ng parametrization is completely wrong at high energies and does not fit low energy collider data as well. The Kachelriess parametrization agrees better with the high energy data but at low energies overestimates the antiproton production twice. The Winkler parametrization agrees with the experimental data well at all energies. Motivated by the future studies of antideuterons, we investigated several event generators: GiBUU, EPOS and PYTHIA and compared the obtained inclusive invariant antiproton cross sections to the NA49 data. The EPOS event generator reproduces the x_F and p_T distributions the best. GiBUU fails to reproduce the p_T dependence while PYTHIA fails to reproduce both the x_F and p_T dependence.
We investigated, how the choice of inclusive invariant antiproton cross section changes the final antiproton cosmic ray fluxes. For this we implemented a general solution in GALPROP which uses an inclusive invariant cross section look-up tables produced by event generators. We as well implemented the Winker parametrization in GALPROP. Only the Kachelriess and Tan and Ng parametrizations have all collision systems implemented. The Kachelriess parametrization fits the AMS-02 data well at high energies, but overestimates low energies. The Tan and Ng parametrization is in a better agreement with low energy data but predicts

lower than measured antiproton flux at low energies. We compared the antiproton fluxes produced in $p+p$, $p+He$, $He+p$ and $He+He$ collisions using the Winkler parametrization and the Kachelriess parametrization. At high energy the two parametrizations give similar results while at low energies Winkler is in a better agreement with the data. At last, we compare the antiproton production in $p+p$ collisions using all three parametrizations and GiBUU results. The antiproton flux produced using Winkler and Tan and Ng is very similar. The GiBUU invariant cross sections overestimate the antiproton production.

We showed the antiproton cosmic ray flux produced using the GiBUU results as a proof of principle of our invariant cross section implementation in GALPROP. But as we showed in the antiproton production investigation, the EPOS event generator reproduces the momentum distribution of the produced antiprotons much better. Thus the next step is the creation of EPOS invariant cross section table for GALPROP momentum grid. In the future studies the antiproton production in $p+He$ and $He+He$ collisions must be investigated in the event generators as well.

When the antiproton production is constrained, the next step is to use the event generators for antideuteron production using coalescence afterburner. The antideuteron creation in GALPROP can be simply implemented the same way as the antiproton creation. Then the produced antideuterons can be propagated using our constrained cosmic ray propagation chain to predict the cosmic ray fluxes.

Appendix A

Galprop: isotropic abundances

The isotropic abundances used in our GALPROP simulations.

```
iso_abundance_01_001 = 0.876e+06     H
iso_abundance_01_002 = 34.8          H
iso_abundance_02_003 = 9.033      He
iso_abundance_02_004 = 0.772e+05     He
iso_abundance_03_006 = 6.36e-06     Li
iso_abundance_03_007 = 5.19e-04     Li
iso_abundance_04_007 = 0            Be
iso_abundance_04_009 = 2.65e-05     Be
iso_abundance_04_010 = 5.30e-06     Be
iso_abundance_05_010 = 1.80e-04     B
iso_abundance_05_011 = 7.42e-04     B
iso_abundance_06_012 = 2808         C
iso_abundance_06_013 = 5.268e-07     C
iso_abundance_07_014 = 190           N
iso_abundance_07_015 = 5.961e-05     N
iso_abundance_08_016 = 3570          O
iso_abundance_08_017 = 6.713e-07     O
iso_abundance_08_018 = 1.286          O
iso_abundance_09_019 = 2.664e-08     F
iso_abundance_10_020 = 312.5     Ne
iso_abundance_10_021 = 0.003556     Ne
iso_abundance_10_022 = 100.1     Ne
iso_abundance_11_023 = 22.84     Na
iso_abundance_12_024 = 658.1     Mg
iso_abundance_12_025 = 82.5     Mg
iso_abundance_12_026 = 104.7     Mg
iso_abundance_13_027 = 76.42     Al
iso_abundance_14_028 = 725.7     Si
iso_abundance_14_029 = 35.02     Si
iso_abundance_14_030 = 24.68     Si
iso_abundance_15_031 = 4.242     P
```

```
iso_abundance_16_032 = 89.12      S
iso_abundance_16_033 = 0.3056      S
iso_abundance_16_034 = 3.417      S
iso_abundance_16_036 = 0.0004281      S
iso_abundance_17_035 = 0.7044      Cl
iso_abundance_17_037 = 0.001167      Cl
iso_abundance_18_036 = 9.829      Ar
iso_abundance_18_038 = 0.6357      Ar
iso_abundance_18_040 = 0.001744      Ar
iso_abundance_19_039 = 1.389      K
iso_abundance_19_040 = 3.022      K
iso_abundance_19_041 = 0.0003339      K
iso_abundance_20_040 = 51.13      Ca
iso_abundance_20_041 = 1.974      Ca
iso_abundance_20_042 = 1.134e-06      Ca
iso_abundance_20_043 = 2.117e-06      Ca
iso_abundance_20_044 = 9.928e-05      Ca
iso_abundance_20_048 = 0.1099      Ca
iso_abundance_21_045 = 1.635      Sc
iso_abundance_22_046 = 5.558      Ti
iso_abundance_22_047 = 8.947e-06      Ti
iso_abundance_22_048 = 6.05e-07      Ti
iso_abundance_22_049 = 5.854e-09      Ti
iso_abundance_22_050 = 6.083e-07      Ti
iso_abundance_23_050 = 1.818e-05      V
iso_abundance_23_051 = 5.987e-09      V
iso_abundance_24_050 = 2.873      Cr
iso_abundance_24_051 = 0      Cr
iso_abundance_24_052 = 8.065      Cr
iso_abundance_24_053 = 0.003014      Cr
iso_abundance_24_054 = 0.4173      Cr
iso_abundance_25_053 = 6.499      Mn
iso_abundance_25_055 = 1.273      Mn
iso_abundance_26_054 = 49.08      Fe
iso_abundance_26_055 = 0      Fe
iso_abundance_26_056 = 697.7      Fe
iso_abundance_26_057 = 21.67      Fe
iso_abundance_26_058 = 3.335      Fe
iso_abundance_27_059 = 2.214      Co
iso_abundance_28_058 = 28.88      Ni
iso_abundance_28_059 = 0      Ni
iso_abundance_28_060 = 11.9      Ni
iso_abundance_28_061 = 0.5992      Ni
iso_abundance_28_062 = 1.426      Ni
iso_abundance_28_064 = 0.3039      Ni
```

Bibliography

[1] F. Zwicky, "Die Rotverschiebung von extragalaktischen Nebeln," *Helv. Phys. Acta*, vol. 6, pp. 110–127, 1933. [Gen. Rel. Grav.41,207(2009)]. *cited in 1 (p. 1), 2.1 (p. 4)*

[2] D. Clowe, M. Bradač, A. H. Gonzalez, M. Markevitch, S. W. Randall, C. Jones, and D. Zaritsky, "A direct empirical proof of the existence of dark matter," *The Astrophysical Journal*, vol. 648, pp. L109–L113, aug 2006. *cited in 1 (p. 1), 2.1.2 (p. 5)*

[3] F. Mayet, A. Green, J. Battat, J. Billard, N. Bozorgnia, *et al.*, "A review of the discovery reach of directional dark matter detection," *Physics Reports*, vol. 627, pp. 1 – 49, 2016. A review of the discovery reach of directional Dark Matter detection. *cited in 1 (p. 1)*

[4] M. CIRELLI, "Indirect searches for dark matter," *Pramana*, vol. 79, pp. 1021–1043, Nov 2012. *cited in 1 (p. 1)*

[5] M. Felcini, "Searches for Dark Matter Particles at the LHC," in *53rd Rencontres de Moriond on Cosmology La Thuile, Italy, March 17-24, 2018*, 2018. *cited in 1 (p. 1)*

[6] V. Hess *Physikalische Zeitschrschift*, vol. 13, p. 1084, 1912. *cited in 1 (p. 2)*

[7] C. D. Anderson, "The apparent existence of easily deflectable positives," *Science*, vol. 76, no. 1967, pp. 238–239, 1932. *cited in 1 (p. 2)*

[8] M. Ackermann, M. Ajello, A. Allafort, L. Baldini, J. Ballet, *et al.*, "Detection of the characteristic pion-decay signature in supernova remnants," *Science*, vol. 339, no. 6121, pp. 807–811, 2013. *cited in 1 (p. 2)*

[9] V. C. Rubin, W. K. Ford, Jr., and N. Thonnard, "Rotational properties of 21 SC galaxies with a large range of luminosities and radii, from NGC 4605 /R = 4kpc/ to UGC 2885 /R = 122 kpc/," *ApJ*, vol. 238, pp. 471–487, June 1980. *cited in 2.1 (p. 4), 2.1.1 (p. 4), 2.1 (p. 5)*

[10] H. W. Babcock, "The rotation of the Andromeda Nebula," *Lick Observatory Bulletin*, vol. 19, pp. 41–51, 1939. *cited in 2.1.1 (p. 4)*

[11] J. H. Oort, "Some Problems Concerning the Structure and Dynamics of the Galactic System and the Elliptical Nebulae NGC 3115 and 4494.," *ApJ*, vol. 91, p. 273, Apr. 1940. *cited in 2.1.1 (p. 4)*

[12] M. S. Roberts, "A High-Resolution 21-CM Hydrogen-Line Survey of the Andromeda Nebula," *ApJ*, vol. 144, p. 639, may 1966. *cited in 2.1.1 (p. 4)*

[13] N. Aghanim *et al.*, "Planck 2018 results. VI. Cosmological parameters," 2018. *cited in 2.1.3 (p. 6)*

[14] M. Tanabashi, K. Hagiwara, K. Hikasa, K. Nakamura, Y. Sumino, *et al.*, "Review of particle physics," *Phys. Rev. D*, vol. 98, p. 030001, Aug 2018. *cited in 2.2 (p. 6)*

[15] G. Bertone, D. Hooper, and J. Silk, "Particle dark matter: evidence, candidates and constraints," *Physics Reports*, vol. 405, no. 5, pp. 279 – 390, 2005. *cited in 2.2 (p. 6)*

[16] A. Boyarsky, A. Neronov, O. Ruchayskiy, and M. Shaposhnikov, "Constraints on sterile neutrinos as dark matter candidates from the diffuse X-ray background," *Monthly Notices of the Royal Astronomical Society*, vol. 370, pp. 213–218, 07 2006. *cited in 2.2 (p. 6)*

[17] K. C. Y. Ng, B. M. Roach, K. Perez, J. F. Beacom, S. Horiuchi, *et al.*, "New constraints on sterile neutrino dark matter from nustar m31 observations," *Phys. Rev. D*, vol. 99, p. 083005, Apr 2019. *cited in 2.2 (p. 6)*

[18] E. Aprile, F. Agostini, M. Alfonsi, K. Arisaka, F. Arneodo, *et al.*, "First axion results from the xenon100 experiment," *Phys. Rev. D*, vol. 90, p. 062009, Sep 2014. *cited in 2.2 (p. 6)*

[19] K. Ehret, M. Frede, S. Ghazaryan, M. Hildebrandt, E.-A. Knabbe, *et al.*, "New alps results on hidden-sector lightweights," *Physics Letters B*, vol. 689, no. 4, pp. 149 – 155, 2010. *cited in 2.2 (p. 6)*

[20] S. J. Asztalos *et al.*, "The axion dark-matter eXperiment: Results and plans," in *Proceedings, 7th Patras Workshop on Axions, WIMPs and WISPs (AXION-WIMP 2011): Mykonos, Greece, June 27-July 1, 2011*, pp. 47–50, 2011. *cited in 2.2 (p. 6)*

[21] J. Conrad and O. Reimer, "Indirect dark matter searches in gamma and cosmic rays," *Nature Physics*, vol. 13, pp. 224 EP –, Mar 2017. Review Article. *cited in 2.2 (p. 7)*

[22] G. Jungman, M. Kamionkowski, and K. Griest, "Supersymmetric dark matter," *Physics Reports*, vol. 267, no. 5, pp. 195 – 373, 1996. *cited in 2.2 (p. 7), 2.2.1 (p. 8), 2.4 (p. 8)*

[23] E. Morgante, *Aspects of WIMP Dark Matter searches at colliders and other probes*. PhD thesis, Geneva U., Dept. Theor. Phys., 2016-09-20. *cited in 2.2 (p. 7), 2.5 (p. 8)*

[24] S. Y. Hoh, J. R. Komaragiri, and W. A. T. Wan Abdullah, "Dark matter searches at the large hadron collider," *AIP Conference Proceedings*, vol. 1704, no. 1, p. 020005, 2016. *cited in 2.3 (p. 7)*

[25] P. von Doetinchem, T. Aramaki, S. Boggs, H. Fuke, C. Hailey, *et al.*, "GAPS - Dark matter search with low-energy cosmic-ray antideuterons and antiprotons," *PoS*, vol. ICRC2015, p. 1219, 2016. [34,1218(2015)]. *cited in 2.6 (p. 9)*

[26] T. Aramaki *et al.*, "Review of the theoretical and experimental status of dark matter identification with cosmic-ray antideuterons," *Phys. Rept.*, vol. 618, pp. 1–37, 2016. *cited in 2.7 (p. 10)*

[27] G. Giesen, M. Boudaud, Y. Génolini, V. Poulin, M. Cirelli, *et al.*, "AMS-02 antiprotons, at last! secondary astrophysical component and immediate implications for dark matter," *Journal of Cosmology and Astroparticle Physics*, vol. 2015, pp. 023–023, sep 2015. *cited in 2.8 (p. 10)*

[28] E. Fermi, "On the origin of the cosmic radiation," *Phys. Rev.*, vol. 75, pp. 1169–1174, Apr 1949. *cited in 3.1 (p. 11)*

[29] F. C. Jones and D. C. Ellison, "The plasma physics of shock acceleration," *Space Science Reviews*, vol. 58, pp. 259–346, Dec 1991. *cited in 3.1 (p. 11)*

[30] A. R. Bell, "The acceleration of cosmic rays in shock fronts – I," *Monthly Notices of the Royal Astronomical Society*, vol. 182, pp. 147–156, 02 1978. *cited in 3.1 (p. 11)*

[31] T. K. Gaisser, R. Engel, and E. Resconi, *Cosmic Rays and Particle Physics*. Cambridge University Press, 2 ed., 2016. *cited in 3.1.1 (p. 11), 3.1.2 (p. 13), 3.1.3 (p. 14), 3.2.1 (p. 15), 3.3.1 (p. 19)*

[32] T. P. A. Collaboration, "The cosmic ray energy spectrum measured using the pierre auger observatory," in *Proceedings of the 35th International Cosmic Ray Conference*, vol. ICRC2017, p. 486, Proceedings of Science, 2017. *cited in 3.3 (p. 14)*

[33] M. Aguilar *et al.*, "Precision measurement of the proton flux in primary cosmic rays from rigidity 1 gv to 1.8 tv with the alpha magnetic spectrometer on the international space station," *Physical Review Letters*, vol. 114, p. 171103, 2015. *cited in 3.3 (p. 14)*

[34] Y. S. Yoon *et al.*, "Proton and helium spectra from the cream-iii flight," *The Astrophysical Journal*, vol. 839, no. 1, p. 5, 2017. *cited in 3.3 (p. 14), 3.4.1 (p. 23)*

[35] S. Ter-Antonyan, "Sharp knee phenomenon of primary cosmic ray energy spectrum," *Physical Review*, vol. D89, no. 12, p. 123003, 2014. *cited in 3.3 (p. 14)*

[36] R. Alfaro *et al.*, "All-particle cosmic ray energy spectrum measured by the hawc experiment from 10 to 500 tev," *Physical Review*, vol. D96, no. 12, p. 122001, 2017. *cited in 3.3 (p. 14)*

[37] T. Abu-Zayyad *et al.*, "Measurement of the cosmic ray energy spectrum and composition from 10^{17} ev to $10^{18.3}$ ev using a hybrid fluorescence technique," *The Astrophysical Journal*, vol. 557, pp. 686–699, 2001. *cited in 3.3 (p. 14)*

[38] R. U. Abbasi *et al.*, "First observation of the greisen-zatsepin-kuzmin suppression," *Physical Review Letters*, vol. 100, p. 101101, 2008. *cited in 3.3 (p. 14)*

[39] M. G. Aartsen *et al.*, "Measurement of the cosmic ray energy spectrum with icetop-73," *Physical Review*, vol. D88, no. 4, p. 042004, 2013. *cited in 3.3 (p. 14)*

[40] T. Antoni, W. Apel, A. Badea, K. Bekk, A. Bercuci, *et al.*, "Kascade measurements of energy spectra for elemental groups of cosmic rays: Results and open problems," *Astroparticle Physics*, vol. 24, no. 1, pp. 1 – 25, 2005. *cited in 3.3 (p. 14)*

[41] W. Apel, J. Arteaga-Velázquez, K. Bekk, M. Bertaina, J. Blümer, *et al.*, "The spectrum of high-energy cosmic rays measured with kascade-grande," *Astroparticle Physics*, vol. 36, no. 1, pp. 183 – 194, 2012. *cited in 3.3 (p. 14)*

[42] M. Amenomori, X. J. Bi, D. Chen, S. W. Cui, Danzengluobu, *et al.*, "The all-particle spectrum of primary cosmic rays in the wide energy range from 1014to 1017ev observed with the tibet-III air-shower array," *The Astrophysical Journal*, vol. 678, pp. 1165–1179, may 2008. *cited in 3.3 (p. 14)*

[43] Z. M. Malkin, "Analysis of determinations of the distance between the sun and the galactic center," *Astronomy Reports*, vol. 57, pp. 128–133, Feb 2013. *cited in 3.2.1 (p. 15)*

[44] M. S. Longair, *High energy astrophysics.* Cambridge University Press, 2004. *cited in 3.2.2 (p. 15), 3.2.2 (p. 16), 3.2.2 (p. 17)*

[45] I. V. Moskalenko, A. W. Strong, J. F. Ormes, and M. S. Potgieter, "Secondary antiprotons and propagation of cosmic rays in the galaxy and heliosphere," *The Astrophysical Journal*, vol. 565, pp. 280–296, jan 2002. *cited in 3.5 (p. 16), 3.2.2 (p. 16), 5.1.1 (p. 36)*

[46] J. M. Dickey and F. J. Lockman, "H i in the galaxy," *Annual Review of Astronomy and Astrophysics*, vol. 28, no. 1, pp. 215–259, 1990. *cited in 3.2.2 (p. 16)*

[47] M. A. Gordon and W. B. Burton, "Carbon monoxide in the Galaxy. I - The radial distribution of CO, H2, and nucleons," *Astrophysical Journal*, vol. 208, pp. 346–353, Sept. 1976. *cited in 3.2.2 (p. 16)*

[48] P. Cox, E. Kruegel, and P. G. Mezger, "Principal heating sources of dust in the galactic disk," *Astronomy and Astrophysics*, vol. 155, pp. 380–396, Feb. 1986. *cited in 3.2.2 (p. 16)*

[49] E. Habart, M. Walmsley, L. Verstraete, S. Cazaux, R. Maiolino, *et al.*, "Molecular hydrogen," *Space Science Reviews*, vol. 119, pp. 71–91, Aug 2005. *cited in 3.2.2 (p. 17)*

[50] P. M. Solomon and J. W. Barrett, "The CO - H_2 Mass Conversion Factor," in *Dynamics of Galaxies and Their Molecular Cloud Distributions* (F. Combes and F. Casoli, eds.), vol. 146 of *IAU Symposium*, p. 235, Jan 1991. *cited in 3.2.2 (p. 17)*

[51] L. Bronfman, R. S. Cohen, H. Alvarez, J. May, and P. Thaddeus, "A CO survey of the southern Milky Way - The mean radial distribution of molecular clouds within the solar circle," *Astrophysical Journal*, vol. 324, pp. 248–266, Jan. 1988. *cited in 3.2.2 (p. 17)*

[52] J. M. Cordes, J. M. Weisberg, D. A. Frail, S. R. Spangler, and M. Ryan, "The galactic distribution of free electrons," *Nature*, vol. 354, no. 6349, pp. 121–124, 1991. *cited in 3.2.2 (p. 17)*

[53] K. Ferrière, "The origin of galactic magnetic fields and their impact on the interstellar medium," in *The Magnetized Plasma in Galaxy Evolution* (K. T. Chyzy, K. Otmianowska-Mazur, M. Soida, and R.-J. Dettmar, eds.), pp. 147–155, Jun 2005. *cited in 3.2.2 (p. 17)*

[54] A. Ruzmaikin, "Magnetic fields of galaxies," in *Interstellar Magnetic Fields* (R. Beck and R. Gräve, eds.), (Berlin, Heidelberg), pp. 16–22, Springer Berlin Heidelberg, 1987. *cited in 3.2.2 (p. 17)*

[55] J.-L. Han, "The Large - scale magnetic field structure of our galaxy: Efficiently deduced from pulsar rotation measures," in *Magnetized Interstellar Medium Conference Antalya, Turkey, September 8-12, 2003*, 2004. *cited in 3.2.2 (p. 17)*

[56] F. H. Shu, F. C. Adams, and S. Lizano, "Star formation in molecular clouds: Observation and theory," *Annual Review of Astronomy and Astrophysics*, vol. 25, no. 1, pp. 23–81, 1987. *cited in 3.2.3 (p. 17)*

[57] V. N. Gamezo, A. M. Khokhlov, E. S. Oran, A. Y. Chtchelkanova, and R. O. Rosenberg, "Thermonuclear supernovae: Simulations of the deflagration stage and their implications," *Science*, vol. 299, no. 5603, pp. 77–81, 2003. *cited in 3.2.3 (p. 18)*

[58] F. Hoyle and W. A. Fowler, "Nucleosynthesis in Supernovae.," *APJ*, vol. 132, p. 565, Nov 1960. *cited in 3.2.3 (p. 18)*

[59] G. L. Case and D. Bhattacharya, "A new Σ-D relation and its application to the galactic supernova remnant distribution," *The Astrophysical Journal*, vol. 504, pp. 761–772, sep 1998. *cited in 3.2.3 (p. 18)*

[60] A. W. Strong and J. R. Mattox, "Gradient model analysis of EGRET diffuse Galactic γ-ray emission.," *Astronomy and Astrophysics*, vol. 308, pp. L21–L24, Apr. 1996. *cited in 3.2.3 (p. 18)*

[61] A. W. Strong and I. V. Moskalenko, "Propagation of cosmic-ray nucleons in the galaxy," *The Astrophysical Journal*, vol. 509, pp. 212–228, dec 1998. *cited in 3.2.3 (p. 18), 3.2.3 (p. 18)*

[62] Yusifov, I. and Küçük, I., "Revisiting the radial distribution of pulsars in the galaxy," *A&A*, vol. 422, no. 2, pp. 545–553, 2004. *cited in 3.2.3 (p. 18)*

[63] R. Schlickeiser, *Cosmic ray astrophysics*. Springer, 2011. *cited in 3.3.1 (p. 19)*

[64] K. J. H. Phillips, *Guide to the sun*. Cambridge University Press, 1995. *cited in 3.3.2 (p. 20)*

[65] I. G. Usoskin, "A history of solar activity over millennia," *Living Reviews in Solar Physics*, vol. 14, p. 3, Mar 2017. *cited in 3.3.2 (p. 20), 5.2.4 (p. 40)*

[66] J. R. Jokipii and E. N. Parker, "on the Convection, Diffusion, and Adiabatic Deceleration of Cosmic Rays in the Solar Wind," *The Astrophysical Journal*, vol. 160, p. 735, May 1970. *cited in 3.3.2 (p. 20)*

[67] R. Kappl, "Solarprop: Charge-sign dependent solar modulation for everyone," *Computer Physics Communications*, vol. 207, pp. 386 – 399, 2016. *cited in 3.3.2 (p. 20), 5.2.3 (p. 40)*

[68] L. J. Gleeson and W. I. Axford, "Solar Modulation of Galactic Cosmic Rays," *The Astrophysical Journal*, vol. 154, p. 1011, Dec. 1968. *cited in 3.3.2 (p. 20)*

[69] R. Hide and P. Roberts, "The origin of the main geomagnetic field," *Physics and Chemistry of the Earth*, vol. 4, pp. 27 – 98, 1961. *cited in 3.3.3 (p. 21)*

[70] M. Aguilar, D. Aisa, B. Alpat, A. Alvino, G. Ambrosi, *et al.*, "Precision measurement of the proton flux in primary cosmic rays from rigidity 1 gv to 1.8 tv with the alpha magnetic spectrometer on the international space station," *Phys. Rev. Lett.*, vol. 114, p. 171103, Apr 2015. *cited in 3.4.2 (p. 23)*

[71] M. Aguilar, L. Ali Cavasonza, B. Alpat, G. Ambrosi, *et al.*, "Antiproton flux, antiproton-to-proton flux ratio, and properties of elementary particle fluxes in primary cosmic rays measured with the alpha magnetic spectrometer on the international space station," *Phys. Rev. Lett.*, vol. 117, p. 091103, Aug 2016. *cited in 3.4.2 (p. 23)*

[72] K. Abe, H. Fuke, S. Haino, T. Hams, M. Hasegawa, *et al.*, "MEASUREMENTS OF COSMIC-RAY PROTON AND HELIUM SPECTRA FROM THE BESS-POLAR LONG-DURATION BALLOON FLIGHTS OVER ANTARCTICA," *The Astrophysical Journal*, vol. 822, p. 65, may 2016. *cited in 3.4.2 (p. 24)*

[73] K. Abe, H. Fuke, S. Haino, T. Hams, A. Itazaki, *et al.*, "Measurement of the cosmic-ray low-energy antiproton spectrum with the first bess-polar antarctic flight," *Physics Letters B*, vol. 670, no. 2, pp. 103 – 108, 2008. *cited in 3.4.2 (p. 24)*

[74] K. Abe, H. Fuke, S. Haino, T. Hams, M. Hasegawa, *et al.*, "Measurement of the cosmic-ray antiproton spectrum at solar minimum with a long-duration balloon flight over antarctica," *Phys. Rev. Lett.*, vol. 108, p. 051102, Jan 2012. *cited in 3.4.2 (p. 24)*

[75] K. Abe, T. Sanuki, K. Anraku, Y. Asaoka, H. Fuke, *et al.*, "Measurements of proton, helium and muon spectra at small atmospheric depths with the bess spectrometer," *Physics Letters B*, vol. 564, no. 1, pp. 8 – 20, 2003. *cited in 3.4.3 (p. 24), 5.4 (p. 46), 5.4 (p. 47)*

[76] R. P. Feynman, "Very high-energy collisions of hadrons," *Phys. Rev. Lett.*, vol. 23, pp. 1415–1417, Dec 1969. *cited in 4 (p. 25)*

[77] R. Kappl and M. W. Winkler, "The cosmic ray antiproton background for AMS-02," *Journal of Cosmology and Astroparticle Physics*, vol. 2014, pp. 051–051, sep 2014. *cited in 4 (p. 26)*

[78] S. J. Brodsky and J. F. Gunion, "Hadronic fragmentation as a probe of the underlying dynamics of hadron collisions," *Phys. Rev. D*, vol. 17, pp. 848–857, Feb 1978. *cited in 4 (p. 26)*

[79] L. C. Tan and L. K. Ng, "Parametrisation of hadron inclusive cross sections in p-p collisions extended to very low energies," *Journal of Physics G: Nuclear Physics*, vol. 9, pp. 1289–1308, oct 1983. *cited in 4.1 (p. 27), 6.1 (p. 49)*

[80] R. Kappl and M. W. Winkler, "The Cosmic Ray Antiproton Background for AMS-02," *JCAP*, vol. 1409, p. 051, 2014. *cited in 4.1 (p. 27)*

[81] M. W. Winkler, "Cosmic Ray Antiprotons at High Energies," *JCAP*, vol. 1702, no. 02, p. 048, 2017. *cited in 4.1 (p. 27), 4.1.2 (p. 29), 4.1.2 (p. 29), 4.1.2 (p. 29), 4.2.2 (p. 32), 6.1 (p. 49), 6.1 (p. 50)*

[82] K. Guettler, B. Duff, M. Prentice, S. Sharrock, W. Gibson, *et al.*, "Inclusive production of low-momentum charged pions, kaons, and protons at $x = 0$ at the cern intersecting storage rings," *Nuclear Physics B*, vol. 116, no. 1, pp. 77 – 98, 1976. *cited in 4.1.1 (p. 27)*

[83] B. Baatar, G. Barr, J. Bartke, L. Betev, O. Chvala, *et al.*, "Inclusive production of protons, anti-protons, neutrons, deuterons and tritons in p+c collisions at 158 gev/c beam momentum," *The European Physical Journal C*, vol. 73, p. 2364, Apr 2013.
cited in 4.1.2 (p. 28), 4.2.2 (p. 32), 4.2.2 (p. 32), 4.2 (p. 33)

[84] M. Simon, A. Molnar, and S. Roesler, "A new calculation of the interstellar secondary cosmic-ray antiprotons," *The Astrophysical Journal*, vol. 499, pp. 250–257, may 1998.
cited in 4.2 (p. 30), 4.1 (p. 31), 4.2.1 (p. 31), 4.2.1 (p. 31)

[85] W. Menn, M. Hof, O. Reimer, M. Simon, L. M. Barbier, *et al.*, "Measurement of the Absolute Proton and Helium Flux at the Top of the Atmosphere using IMAX," in *APS Meeting Abstracts*, p. K10.11, May 1996. *cited in 4.2.1 (p. 30)*

[86] J. J. Engelmann, P. Ferrando, A. Soutoul, P. Goret, E. Juliusson, *et al.* *cited in 4.2.1 (p. 30)*

[87] G. Barr, O. Chvala, H. Fischer, M. Kreps, M. Makariev, *et al.*, "Charged pion production in p+c collisions at 158 gev/c beam momentum: Discussion," *The European Physical Journal C*, vol. 49, pp. 919–945, Mar 2007. *cited in 4.2.2 (p. 31)*

[88] R. Aaij, C. Abellán Beteta, B. Adeva, M. Adinolfi, *et al.*, "Measurement of antiproton production in p—He collisions at $\sqrt{s_{\mathrm{NN}}} = 110$ GeV," *Phys. Rev. Lett.*, vol. 121, p. 222001, Nov 2018. *cited in 4.2 (p. 33)*

[89] I. V. Moskalenko, A. W. Strong, J. F. Ormes, and M. S. Potgieter, "Secondary antiprotons and propagation of cosmic rays in the galaxy and heliosphere," *The Astrophysical Journal*, vol. 565, pp. 280–296, jan 2002. *cited in 5 (p. 35)*

[90] R. Kappl, "Solarprop: Charge-sign dependent solar modulation for everyone," *Computer Physics Communications*, vol. 207, pp. 386 – 399, 2016. *cited in 5 (p. 35)*

[91] M. Boschini, S. D. Torre, M. Gervasi, G. L. Vacca, and P. Rancoita, "The helmod model in the works for inner and outer heliosphere: From ams to voyager probes observations," *Advances in Space Research*, 2019. *cited in 5 (p. 35), 5.2.2 (p. 39), 5.2.2 (p. 40)*

[92] L. Desorgher, E. O. Flückiger, and M. Gurtner, "The PLANETOCOSMICS Geant4 application," in *36th COSPAR Scientific Assembly*, vol. 36 of *COSPAR Meeting*, 2006.
cited in 5 (p. 35)

[93] "Galprop," *https://galprop.stanford.edu/*. *cited in 5.1 (p. 35)*

[94] M. J. Boschini, S. D. Torre, M. Gervasi, D. Grandi, G. Jóhannesson, and j. . T. a. . L. others, title = Solution of Heliospheric Propagation: Unveiling the Local Interstellar Spectra of Cosmic-ray Species vol. 840, p. 115, may 2017. *cited in 5.1.1 (p. 35), 5.4 (p. 43)*

[95] I. V. Moskalenko, S. G. Mashnik, and A. W. Strong, "New calculation of radioactive secondaries in cosmic rays," in *27th International Cosmic Ray Conference (ICRC 2001) Hamburg, Germany, August 7-15, 2001*, p. 1836, 2001. [5,1836(2001)]. *cited in 5.1.1 (p. 36)*

[96] I. G. Usoskin, G. A. Bazilevskaya, and G. A. Kovaltsov, "Solar modulation parameter for cosmic rays since 1936 reconstructed from ground-based neutron monitors and ionization chambers," *Journal of Geophysical Research: Space Physics*, vol. 116, no. A2, 2011. *cited in 5.2.1 (p. 39), 5.2.3 (p. 40)*

[97] M. Boschini, S. D. Torre, M. Gervasi, G. L. Vacca, and P. Rancoita, "Propagation of cosmic rays in heliosphere: The helmod model," *Advances in Space Research*, vol. 62, no. 10, pp. 2859 – 2879, 2018. Origins of Cosmic Rays. *cited in 5.2.2 (p. 40)*

[98] R. Kappl, "Charge-sign dependent solar modulation for everyone," *Journal of Physics: Conference Series*, vol. 718, p. 052020, may 2016. *cited in 5.2.3 (p. 40)*

[99] J. T. Hoeksema, "The Large-Scale Structure of the Heliospheric Current Sheet During the ULYSSES Epoch," *Space Science Reviews*, vol. 72, pp. 137–148, Apr 1995. *cited in 5.2.3 (p. 40)*

[100] I. G. Usoskin, A. Gil, G. A. Kovaltsov, A. L. Mishev, and V. V. Mikhailov, "Heliospheric modulation of cosmic rays during the neutron monitor era: Calibration using pamela data for 2006–2010," *Journal of Geophysical Research: Space Physics*, vol. 122, no. 4, pp. 3875–3887, 2017. *cited in 5.2.3 (p. 40)*

[101] M. S. Potgieter, "Solar modulation of cosmic rays," *Living Reviews in Solar Physics*, vol. 10, p. 3, Jun 2013. *cited in 5.2.4 (p. 42)*

[102] V. D. Felice, R. Munini, E. E. Vos, and M. S. Potgieter, "NEW EVIDENCE FOR CHARGE-SIGN-DEPENDENT MODULATION DURING THE SOLAR MINIMUM OF 2006 TO 2009," *The Astrophysical Journal*, vol. 834, p. 89, jan 2017. *cited in 5.2.4 (p. 42)*

[103] S. Miyake, R. Kataoka, and T. Sato, "Cosmic ray modulation and radiation dose of aircrews during the solar cycle 24/25," *Space Weather*, vol. 15, no. 4, pp. 589–605, 2017. *cited in 5.2.4 (p. 42)*

[104] A. C. Cummings, E. C. Stone, B. C. Heikkila, N. Lal, W. R. Webber, *et al.*, "GALACTIC COSMIC RAYS IN THE LOCAL INTERSTELLAR MEDIUM:VOYAGER 1observations AND MODEL RESULTS," *The Astrophysical Journal*, vol. 831, p. 18, oct 2016. *cited in 5.4 (p. 43)*

[105] I. V. Moskalenko, S. Digel, and G. Jóhannesson, "GALPROP Code for Galactic Cosmic Ray Propagation and Associated Photon Emissions," in *Proceedings, 32nd International Cosmic Ray Conference (ICRC 2011): Beijing, China, August 11-18, 2011*, vol. 6, p. 279. *cited in 5.4 (p. 43)*

[106] M. Kachelriess, I. V. Moskalenko, and S. S. Ostapchenko, "NEW CALCULATION OF ANTIPROTON PRODUCTION BY COSMIC RAY PROTONS AND NUCLEI," *The Astrophysical Journal*, vol. 803, p. 54, apr 2015. *cited in 6.1 (p. 49)*

[107] M. Antinucci, A. Bertin, P. Capiluppi, M. D'Agostino-Bruno, A. M. Rossi, *et al.*, "Multiplicities of charged particles up to isr energies," *Lettere al Nuovo Cimento (1971-1985)*, vol. 6, pp. 121–128, Jan 1973. *cited in 6.1 (p. 49)*

[108] O. Buss, T. Gaitanos, K. Gallmeister, H. van Hees, M. Kaskulov, *et al.*, "Transport-theoretical description of nuclear reactions," *Physics Reports*, vol. 512, no. 1, pp. 1 – 124, 2012. Transport-theoretical Description of Nuclear Reactions. *cited in 6.2 (p. 53)*

[109] K. Werner, F.-M. Liu, and T. Pierog, "Parton ladder splitting and the rapidity dependence of transverse momentum spectra in deuteron-gold collisions at the bnl relativistic heavy ion collider," *Phys. Rev. C*, vol. 74, p. 044902, Oct 2006. *cited in 6.2 (p. 53)*

[110] T. Sjöstrand, S. Ask, J. R. Christiansen, R. Corke, N. Desai, *et al.*, "An introduction to pythia 8.2," *Computer Physics Communications*, vol. 191, pp. 159 – 177, 2015. *cited in 6.2 (p. 53)*

[111] H. Drescher, M. Hladik, S. Ostapchenko, T. Pierog, and K. Werner, "Parton-based gribov–regge theory," *Physics Reports*, vol. 350, no. 2, pp. 93 – 289, 2001. *cited in 6.2 (p. 53)*

[112] D. Sarkar, S. Das, and S. Chattopadhyay, "Investigating the particle production at intermediate pt using identified triggered correlation in pp collisions at s = 7 tev," *Nuclear Physics A*, vol. 989, pp. 13 – 20, 2019. *cited in 6.2 (p. 53)*

[113] The NA49 Collaboration, "Inclusive production of protons, anti-protons and neutrons in p+p collisions at 158 gev/c beam momentum," *The European Physical Journal C*, vol. 65, p. 9, Nov 2009. *cited in 6.2 (p. 54)*